

**COUPLED MODE THEORY
BASED
MODELING AND ANALYSIS
OF
CIRCULAR OPTICAL MICRORESONATORS**

Kirankumar Rajshekhar Hiremath

The research presented in this dissertation was carried out at the Applied Analysis and Mathematical Physics group, the faculty of Electrical Engineering, Mathematics and Computer Science, and MESA+ Research Institute, University of Twente, P. O. Box 217, 7500 AE, Enschede, The Netherlands.

This research was carried out as a part of the European Commission funded project “*Next generation Active Integrated optic Subsystems*” (project IST-2000-28018).

Front cover: Field examples for a 2-D microdisk resonator. The plots show absolute value $|E_y|$ of the principal component of the TE fields (top), and snapshots of the real physical electric field E_y (bottom). From left to right, the field plots illustrate microresonator in off-resonance state, in TE_1 resonance state, and in TE_0 resonance state. The color scale levels of the plots in each row are comparable. For further details refer to Section 4.4.2.

Using just four relevant basis modes (the fundamental mode of a straight waveguide, and the first three lower order modes of a bent waveguide), the simulations are done with the coupled mode theory based approach discussed in this thesis.

Back cover: Whispering gallery modes of a 2-D bent waveguide. The plots show absolute value $|E_y|$ of the principal component of the TE mode profile (top), and snapshots of the real physical electric field E_y (bottom). From left to right, it illustrates TE_0 , TE_1 , and TE_2 mode. For further details refer to Section 2.4.5.

The results are obtained with the analytic model of bent waveguides presented in Chapter 2. Having access to the analytic bent modes greatly facilitated an efficient implementation of the coupled mode theory based model of bent-straight waveguide couplers, which in turn led to various accomplishments of the present resonator model.

This thesis was typeset using $\text{\LaTeX} 2_\epsilon$ and the softwares Emacs, \AUCTEX , \RefTeX under SuSe Linux. Except the use of MATLAB for plotting, all other softwares used are public domain (and mostly open source) softwares viz. g++, f77, Xdvi, ghostview, gnuplot, Xfig, and gimp. The cover page was designed in Openoffice.

**COUPLED MODE THEORY BASED
MODELING AND ANALYSIS OF
CIRCULAR OPTICAL MICRORESONATORS**

DISSERTATION

to obtain
the doctor's degree at the University of Twente,
on the authority of the rector magnificus,
prof. dr. W. H. M. Zijm,
on account of the decision of the graduation committee,
to be publicly defended
on Friday 14 October 2005 at 16:45

by

Kirankumar Rajshekhar Hiremath
born on 21 August 1976
in Solapur, India

This dissertation is approved by

the promotor
prof. dr. E. van Groesen

the assistant promotor
dr. Manfred Hammer

If I have seen further it is because they taught me to stand.

This work is dedicated to my teachers.

Acknowledgement

On 30 March 2001, I got an email from Brenny van Groesen, in which he wrote “.....One type of spectacular new devices are microresonators, where constructive interference of light traveling in a circular disk, may lead to transfer of light from one waveguide to another. Mathematical challenge is to understand the qualitative behaviour (with new physical phenomena), and using numerical tools, approximate actual solutions. My specific question to you: are you interested to accept this offer and to come to UTwente.....?” What happened after that is in this thesis in your hands! Brenny, thank you very much for introducing me to fascinating vista of mathematical aspects of electromagnetics.

While Brenny gave me a canvas to paint my impressions, Manfred Hammer gave me brushes and colors. I explored the landscape under his supervision. At the start of Ph. D., Manfred explained me the project, and gave the relevant literature collection done by him. That helped me to orient myself quickly in the right direction. In middle of the course, he gave me his 2-D straight waveguides mode solver. On top of which, I developed 2-D bent waveguides mode solver, bent-straight waveguide couplers module, and resonators module.

I learned countless things from him. It took me quite some time to get embodied in his extremely organized and disciplined way of *modus operandi*. And now, it became a part of my *modus vivendi*! His style of comprehensive analysis of a topic, meticulous writing, spotless presentation, and single-minded hard working left the ever lasting impressions on me. During the formative phase of the Ph. D., his alacritous availability for discussions, his insistence on preciseness helped me a lot. In retrospect, working with Manfred was the venerable experience.

I also benefited by the experience and insight of Hugo Hoekstra, Remco Stoffer and Theo Valkering. The discussions with them during group meetings and review meetings helped me to develop an understanding of the present interdisciplinary work from the application point of view.

I will like to thank my colleagues from Applied Analysis and Mathematical Physics (AAMP) and Numerical Analysis and Computational Mechanics (NACM) groups. I have fond memories of my officemates Pearu Peterson (for enjoying all sorts of “strange” coffees), Fedderik van der Bos (*voor Nederlands praten en vertalen*), Arek Kuczaj (for software troubleshooting). It was a great fun to work with Linux enthusiastic guys like Vijaya Ambati (Plotting=Gnuplot), Christiaan Klaij (Viva Emacs!), Lars Pesch (The Jack of many GNU softwares), Joris van den Berg (Mr. Macintosh).....and of course Manfred (For C++ optimization ideas, Xfig).

Scientific discussions with Agus Suryanto, Ardhasena Sopaheluwakan, Jaqueline Nicolau, Henri Uranus, Didit Yudistira was very useful. I will like to thank Timco Visser, Hala Elrofai, Helena Margaretha, Hadi Susanto, Natanael Karjanto, Monica Polner, Janivita Sudirham, Mikhail Tchesnokov, and Davit Harutyunyan. Also thanks to Debby Lanser, Mike Botchev, Bernard Geurts, and Chris Stolk for sharing their valuable experiences with me.

I have the unique memories of two very special persons: Marielle Plekenpol and Diana Dalenoord. They act as binding forces, leaving no stone unturned (well.... that is a quite difficult task in The Netherlands!) to make all of us mingle, come together for informal gatherings like birthday celebrations, lunch-together, group outings. They have added many countries to my philatelic collection. I acknowledge Marielle’s support for the administrative and practical matters.

Interaction with Mart Diemeer, Douwe Geuzebroek, Ronald Dekker, and many other colleagues from Integrated Optical MicroSystems (IOMS) group and MESA+ Research Institute, and also with NAIS project partners, especially with Ladislav Prkna, was very fruitful.

I thank Enno Oosterhuis and Ewout Bakker from computer helpdesk for their support for computational infrastructure. With the advent of the computers and wide spread use of digital format, a need to visit library is becoming less and less. Nevertheless, there is a team of dedicated librarians working quietly in the background. I thank the library support team for their efficient content provision. Thanks to Michel ten Bulte for his efficient co-ordination during moving from TWRC to Informatica, and from Informatica to Ravelijn. After a day’s work, I used to leave my table in a bit of mess, but next day it used to be systematically cleaned and arranged. How can I forget those nameless, unknown hands? Very special thanks to them.

The presence of Indian friends at the University of Twente was very important for emotional composure; many thanks from heart to Makarand Pimplapure, Rahul Dahule, Salim Deshmukh, Sheela Sowariraj, Rajshekhar Kakumani, Ramkrishna

Pasumarthy, Vijaya Ambati, Manish Arora, Amol Thakre, Chandrashekhar Murade, and Rajeev Roy; also to affectionate families Madhavi and Ravi Tupe, Shashi and Satyendra Tomar, Vishakha and Pramod Agarwal, Deepa and Viswanath Talasila, Kavitha and Kiran Thumma. I am recalling so many other names..... I will always cherish memories of all these *gezellige* people!

For the last four years, while I was working like a bee in my bonnet, far far away there are a few people who always used to encourage me without expressing their griefs. They gave me wings and power to fly. They supported my ideas to explore a new sky. I am indebted to my parents for giving me a free hand, and supporting me at the crucial moments. Thanks to my siblings Hemakka, Ashakka and Amit for taking care of the family, and leaving me free of any worries. I specially remember passing away of my grandmother, who was my the first mathematics teacher. Without the support of my siblings in “those” difficult situations, I don’t know.....how I would have found my way. Thank you Netra for being with me, and synchronizing my heartbeats and brain-waves. Thanks to pals Balaji Kasal and Ganesh Bagler.

The experience of these four years will “guide” my journey ahead. *Van harte bedankt allemaal, en tot straks.*

K. R. (Kiran) Hiremath

October 2005, Enschede

Abstract

For the full utilization of large bandwidth and high speed features provided by optical fibers, currently concepts for integrated optical devices for wavelength division multiplexing/demultiplexing are vigorously investigated. Due to their superior selectivity, compactness, and possibility of dense integration, microresonators with circular ring or disk cavities are attractive add-drop filter elements for applications in photonic chips related to optical wavelength-division multiplexing. Modeling of these devices is the topic of the present work.

In this thesis, we restrict ourself to two dimensional settings. While for specific configurations one could regard the present two dimensional model as an approximate description of realistic devices in terms of effective indices, in other cases simulations in three spatial dimensions are certainly necessary, e.g. for vertically coupled resonators. Therefore our model is formulated such that an extension to three dimensions is straightforward. We treat the circular microcavities as traveling wave resonators in the framework of a pure frequency domain description.

The most common resonator model, discussed in Chapter 1, permits a basic understanding of the functioning of these devices. The resonators are functionally represented in terms of two bent-straight waveguide couplers with appropriate connections using bent and straight waveguides. The abstract scattering matrices of these couplers, and the propagation constants of the cavity bends allow to compute the spectral responses of the resonators. Generally, these quantities are treated as free parameters. One of the objectives of this work is to present a systematic approach to compute these free parameters for given resonator configurations. Another objective is to characterize the response of the resonators systematically for various geometrical parameters (e.g. the radius of the cavity, the widths of the waveguides, the separation distances) and material parameters (e.g. the refractive indices).

A rigorous classical analytic model of confined optical wave propagation along 2-D bent slab waveguides and curved dielectric interfaces is investigated in Chapter 2. This frequency domain model is based on ansatz of piecewise continuous

bend mode profiles in terms of Bessel and Hankel functions. This approach provides a clear picture of the behaviour of bend modes, concerning their decay for large radial arguments or effects of varying bend radius. For the numerical implementation of this model, fast and reliable routines are required to evaluate Bessel functions with large complex orders and large arguments. Using the “uniform asymptotic expansions” of Bessel/Hankel functions, we found that with present standard computers it is not a problem to carry out the rigorous analytic evaluation of the problem. Our implementation enabled detailed studies of bent waveguide properties, including higher order bend modes and whispering gallery modes, their interference patterns, and issues related to bend mode normalization and orthogonality properties. Also a perturbational expression is derived for the shift in the propagation constant due to changes in the core refractive index.

Capitalizing on the availability of rigorous analytical modal solutions for 2-D bent waveguides, Chapter 3 presents a model of bent-straight waveguide couplers using a frequency domain spatial coupled mode formalism, derived by means of a variational principle. The formulation is consistent with standard physical notions; it takes into account that multiple modes in each of the cores may turn out to be relevant for the functioning of the resonators supplemented with such couplers. Simulation results for the response of 2-D couplers for monomode and multimode settings for varying separation distances, radii, and different wavelengths are discussed. The resulting scattering matrices show reciprocity as expected according to the symmetry of the coupler structures, which also provides a useful means of assessing the reliability of the simulations.

Having explained how to compute the required cavity mode propagation constants and the scattering matrices, Chapter 4 presents simulation results for the entire resonator devices. We also discuss a few procedures for the faster calculation of the spectral response. The examples cover the spectral response and field for microresonators with mono- and multi-modal cavities for TE and TM polarizations. Comparisons with finite difference time domain simulations show very good overall agreement. A detailed analysis of effect of the separation distances on the resonator spectral response is carried out, which leads to a useful criterion that should be satisfied by the numerical simulations. Also, a perturbational approach for the evaluation of tuning of resonators by slight changes of the cavity core refractive index is presented.

The present work about coupled mode theory based modeling and analysis of 2-D circular integrated optical microresonators paved the way for analogous simulations of realistic microresonators in three spatial dimensions.

Contents

1	Introduction	1
1.1	Rise of optical technology	2
1.2	Next generation Active Integrated optic Subsystems	4
1.3	Circular optical microresonators	5
1.4	Ring-resonator theory	8
1.4.1	“Standard model” for resonators: Monomode setting	9
1.4.2	Power transfer	10
1.4.3	Resonances	11
1.4.4	Resonance characteristics	12
1.4.5	Tuning	14
1.5	Existing approaches for modeling of circular microresonators	16
1.6	Scope of the thesis	17
1.7	Outline of the thesis	19
1.8	Publications	20
2	Analytic approach to dielectric optical bent slab waveguides	21
2.1	Existing approaches for modeling of bent waveguides	23
2.2	Bent waveguide model	24
2.2.1	Bend mode normalization	27
2.2.2	Orthogonality of bend modes	29

2.3	Remarks on the numerical implementation	32
2.4	Simulation results	33
2.4.1	Propagation constants	34
2.4.2	Mode profiles	36
2.4.3	Comparison with FDTD results	38
2.4.4	Higher order bend modes	39
2.4.5	Whispering gallery modes	42
2.5	Effect of core refractive index perturbation	44
2.6	Concluding remarks	47
3	Bent-Straight waveguide couplers	49
3.1	Coupled mode theory	50
3.2	Bent-straight waveguide couplers	51
3.2.1	Coupled mode equations	53
3.2.2	Transfer matrix and scattering matrix	55
3.2.3	Remarks on the projection operation	57
3.3	Reciprocity of scattering matrix	58
3.4	Simulation results	59
3.4.1	Coupler with monomodal bent waveguide	60
3.4.2	Coupler with multimodal bent waveguide	66
3.5	Concluding remarks	70
4	Microresonators	73
4.1	Abstract microresonator model	74
4.2	Scattering matrix analysis of the full resonator	77
4.3	Spectrum evaluation	79
4.4	Simulation results	80
4.4.1	Microring resonator	80
4.4.2	Microdisk resonator	84

4.4.3	Compact high contrast cavities	89
4.5	Influence of separation distance on the spectral response	93
4.5.1	Changing both separation distances identically	93
4.5.2	Changing only one of the separation distances	95
4.5.3	Shifting the cavity between fixed bus waveguides	98
4.6	Tuning	103
4.7	Concluding remarks	106
5	Conclusions and outlook	109

Chapter 1

Introduction

Communication networks are part and parcel of today's knowledge based society. Optical fibers are extensively used in state-of-the-art communication networks. But the use of electronic devices in heterogeneous electronic-optical networks represents a major bottleneck for the full utilization of large bandwidth and high speed features provided by the optical fibers. To circumvent such network traffic congestion, optics based technologies for wavelength division multiplexing/demultiplexing are vigorously investigated. Microcavity based resonators are one of the promising concepts for such applications. Modeling of these devices is the topic of the present work. This introductory chapter presents the general theory of circular microresonators as wavelength filters. It also outlines the organization of the present thesis.

Parts of this chapter are adapted from:

M. Hammer, K. R. Hiremath, and R. Stoffer. *Analytical approaches to the description of optical microresonator devices.*, In M. Bertolotti, A. Driessen, and F. Michelotti, editors, *Microresonators as building blocks for VLSI photonics*, volume 709 of AIP conference proceedings, pages 48–71. American Institute of Physics, Melville, New York, 2004.

The information and communication technology revolution transformed the world in a true sense into a global village. It changed the style of communication, transactions, and entertainment. E-mail communication became a standard practice. Internet enabled banking, 24/7 open automatic teller machines, e-commerce changed the way we used to deal with money. Computer aided design and manufacturing cut down the production cost of consumer products, and also increased their reliability. Voice-over-Internet is about to start a new era of low cost long distance telephony, and Video-on-Demand is lurking on the horizon. The genesis of this digital life style can be traced back into 1970s.

In 1970s, mass production by integration of electronic components helped to reduce the prices of electronic devices dramatically, and acted as a catalyst for the information technology revolution in 1990s. Soon computers became ubiquitous. The utility of computers increased significantly, when they were connected to each other. At present, the world wide web of computers (aka the Internet) is the most happening place in the world. As more and more day-to-day activities were getting information technology enabled, the demand for fast computers and high speed communication networks was also increasing. Traditionally, microelectronics was used for the manufacturing of data/signal processing devices, and copper cables were used as the carrier media for data transfer. But as the demand for high speed and large capacity data transfer was grown, the copper cable based communication networks were not able to handle it efficiently. At that time, optical fibers made their appearance [1], ushering a dawn of new technology.

1.1 Rise of optical technology

In modern-day communication systems, electromagnetic waves play a very important role. Communication with microwaves, radio waves are well known examples [2]. Optical fibers carry electromagnetic signals in the form of light waves. The wavelengths of these light waves ranges generally from $0.4 \mu\text{m}$ to $1.6 \mu\text{m}$. Unlike in the conventional copper wires, where electromagnetic signals are carried by electrons, in the optical fibers the signals are carried by photons.

This fundamental difference offers several advantages for the use of optical fibers in place of copper cables [3]. Compared to copper cables, optical fibers have much lower line loss and smaller dispersion per unit length. Moreover, optical fibers support a broad bandwidth permitting multiplexing to further increase the transmission capacity. Copper cables are prone to electromagnetic interference causing high error rates, and also they are sensitive to eavesdropping, whereas optical fibers

are immune to these problems. As a result, optical fibers soon became one of the essential components of communication networks.

As most processing/transmission devices (e.g. computers, routers, amplifiers, etc.) are at present based on electronics, data to be processed or transmitted is typically available in the form of electrical signals. To send these signals over optical fiber networks, these signals first have to be converted from the electrical domain to the optical domain. At amplifier/receiver units, the data have to be converted back to electrical signals. This signal conversion from the electrical domain to the optical domain, and vice versa, involves losses. And also the realization introduces additional costs [4].

With the use of optical fibers, even though the signal transmission is improved significantly, the ultimate performance of combined electronic-optical transmission systems is determined by the processing speed of the electronic devices. Micro-electronic devices are also getting faster, but their switching speed is not at par with the transmission capacity of optical networks [5, 6]. This is inevitable, because the underlying physical mechanisms for the transfer of electrons and photons are quite different. Also there are technological limitations for the extreme miniaturization of the electronic circuits [7]. To accommodate the increasing demand of faster information processing, there is a need to develop a new technology. The potential shown by the optical fibers drew attention to optics.

The field of optics has made huge progress from the time of seminal work of Huygens (1629-1695), Newton (1643-1727) and Maxwell (1831-1879). The invention of lasers in 1958 rejuvenated the interest in optics. The next stepping stone for optics was the use of optical fibers in telecommunication networks. This growing interest in optics led to the establishment of new fields like “optronics”, “photonics”¹.

A main concern of the field of modern optics is the *generation, manipulation, guidance, and detection* of light for communication and information processing applications. Thus the communication networks are evolving from mere cost effective optical signal transport in networks based on electronic devices to full-fledged optical networks. In an advanced stage, such optical networks will as far as possible avoid the expensive conversion of electrical signals into optical signals, and vice versa. Apart from optics based light sources, detectors, and signal carriers (i.e.

¹Optronics — opto-electronics — is about using modern optical technology along with conventional microelectronics technology. Many times, the terms “optics” and “photonics” are used interchangeably, and the distinction between them is rather vague. Optics is a quite wide field dealing with light in different contexts, spanning from geometrical optics (dealing with lenses, prisms, free space transmission, etc.) to quantum optics (dealing with light-matter interaction).

waveguides), essential building blocks of such networks are optics based amplifiers, modulators, switches, and filters [8]. Successful demonstration and realization of these functional components will lead to “all-optical-processing” systems.

1.2 Next generation Active Integrated optic Subsystems

Innovations in the areas of material sciences and lithography, coupled with the availability of powerful microscopy tools initiated intensified efforts towards “all-optical-processing” systems. As one of the outcomes of these current developments, it is now possible to realize compact and high finesse dielectric microcavities. These optical microcavities have shown a great potential for many applications [9]. For quite some time, microcavity resonators are discussed as promising building blocks for passive and active components for integrated optical devices [10]. Recent advances opened a range of possibilities of using micro-ring/disk resonators (a “cavity” coupled to single/dual waveguides) as lasers [11, 12, 13], logic gates [14, 15], optical switches [16, 17, 18], sensors [19, 20, 21], and add/drop (multiplexing/demultiplexing) wavelength filters [22, 23].

The performance of wavelength division multiplexing/demultiplexing filters plays a crucial role for the full utilization of the high bandwidth potential of optical fibers. At present, arrayed waveguide gratings (AWGs) are used for this purpose [24, 25]. But due to their comparably large sizes, AWGs are not suitable for the use in densely integrated photonic circuits [26, 27]. Alternatively, wavelength division filters based on photonic crystals are quite promising [28, 29, 30], but the corresponding technological issues are still challenging. On this background, due to their versatility, compactness and possibility of dense integration, resonators based on conventional microcavities became attractive candidates for add/drop wavelength filters. A recent overview of this field can be found in Ref. [31].

Microcavity based resonator filters can be configured in various ways [22]. In this work we are interested in resonators, in the form of dual waveguide coupled circular microcavities, as tunable add/drop wavelength filters. A wavelength filter is a device which, given several input signals of different wavelengths, selects one of these as the output wavelength. By an add/drop filter one means that not only one of the inputs can be dropped (i.e. extracted/demultiplexed), but also a new input can be added (i.e. inserted/multiplexed) to the outgoing signal. Tunability of a filter implies that one can tune (i.e. change) the output response of the filter to one of the desired input wavelengths.

The co-ordinated efforts to demonstrate the feasibility of microresonator based

compact integrated optical subsystems resulted in the project “*Next generation Active Integrated optic Subsystems*” (NAIS), funded by the European Commission within the framework of the Information Society Technologies programme [32]. This project was centered around the realization of microresonator based tunable add/drop wavelength filters. The work presented in this thesis has been part of that project.

The project NAIS has covered several aspects like material research, design tools and techniques, technology/fabrication, testing and packaging, and system requirements. Naturally, there were lots of interdependencies among these different research topics. The project involved several disciplines like physics, mathematics, electrical engineering, material science, etc. The progress of such a time-bound multidisciplinary engineering project is advanced by a sound understanding of the dependence of the performance of the devices on material and design aspects. In this regard, a realistic model of the device and a reliable simulation tool based on such a model is essential. This is where the present work, as part of the design workpackage, contributed to the project NAIS.

1.3 Circular optical microresonators

Two typical settings of microresonators are shown in Fig. 1.1. A ring or a disk shaped dielectric cavity is placed between two parallel dielectric straight waveguides. In real life (3-D) devices, the straight waveguides can be positioned either in the same plane (Fig. 1.1(a): horizontal coupling scheme) or below (Fig. 1.1(b): vertical coupling scheme) the cavity plane. These two straight waveguides form four ports for the external connections, the two input ports named “In-port” and “Add-port”, and the two output ports named “Through-port” and “Drop-port”. To understand the functioning of the microresonators, for the sake of simplicity, let’s consider only unidirectional fields (clockwise propagating), where only the In-port is illuminated, while there is no incoming signal at the Add-port.

Conventionally, the functioning of microresonators is described by the interaction of harmonic optical waves propagating along the straight waveguide and the cavity, and the interferometric resonances of the waves inside the cavity [33]. A single frequency optical wave is launched at the In-port of the resonator. As this signal propagates along the upper straight waveguide, that connects the In-port and Through-port, part of it is evanescently coupled to the cavity. While propagating along the cavity, part of this signal is coupled to the lower straight waveguide and appears at the Drop-port. The remaining part of the signal propagates along the cavity, and interferes with the newly in-coupled signal in the upper interac-

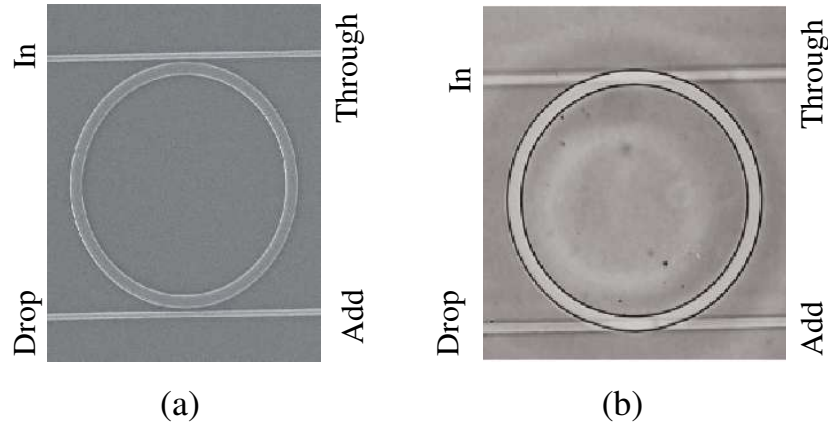


Figure 1.1: Scanning electron microscope pictures of horizontally coupled (a) and vertically coupled (b) real life microresonators. Courtesy: Integrated Optical Microsystems group, Department of Electrical Engineering, University of Twente.

tion region. Depending upon the specific configuration, these two fields undergo constructive or destructive interference.

If the cavity field is out of phase with the newly entering field, then destructive interference takes place inside the cavity and as a result, there is only a small amount of power inside the cavity. Under so-called off resonance conditions, as shown in Fig. 1.2(a), most of the input power is directly transmitted to the Through-port, and there is comparably low power at the Drop-port.

On the other hand, if the field inside the cavity is in phase with the newly in-coupled signal, then due to constructive interference, energy builds up inside the cavity. This field gets coupled to the Drop-port waveguide. Under so-called resonance conditions, there is a significant power observed at the Drop-port, while less power appears at the Through-port. This situation is shown in Fig. 1.2(b).

A typical spectral response of a microresonator device is shown in Fig. 1.3. Resonances appear as dips in the Through-port power curve and peaks in the Drop-port power curve. In other words, the wavelengths for which a microresonator is on resonance, will be “dropped” at the Drop-port. Also, for a symmetrical device, if a new signal that corresponds to a resonance wavelength is launched at the Add-port, it will get “added” to the off resonance signal launched at the In-port, and appears at the Through-port. Therefore the arrangement shown in Fig. 1.1 can be used as an add/drop filter.

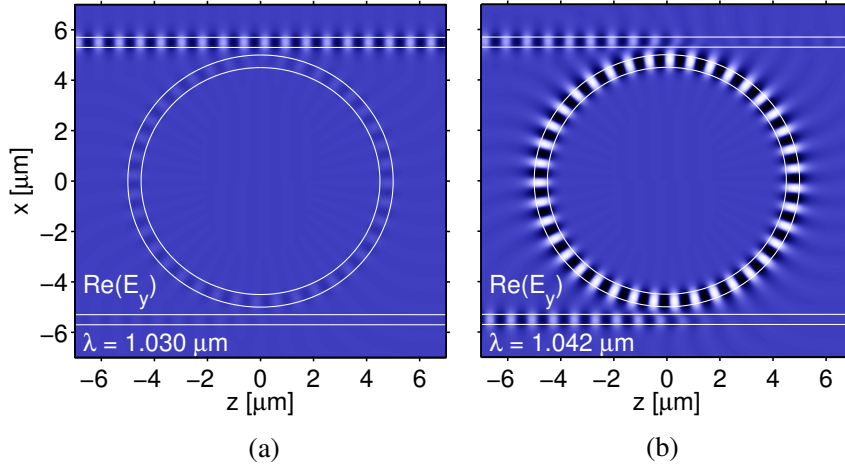


Figure 1.2: Off-resonance state (a) and resonance state (b) of a microresonator. The figure shows the real physical y component of TE polarized electrical field for a microresonator as considered in Section 4.4.1 with a cavity radius of $5 \mu\text{m}$ and gap widths of $0.3 \mu\text{m}$.

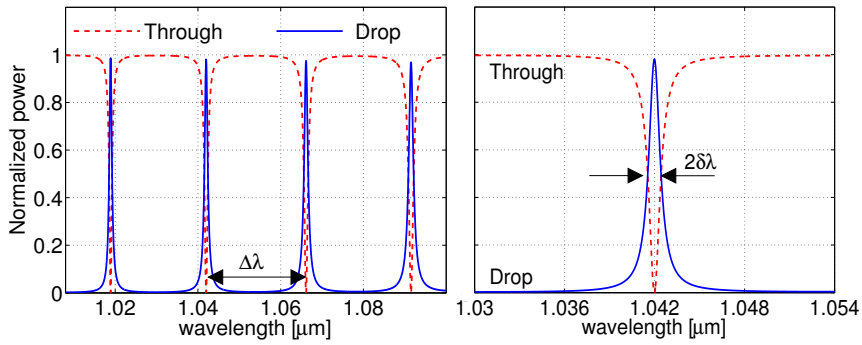


Figure 1.3: Wavelength dependent response of the microresonator as introduced in Fig. 1.2. Characterizing quantities of this spectral response are the free spectral range $\Delta\lambda = 0.02 \mu\text{m}$, the full width at half maximum $2\delta\lambda = 0.9 \text{ nm}$, the finesse $F = 22$, and the quality factor $Q = 1158$. These quantities are explained in detail in Section 1.4.4.

1.4 Ring-resonator theory

For the sake of further understanding, consider the typical abstract setting of a horizontally coupled circular microresonator as sketched in Figure 1.4. Two straight waveguides are evanescently coupled to the cavity. For “well confined” modes of the straight waveguide and cavity, one can expect that the interaction between the cavity modes and the port waveguide modes is localized around the region of the closest approach. Hence the device is functionally decomposed into two bent-straight waveguide couplers (I and II), which are connected to each other by the cavity segments, i.e. by pieces of bent waveguides. External connections are provided by the straight waveguides.

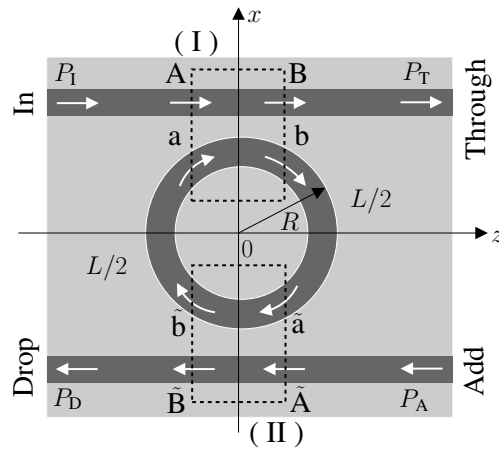


Figure 1.4: Functional decomposition of a microresonator into bent-straight waveguide couplers (shown by the dashed rectangles I and II), with the straight waveguide and the bent waveguide connections.

In this setting, as explained in the following paragraphs, the prediction of the spectral response of the resonator requires a description of the light propagation along the cavity segments, the analysis of the response of the bent-straight waveguide couplers, and finally a framework to combine these individual modules to predict the drop- and through-power. The subsequent discussion in this section is meant for structures involving monomodal straight waveguides and ring cavity. In Chapter 4, we extend it to the multimodal setting.

1.4.1 “Standard model” for resonators: Monomode setting

The “standard resonator model” [34, 35] describes the frequency domain propagation of light inside the resonator. In this model, the optical field with vacuum wavelength λ oscillates everywhere in time according to $\exp(i\omega t)$, where $\omega = kc$ is real angular frequency, $k = 2\pi/\lambda$ is the vacuum wavenumber, and c is the vacuum speed of light. The model is based on the following approximations and assumptions:

- For simplicity, we here assume that all waveguides are monomodal and all modes are of same polarization.
- The waveguides are made of linear and nonmagnetic materials. The attenuation of the cavity fields is incorporated into the complex valued cavity mode propagation constant.
- The bent-straight waveguide couplers considered here are “adiabatic”. Thus backreflections are negligible inside the couplers and the cavity segments.
- Outside the coupler regions, there is negligible “interaction” between the fields of the straight waveguides and the cavity.
- For further simplification, we assume that the resonator is symmetrical with respect to the x and z axes (see Figure 1.4).

Thus, the microresonator model under consideration consists of two identical bent-straight waveguide couplers (coupler I and coupler II) which are connected to each other by two segments of the cavity waveguide of length $L/2$. The external ports are constituted by straight waveguides. Variables $A, B, \tilde{A}, \tilde{B}$ (external connections) and $a, b, \tilde{a}, \tilde{b}$ (cavity connections) denote the amplitudes of properly normalized guided modes in the respective coupler port planes, which are identified by corresponding letters.

The response of the couplers is characterized by a scattering matrix \mathbf{S} . For the coupler I and II, the relationship between coupler input and output amplitudes is given by

$$\begin{pmatrix} b \\ B \end{pmatrix} = \mathbf{S} \begin{pmatrix} a \\ A \end{pmatrix}, \quad \begin{pmatrix} \tilde{b} \\ \tilde{B} \end{pmatrix} = \mathbf{S} \begin{pmatrix} \tilde{a} \\ \tilde{A} \end{pmatrix}, \quad \text{with} \quad \mathbf{S} = \begin{pmatrix} S_{bb} & S_{bs} \\ S_{sb} & S_{ss} \end{pmatrix}. \quad (1.1)$$

The entry $S_{v,w}$ with $v, w = b, s$ represents the “coupling” from the mode of waveguide w to the mode of waveguide v . Thus S_{bb}, S_{ss} are “self coupling coefficients”,

and S_{bs} , S_{sb} are “cross coupling coefficients”. Note that, here the matrix \mathbf{S} is not assumed to be unitary. Losses, e. g. due to power transfer to radiative (non-guided) parts of the optical field in the coupler region, can thus be incorporated in \mathbf{S} .

The (lossy) mode of the cavity waveguide is characterized by a complex valued cavity mode propagation constant $\gamma = \beta - i\alpha$, where β is the phase constant and α is the attenuation constant. Then for the propagation of the fields along the cavity segments, one writes

$$a = G\tilde{b}, \quad \tilde{a} = Gb, \quad \text{with} \quad G = e^{-i\beta L/2} e^{-\alpha L/2}. \quad (1.2)$$

1.4.2 Power transfer

Due to the linearity and the symmetry of the device, it is sufficient to consider an excitation in only one of the external ports, say port A . Given input amplitudes $A = \sqrt{P_1}$, $\tilde{A} = 0$, one is interested in the transmitted power $P_T = |B|^2$ and the dropped power $P_D = |\tilde{B}|^2$. By solving equations (1.1) and (1.2) for amplitudes B and \tilde{B} , one obtains

$$\tilde{B} = \left(\frac{S_{sb}S_{bs}G}{1 - S_{bb}^2G^2} \right) A, \quad B = \left(S_{ss} + \frac{S_{sb}S_{bs}S_{bb}G^2}{1 - S_{bb}^2G^2} \right) A. \quad (1.3)$$

Let $S_{bb} = |S_{bb}| e^{i\varphi}$, $S_{ss} - S_{bs}S_{sb}/S_{bb} = \rho e^{i\psi}$ with φ , ρ and ψ real. Then the dropped power is given by

$$P_D = P_1 \frac{|S_{sb}|^2 |S_{bs}|^2 e^{-\alpha L}}{1 + |S_{bb}|^4 e^{-2\alpha L} - 2|S_{bb}|^2 e^{-\alpha L} \cos(\beta L - 2\varphi)}, \quad (1.4)$$

and the through power is given by

$$P_T = P_1 \frac{|S_{ss}|^2 (1 + |S_{bb}|^2 \rho^2 e^{-2\alpha L} - 2|S_{bb}| \rho e^{-\alpha L} \cos(\beta L - \varphi - \psi))}{1 + |S_{bb}|^4 e^{-2\alpha L} - 2|S_{bb}|^2 e^{-\alpha L} \cos(\beta L - 2\varphi)}. \quad (1.5)$$

Here L is the total length of those parts of the cavity which are not already included in the couplers. According to equations (1.4) and (1.5), one can evaluate the throughput power and the dropped power, if the scattering matrix \mathbf{S} and the cavity propagation constant γ are available.

1.4.3 Resonances

In principle, all quantities that enter expressions (1.3), (1.4), (1.5) are wavelength dependent. Hence the proper way to compute the resonator spectrum would be to evaluate all relevant quantities in these expressions for a series of wavelengths.

A little more insight can be obtained if one accepts the approximation that if only a narrow wavelength interval needs to be considered, then the significant changes in the drop power and through power originate “exclusively” from the cosine terms in Equations (1.4), (1.5) that include the phase information.

To take into account the nonnegligible length l of the cavity segments in the coupler regions, write the phase term as $\beta L - 2\varphi = \beta L_{\text{cav}} - \phi$, where $L_{\text{cav}} = 2\pi R$ is the complete cavity length, and $\phi = 2\beta l + 2\varphi$ (a corresponding procedure is also applied to the phase term in the numerator of Equation (1.5)). Further consider only the wavelength dependence of the propagation constant β as it appears explicitly in the term $\beta L_{\text{cav}} - \phi$. In this way, one incorporates the wavelength dependence of the phase change βL_{cav} for the entire cavity, but disregards the wavelength dependence of the phase change ϕ that is introduced by the interaction with the port waveguides.

With the above approximation, resonances (i.e. maxima of the dropped power) are now characterized by singularities in the denominators of Equations (1.4), (1.5), which occur if $\cos(\beta L_{\text{cav}} - \phi) = 1$. This leads to the condition

$$\beta = \frac{2m\pi + \phi}{L_{\text{cav}}} =: \beta_m, \quad \text{for integer } m. \quad (1.6)$$

For a resonant configuration, the dropped power is given by

$$P_{\text{D}}|_{\beta=\beta_m} = P_{\text{I}} \frac{|S_{\text{sb}}|^2 |S_{\text{bs}}|^2 e^{-\alpha L}}{(1 - |S_{\text{bb}}|^2 e^{-\alpha L})^2}. \quad (1.7)$$

Note that properly computed values of S_{sb} , S_{bs} and S_{bb} already include the losses along the parts of the cavity inside the couplers. Therefore L in the Equation (1.7) (and in those places of Equations (1.4), (1.5) where attenuation is concerned) must not be replaced by L_{cav} .

In Chapter 4, we verify the validity of the above outlined approximation. As we shall see in the subsequent paragraphs, it provides quite useful insight into the spectral response of microresonators.

1.4.4 Resonance characteristics

As shown in Figure 1.3, the performance of resonators can be measured in terms of the free spectral range, the full width at half maximum, the finesse, and the quality factor. Here we derive (approximate) expressions for these characterizing quantities.

Free spectral range

The free spectral range (FSR) is defined as the wavelength difference $\Delta\lambda$ between two successive maxima of the dropped power (or minima of the through power).

The resonant configuration next to a resonance found for β_m is approximated as

$$\beta_{m-1} = \frac{2(m-1)\pi + \phi}{L_{\text{cav}}} = \beta_m - \frac{2\pi}{L_{\text{cav}}} \approx \beta_m + \left. \frac{\partial\beta}{\partial\lambda} \right|_m \Delta\lambda \quad (1.8)$$

where the right hand side is obtained as a first order Taylor series expansion for the propagation constant around the m 'th resonance wavelength; $\Delta\lambda$ is the difference between the vacuum wavelengths corresponding to the two resonant configurations.

By virtue of homogeneity arguments [36] for the propagation constants $\beta(\lambda, q_j)$, viewed as a function of the wavelength λ and all geometrical parameters q_j that define the cavity waveguide cross section, one finds

$$\frac{\partial\beta}{\partial\lambda} = -\frac{1}{\lambda} \left(\beta + \sum_j q_j \frac{\partial\beta}{\partial q_j} \right) \approx -\frac{\beta}{\lambda} \quad (1.9)$$

for the wavelength dependence of the propagation constants in the cavity loop. The same (crude) approximation can be obtained if one writes the propagation constant in terms of vacuum wavenumber and effective mode index as $\beta = 2\pi n_{\text{eff}}/\lambda$ and neglects the wavelength dependence of the effective index:

$$\frac{\partial\beta}{\partial\lambda} = -\frac{\beta}{\lambda} + k \frac{\partial n_{\text{eff}}}{\partial\lambda} \approx -\frac{\beta}{\lambda}. \quad (1.10)$$

This leads to the expression

$$\Delta\lambda = -\frac{2\pi}{L_{\text{cav}}} \left(\left. \frac{\partial\beta}{\partial\lambda} \right|_m \right)^{-1} \approx \left. \frac{\lambda^2}{n_{\text{eff}} L_{\text{cav}}} \right|_m \quad (1.11)$$

for the free spectral range (FSR) $\Delta\lambda$ of the resonator around the resonance of order m that is associated with the wavelength λ and the effective mode index $n_{\text{eff}} = \lambda\beta_m/2\pi$ of the cavity waveguide.

A more accurate and still simple expression can be obtained if one does not introduce the approximations (1.9), (1.10), i.e. if the wavelength dependence of β or n_{eff} is explicitly incorporated. Customarily one can write

$$\frac{\partial\beta}{\partial\lambda} = -\frac{k}{\lambda}n_{\text{eff, g}} \quad \text{with } n_{\text{eff, g}} = n_{\text{eff}} - \lambda\frac{\partial n_{\text{eff}}}{\partial\lambda}, \quad (1.12)$$

where $n_{\text{eff, g}}$ is the group effective index of the cavity mode [35]. Then the free spectral range is given by

$$\Delta\lambda = \frac{\lambda^2}{n_{\text{eff, g}}L_{\text{cav}}}. \quad (1.13)$$

Full width at half maximum

The full width at half maximum (FWHM) is a measure of the sharpness of the resonance. As the name suggests, it is given as the width of the resonance peak where the power drops to half of the resonance value.

A configuration that drops about half of the maximum power is realized for a propagation constant $\beta + \delta\beta$ with $1/(1 + |S_{\text{bb}}|^4 e^{-2\alpha L} - 2|S_{\text{bb}}|^2 e^{-\alpha L} \cos(\beta L_{\text{cav}} - 2\phi)) = 2/(1 + |S_{\text{bb}}|^4 e^{-2\alpha L} - 2|S_{\text{bb}}|^2 e^{-\alpha L} \cos(\beta L_{\text{cav}} + \delta\beta L_{\text{cav}} - 2\phi))$. Using the second order approximation of the cosine terms around a resonant cavity propagation constant, one obtains

$$\delta\beta = \pm \frac{1}{L_{\text{cav}}} \left(\frac{1}{|S_{\text{bb}}|} e^{\alpha L/2} - |S_{\text{bb}}| e^{-\alpha L/2} \right) \quad (1.14)$$

for the shift in the propagation constants that distinguishes configurations with the maximum and half of the maximum dropped power.

Using an approximation $\delta\beta \approx -(\beta_m/\lambda)\delta\lambda$, analogous to Equations (1.9),(1.10), Equation (1.14) leads to an expression

$$2\delta\lambda = \frac{\lambda^2}{\pi L_{\text{cav}} n_{\text{eff}} \Big|_m} \left(\frac{1}{|S_{\text{bb}}|} e^{\alpha L/2} - |S_{\text{bb}}| e^{-\alpha L/2} \right) \quad (1.15)$$

which gives the full width at half maximum $2\delta\lambda$ of the resonance of order m .

Finesse and quality factor

The finesse F of the resonator is defined as the ratio of the free spectral range and the full width at half maximum of a resonance for a specific resonance wavelength. With the FSR and the FWHM given by Equations (1.11), (1.15), for the present model the finesse is given by

$$F = \frac{\Delta\lambda}{2\delta\lambda} = \pi \frac{|S_{bb}|e^{-\alpha L/2}}{1 - |S_{bb}|^2e^{-\alpha L}}. \quad (1.16)$$

The ability of the cavity to confine the field is described by the quality factor Q . It is a measure of the sharpness of the transmission peak and defined as the ratio of the resonance wavelength to the full width at half maximum ²:

$$Q = \frac{\lambda}{2\delta\lambda} = \pi \frac{n_{\text{eff}}L_{\text{cav}}}{\lambda} \frac{|S_{bb}|e^{-\alpha L/2}}{1 - |S_{bb}|^2e^{-\alpha L}} = \frac{n_{\text{eff}}L_{\text{cav}}}{\lambda} F. \quad (1.17)$$

For a circular resonator with radius R and cavity length $L_{\text{cav}} = 2\pi R$, one obtains

$$Q = kRn_{\text{eff}}F \quad (1.18)$$

for the relationship between Q and finesse F .

As before, the approximations according to Equations (1.9), (1.10) can be avoided by substituting the effective cavity mode index n_{eff} in Equations (1.15), (1.17) by the effective group mode index $n_{\text{eff, g}}$ as defined in Equation (1.12).

1.4.5 Tuning

The realization and actual performance of the resonators are constrained by several factors, e.g. an accurate definition of the resonance wavelengths requires a high degree control of the geometrical parameters, temperature dependant changes in the material parameters detune the spectral response. Active (e.g. electro-optical, thermo-optical) tuning of the resonators greatly relaxes these constraints. This is quite essential for stable performance of the devices. See Ref. [38] and the references quoted there for further details. Here we outline a framework for the modeling of tuning.

²In a time domain setting, the Q factor is defined as the ratio of the optical power stored in the cavity to the cycle averaged power radiated out of the cavity [37]. Therefore the larger the Q factor, the longer the optical field is trapped inside the cavity.

As explained in Section 1.4.3, at resonance the condition $\beta = (2m\pi + \phi)/L_{\text{cav}} = \beta_m$ holds for the cavity mode propagation constant, where the integer m gives the order of the resonance. Assume that the wavelength dependence of the propagation constant $\beta = \beta(\lambda)$ is given. Then one can write $\beta(\lambda_m) = \beta_m$, where λ_m is the resonance wavelength associated with the resonant cavity mode propagation constant β_m .

Disregarding its influence on the response of the (short) couplers as a first approximation, a tuning mechanism is modeled by a parameter p , which affects mainly the field propagation along the cavity. Thus now, besides the wavelength, the cavity mode propagation constant also depends on the tuning parameter, i.e. $\beta = \beta(p, \lambda)$, with $p = 0$ representing the original state: $\beta(0, \lambda_m) = \beta_m$.

With the tuning applied, the resonance of order m is shifted towards a new wavelength $\tilde{\lambda}_m$, such that $\beta(p, \tilde{\lambda}_m) = (2m\pi + \phi)/L_{\text{cav}} \stackrel{!}{=} \beta_m$ is satisfied again. A linear approximation in the tuning parameter and in the wavelength differences

$$\beta(p, \tilde{\lambda}_m) \approx \beta(0, \lambda_m) + p \left. \frac{\partial \beta}{\partial p} \right|_{0, \lambda_m} + (\tilde{\lambda}_m - \lambda_m) \left. \frac{\partial \beta}{\partial \lambda} \right|_{0, \lambda_m} \stackrel{!}{=} \beta_m \quad (1.19)$$

leads to an expression for the shift in the wavelength $\Delta_p \lambda_m = \tilde{\lambda}_m - \lambda_m$ that is affected by the tuning mechanism

$$\Delta_p \lambda_m = -p \left(\frac{\partial \beta}{\partial p} \right) \left(\frac{\partial \beta}{\partial \lambda} \right)^{-1} \Big|_{0, \lambda_m}, \quad (1.20)$$

which on simplification by using Equation (1.9) leads to

$$\Delta_p \lambda_m = p \frac{\partial \beta}{\partial p} \frac{\lambda_m}{\beta_m} \quad \text{or} \quad \Delta_p \lambda_m = p \frac{\partial \beta}{\partial p} \frac{\lambda_m^2}{2\pi n_{\text{eff},m}}, \quad (1.21)$$

i.e. the wavelength shift compensates the change in the cavity mode propagation constant due to a nonzero perturbation strength p . Note that the wavelength shift does not depend on the length of the cavity. If available, the effective group index $n_{\text{eff},g}$ according to Equation (1.12) can replace the effective index n_{eff} in Equation (1.21).

We are specifically interested in tuning effected by the change of the cavity core permittivity (i.e. refractive index). For further details about this, see Section 2.5 and Section 4.6.

1.5 Existing approaches for modeling of circular micro-resonators

From the abstract resonator theory discussed in Section 1.4, it is clear that the spectral response of the microresonators depends on the propagation of electromagnetic fields along the cavity, and the coupling between the cavity and the straight waveguides. In turn, these quantities are influenced by the geometrical parameters like the size of the cavity, the gap widths between the cavity and the straight waveguides, and by material parameters like refractive indices³. Several analytical, parametrical, pure numerical, and mixed analytical-numerical models have been proposed for the analysis of these structures.

Proper understanding of the propagation of electromagnetic fields along the cavity is very important, because the behavior of these fields is mainly responsible for the resonances in the spectral response. This is systematically explained by a time domain model of isolated (circular) cavities in terms of integer valued angular mode number and complex valued eigenfrequencies [39, 40, 41]. But in case of the present resonators, the cavity is coupled to the external straight waveguides. These waveguides are usually modeled in terms of given real valued frequency [42, 43]. Thus, to study a cavity coupled to straight waveguides, a complex eigenfrequency model of (isolated) cavities is not the most suitable choice. Problems for the description of the coupling arise from the radially growing field solutions of the time domain cavity modes [39, 40]. Nevertheless, attempts are made to study analytically the above coupling by combining a complex eigenfrequency model of the cavities with a real valued frequency model of the straight waveguides [41, 44].

To avoid such juggling of viewpoints, either parametrical or ab initio frequency domain models are used. While very few studies exist about ab initio models, parametrical models, such as discussed in Section 1.4, are quite popular, e.g. see [33, 45, 46, 47]. Treating the (complex valued) cavity mode propagation constants and the coupler scattering matrices (which parameterize the interaction between the cavity and the straight waveguide in terms of coupling coefficients) as free parameters, one can qualitatively analyze the effects of the above parameters on the spectral response. Under simplifying assumptions of a lossless coupler and unidirectional monomode wave propagation, universal relations for the coupling of optical power between a cavity ring and one bus waveguide are derived in [48]. In Ref. [38] a detailed procedure of fitting these free parameters in the ring-resonator model to experimental measurements is outlined. But when it comes to the design

³ Other factors like anisotropy, material attenuation, side wall roughness play a role in real devices, but these are out of scope of the present work.

of microresonators, one must know how to determine systematically these free parameters, given the geometrical and material properties of the device.

The coupling between a circular cavity and a straight waveguide has been modeled with phenomenologically derived expressions for the coupling coefficient [22], with integral equations based on Green's functions [49], and with different versions of coupled mode theory. Coupled mode theory [50, 51, 52] proved to be a quite useful tool for the analysis of the interaction between straight waveguides. Motivated by this success, in Ref. [44] space dependent coupled mode theory has been used to model the coupling between a curved waveguide and a straight waveguide. That approach is based on a complex eigenfrequency model of the cavities. Also the coupled mode equations are derived phenomenologically. As another variant, time dependent coupled mode theory was also attempted [22, 53].

Concerning the modeling of three dimensional microresonators, by using the effective index method certain 3-D settings can be reduced to 2-D, which are then analyzed by means of phenomenologically derived expressions for the coupling coefficients [33] or by conformal mapping method [54].

Apart from the above analytical and parametrical methods, pure numerical methods like Finite Difference Time Domain (FDTD) [55, 56] are also used for the simulation of microresonators. In Ref. [57] a finite difference based Helmholtz solver is used to compute the spectral response of 2-D microdisk resonators. Even for the 2-D setting, pure numerical methods turn out to be time consuming, and these become prohibitively time consuming in case of the 3-D setting. These numerical models are generally reserved for benchmarking of the results obtained with other techniques, not for practical design work.

Finally one should emphasize that specific 2-D configurations can be treated in an accurate and highly efficient analytical way in terms of integral equations [58]. This concerns eigenvalue [59, 60] and scattering problems [61, 62] for micro-ring and disk cavities with regular deformations, in the vicinity of one straight dielectric waveguide or half-block. Unfortunately, the extension to 3-D appears to be far from obvious.

1.6 Scope of the thesis

With the growing importance of microresonators for a variety of applications, it becomes necessary to devise a model which is directly interpretable in physical terms, and which is essentially free of any fit parameters. Moreover, the numerical implementation should not be computationally time consuming and resource

intensive. These are the desirable features for a microresonator model from the viewpoint of device design and interpretation of experimental results.

The present work remains in the scope of classical optics, on the basis of the Maxwell equations. Referring to the classification of resonator types given in [53], in this thesis we treat the circular microcavities as traveling wave resonators in the framework of a pure frequency domain description. For modeling purposes, we adopt the functional decomposition as outlined by the “standard model” in Section 1.4. The advantage of such a decomposition is that the analysis of microresonators reduces to the modeling of straight waveguides and bent waveguides, and the modeling of bent-straight waveguide couplers. Out of this, models for straight waveguides are quite well established, and sophisticated numerical tools for their analysis exist already ⁴.

The decomposition approach of the “standard model” is well known in the literature [35, 46, 47], where it is typically presented as a parametrical model. For qualitative study of the spectral response of microresonators, such a parametrical model is sufficient. But from the design point of view, it is rather inadequate. The numerical implementation of such model requires the propagation constants of the cavity segment modes, and the coupling coefficients of the bent-straight waveguide couplers.

The real valued frequency domain model of the wave propagation along bent waveguides or curved interfaces (i.e. cavity segments) is well known [10, 63, 64]. For recent work on this topic, see Refs. [65, 66, 67, 68]. But due to the difficulties associated with complex order Bessel functions, this approach is hardly ever pursued in detail. Important issues like computing bend modes and their propagation constants (especially for very small bent radii), or the mode normalization still require proper attention.

To some degree, the time domain and the frequency domain viewpoints for propagation of the cavity modes are equivalent, and results obtained with one model can be interpreted in the framework of the other model [40, 44]. But this switching of viewpoints is not straightforward, and it leads to a few rather obscure issues like the nature of cavity fields at infinity, or the issue of “phase matching” for the coupling between the cavity fields and the straight waveguide fields. As commented in Section 1.5, a model of bent-straight waveguide couplers is lacking, which is consistent in terms of physical notions and based on rigorous mathematical concepts.

A major part of the work presented in this thesis is centered around topics re-

⁴For the present work, we use 2-D straight waveguide mode solver by Dr. Manfred Hammer. See www.math.utwente.nl/hammer/Metric/ for further details.

lated to the wave propagation along curved interfaces. We establish a model for bent-straight waveguide couplers with a sound mathematical foundation, that is consistent with the physical notions. We derive the governing equations from first principles. Going beyond the mere abstract theoretical model, another objective of this work is the reliable and efficient numerical implementation of the approach. We will also address this issue in the present work.

To investigate feasibility and scope of the above approach, in this thesis we restrict ourself to the modeling of 2-D microresonators. Naturally, we discuss only horizontally coupled devices. The theory, however, has been formulated such that an extension to the 3-D setting (including the vertically coupled case) can follow the same line of arguments [69].

1.7 Outline of the thesis

This thesis is based on our contributions to the project NAIS concerning the modeling and simulation of microresonators as tunable wavelength filters. Here we investigate a frequency domain spatial coupled mode theory based model of 2-D circular integrated optical microresonators. The formulation requires the propagation constants of the cavity segment (bent waveguide) modes and the scattering matrices of the bent-straight waveguide couplers. The former quantities characterize the wave propagation along the cavity segments, and the latter quantities characterize the response of the couplers. We proceed as follows:

- Chapter 2 explores the classical frequency domain model of the wave propagation along curved interfaces. We implemented routines for complex order Bessel functions, which allow to compute the bend modes and their propagation constants, and also to visualize the bend field propagation.
- Chapter 3 presents a parameter-free spatial coupled mode theory model of bent-straight waveguide couplers derived from variational principles. With access to the analytical bent waveguide modes, we could implement the above model, and investigate it systematically.
- Chapter 4 describes in detail the 2-D model for circular microresonators, and explains how to evaluate effectively their spectral response. Tunability of microresonators is an essential feature from the application point of view. This chapter also describes how the effect of small changes of the cavity refractive index on the spectral response of the resonators can be estimated by perturbational expressions.
- Chapter 5 contains the conclusions of the present work and a brief outlook.

1.8 Publications

The work presented in this thesis has been accompanied by the following publications.

1. K. R. Hiremath, R. Stoffer, and M. Hammer. Coupled mode theory and FDTD simulations on coupling between bend and straight optical waveguides. In *Proceedings of 8'th Annual Symposium of IEEE/LEOS Benelux Chapter*, pages 33–36, 2003.
2. M. Hammer, K. R. Hiremath, and R. Stoffer. Analytical approaches to the description of optical microresonator devices. In M. Bertolotti, A. Driessen, and F. Michelotti, editors, *Microresonators as building blocks for VLSI photonics*, volume 709 of AIP conference proceedings, pages 48–71. American Institute of Physics, Melville, New York, 2004.
3. R. Stoffer, K. R. Hiremath, and M. Hammer. Comparison of coupled mode theory and FDTD simulations of coupling between bent and straight optical waveguides. In M. Bertolotti, A. Driessen, and F. Michelotti, editors, *Microresonators as building blocks for VLSI photonics*, volume 709 of AIP conference proceedings, pages 366–377. American Institute of Physics, Melville, New York, 2004.
4. K. R. Hiremath, R. Stoffer, and M. Hammer. Multimode circular integrated optical microresonators: Coupled mode theory modeling. In *Proceedings of 9'th Annual Symposium of IEEE/LEOS Benelux Chapter*, pages 79–82, 2004.
5. K. R. Hiremath, M. Hammer, S. Stoffer, L. Prkna, and J. Čtyroký. Analytic approach to dielectric optical bent slab waveguides. *Optical and Quantum Electronics*, 37(1-3):37–61, January 2005.
6. K. R. Hiremath, R. Stoffer, M. Hammer. Modeling of circular integrated optical microresonators by 2-D frequency domain coupled mode theory. *Optics Communications*, 2005 (accepted).
7. R. Stoffer, K. R. Hiremath, M. Hammer, L. Prkna, and J. Čtyroký. Cylindrical integrated optical microresonators: Modeling by 3-D vectorial coupled mode theory. *Optics Communications*, 2005 (accepted).

Chapter 2

Analytic approach to dielectric optical bent slab waveguides

A rigorous classical analytic model of confined optical wave propagation along 2-D bent slab waveguides and curved dielectric interfaces is investigated, based on a piecewise frequency domain ansatz for bend mode profiles in terms of Bessel and Hankel functions. This approach provides a clear picture of the behaviour of bend modes, concerning their decay for large radial arguments or effects of varying bend radius. Fast and accurate routines are required to evaluate Bessel functions with large complex orders and large arguments. Our implementation enabled detailed studies of bent waveguide properties, including higher order bend modes and whispering gallery modes, their interference patterns, and issues related to bend mode normalization and orthogonality properties. Also a perturbational expression is derived for the shift in the propagation constant due to changes in the core refractive index.

Parts of this chapter are adapted from:

K. R. Hiremath, M. Hammer, S. Stoffer, L. Prkna, and J. Čtyroký. *Analytic approach to dielectric optical bent slab waveguides*. *Optical and Quantum Electronics*, 37(1-3):37–61, January 2005.

Bent dielectric waveguides play an important role in photonic integrated circuits. Accurate evaluation of mode profiles, phase propagation constants, and of optical losses associated with the leaky wave propagation is the central task for theoretical modeling of the curved structures. The present work on this – rather old – topic is motivated by the recent interest in circular optical microresonator devices as building blocks for large-scale integrated optics [22, 31]. During our participation in a related European project [32], we experienced that certain notions about the properties of bend modes deserved clarification. This concerns e.g. the behaviour of the mode profiles for large radial coordinates, profile integrability, mode orthogonality, or a clear picture of propagation and interference of the bend modes.¹

A sound modal analysis of bent slabs becomes particularly relevant if the mode profiles are to be employed as basis fields for a description of integrated optical microresonators with circular, ring- or disk-shaped cavities. In a framework of coupled mode theory [33, 70, 44], an as far as possible analytic representation of the basic field profiles on a radially unbounded domain must be regarded as highly advantageous. This is provided by the approach of this chapter. Preliminary promising studies on CMT modeling of circular resonators are contained in [34, 71, 72]; further details follow in Chapters 3, 4.

This chapter presents an analytical model of (2-D) bent waveguides. Using the uniform asymptotic expansions of Bessel/Hankel functions as provided in Ref. [73, 74], we found that with present standard computers it is not a problem to carry out the rigorous analytic evaluation of the problem. Details on the implementation of Bessel and Hankel functions are given in Section 2.3. See Refs. [67, 68, 75], for steps towards a 3-D generalization of the present 2-D model.

In Section 2.1 various methods for modeling of bent waveguides are briefly reviewed. Section 2.2 introduces the bend mode ansatz and outlines the analytic steps towards a solution. Remarks on bend mode normalization, on orthogonality properties of bend modes are added in Sections 2.2.1, 2.2.2. Section 2.4 summarizes the results of the analytic model for a series of bend configurations including higher order modes, and modes which are “effectively” guided by just one dielectric interface. Wherever benchmark results are available, the present analytical results are compared with them. In Section 2.5 a perturbational analysis of the effect of changes in the core refractive index on the propagation constants is carried out.

¹Partly these notions originate from the use of a ray picture for the description of bent waveguides, or from approximate models in terms of “equivalent” leaky straight waveguide profiles. We will avoid these viewpoints in the present work.

2.1 Existing approaches for modeling of bent waveguides

Initial frequency domain models of optical bent waveguides can be found in Ref. [10, 63]. Since then, various different techniques were applied to the task. In Refs. [76, 77] a method for the calculation of bend mode losses is presented, based on ray path notions from geometrical optics. By conformal mapping [78, 79], the bent waveguide problem can be transformed into equations for a (leaky) straight waveguide. In Ref. [80] conformal mapping with perfectly matched layer (PML) boundary conditions is used to analyze bent waveguides. In a perturbational approach [81] the curvature is treated as a perturbation of a straight waveguide, and the bent waveguide modes are expressed in terms of straight waveguide fields. Other techniques of a more analytical character (e.g. WKB approximations [82], a transfer matrix approach [83]), or of a numerical nature (e.g. beam propagation [84], the method of lines [85], finite difference [86] or finite element discretizations [87]) are applied as well.

The pure analytic approach for modeling of optical bent slab waveguides is quite well known [10, 63, 64, 65, 66, 88, 43], though apparently hardly ever evaluated rigorously, especially for bent waveguides with small radii. When trying to do so, a major obstacle is encountered in the form of the necessity to compute Bessel functions of large complex order and large argument; we experienced that efficient facilities for these function evaluations are not provided by the standard numerical libraries. To overcome that hindrance, most authors resorted to approximations of the problem, such that reliable results for bent slab waveguides, e.g. for the purpose of a bend mode solver benchmark, still seem to be rare.

Alternatively, one can consider time-domain resonances that are supported by full circular cavities. In that viewpoint, the field solutions are parameterized by an integer azimuthal index; the frequency takes the role of a complex valued eigenvalue. Any difficulties with the complex order Bessel functions are avoided in that way, and the values for frequencies and propagation constants can be largely translated between the two viewpoints [39]. However, the field solutions obtained in the latter way are not directly useful for applications, where one is interested in pieces of bent waveguides only. Also, for a microresonator model that combines modal solutions for bent and straight waveguides by means of coupled mode theory integrals, the fixed-frequency bend mode profiles as discussed in this chapter are required.

The present discussion is concerned with a frequency domain model, where the (real valued) frequency or vacuum wavelength is regarded as a given parameter, and one is interested in solutions of the Maxwell equations for wave propagation along angular segments of the curved structures, that are characterized by a complex valued propagation constant.

2.2 Bent waveguide model

Consider a bent slab waveguide with the y -axis as the axis of symmetry as shown in Figure 2.1. We assume that the material properties and the fields do not vary in the y -direction. Being specified by the radially dependent refractive index $n(r)$ (here n is piecewise constant), the waveguide can be seen as a structure that is homogeneous along the angular coordinate θ . Hence one chooses an ansatz for the bend modes with pure exponential dependence on the azimuthal angle, where the angular mode number is commonly written as a product γR with a reasonably defined bend radius R , such that γ can be interpreted as a propagation constant.

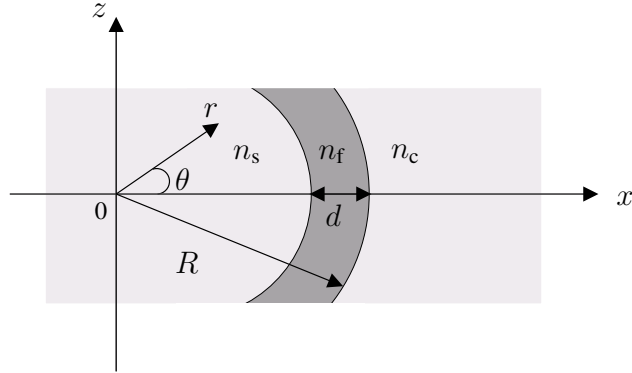


Figure 2.1: A bent slab waveguide. The core of thickness d and refractive index n_f is embedded between an interior medium (“substrate”) with refractive index n_s and an exterior medium (“cladding”) with refractive index n_c . The distance between the origin and the outer rim of the bend defines the bend radius R .

In the cylindrical coordinate system (r, θ) , the functional form (in the usual complex notation) of the propagating electric field \mathbf{E} and the magnetic field \mathbf{H} reads

$$\begin{aligned} \mathbf{E}(r, \theta, t) &= (\tilde{E}_r, \tilde{E}_y, \tilde{E}_\theta)(r) e^{i(\omega t - \gamma R \theta)}, \\ \mathbf{H}(r, \theta, t) &= (\tilde{H}_r, \tilde{H}_y, \tilde{H}_\theta)(r) e^{i(\omega t - \gamma R \theta)}, \end{aligned} \quad (2.1)$$

where the \sim symbol indicates the mode profile, γ is the propagation constant of the bend mode, and ω is the angular frequency corresponding to vacuum wavelength λ . Since an electromagnetic field propagating through a bent waveguide loses energy due to radiation [88], γ is complex valued, denoted as $\gamma = \beta - i\alpha$, where β and α are the real valued phase propagation and attenuation constants.

Note that the angular behaviour of the field (2.1) is determined by the product

γR , where the definition of R is entirely arbitrary. Given a bend mode, the values assigned to the propagation constant γ change, if the same physical solution is described by using different definitions of the bend radius R . We will add a few more comments on this issue in Section 2.4. The definition of the bend radius R as the radial position of the outer interface of the core layer is still applicable in case the guiding is effected by a single dielectric interface only, i.e. for the description of whispering gallery modes (see Section 2.4.5). Hence, for this paper we stick to the definition of R as introduced in Figure 2.1.

If the ansatz (2.1) is inserted into the Maxwell equations, one obtains the two separate sets of equations

$$\left. \begin{aligned} \frac{\gamma R}{r} \tilde{E}_y &= -\mu_0 \omega \tilde{H}_r, \\ \frac{\partial \tilde{E}_y}{\partial r} &= -i\mu_0 \omega \tilde{H}_\theta, \\ \frac{1}{r} \frac{\partial r \tilde{H}_\theta}{\partial r} + \frac{i\gamma R}{r} \tilde{H}_r &= -i\epsilon_0 \epsilon \omega \tilde{E}_y \end{aligned} \right\} \text{TE} \quad (2.2)$$

and

$$\left. \begin{aligned} \frac{\gamma R}{r} \tilde{H}_y &= \epsilon_0 \epsilon \omega \tilde{E}_r, \\ \frac{\partial \tilde{H}_y}{\partial r} &= i\epsilon_0 \epsilon \omega \tilde{E}_\theta, \\ \frac{1}{r} \frac{\partial r \tilde{E}_\theta}{\partial r} + \frac{i\gamma R}{r} \tilde{E}_r &= i\mu_0 \omega \tilde{H}_y, \end{aligned} \right\} \text{TM} \quad (2.3)$$

with vacuum permittivity ϵ_0 , vacuum permeability μ_0 , and the relative permittivity $\epsilon = n^2$.

For transverse electric (TE) waves the only nonzero components are \tilde{E}_y , \tilde{H}_r and \tilde{H}_θ , which are expressed in terms of \tilde{E}_y , while for transverse magnetic (TM) waves the only nonzero components are \tilde{H}_y , \tilde{E}_r and \tilde{E}_θ , which are given by \tilde{H}_y . Within radial intervals with constant refractive index n , the basic electric and magnetic components are governed by a Bessel equation with complex order γR ,

$$\frac{\partial^2 \phi}{\partial r^2} + \frac{1}{r} \frac{\partial \phi}{\partial r} + \left(n^2 k^2 - \frac{\gamma^2 R^2}{r^2} \right) \phi = 0 \quad (2.4)$$

for $\phi = \tilde{E}_y$ or $\phi = \tilde{H}_y$, where $k = 2\pi/\lambda$ is the (given, real) vacuum wavenumber. For TE modes, the interface conditions require continuity of \tilde{E}_y and of $\partial_r \tilde{E}_y$ across the dielectric interfaces. For TM modes, continuity of \tilde{H}_y and of $\epsilon^{-1} \partial_r \tilde{H}_y$ across the interfaces is required.

Eq. (2.4), together with the interface conditions and suitable boundary conditions for $r \rightarrow 0$ and $r \rightarrow \infty$, represents an eigenvalue problem with the bend mode profiles ϕ as eigenfunctions, and the propagation constants γ or angular mode numbers $\nu = \gamma R$ as eigenvalues. The equation is solved piecewise in the regions with constant refractive index. While the procedure is in principle applicable for arbitrary multilayer bent waveguides, for the sake of brevity we discuss here the three layer configuration as introduced in Figure 2.1.

The general solution of Eq. (2.4) is a linear combination of the Bessel functions of the first kind J and of the second kind Y . This representation is applicable to the core region. Since Y tends to $-\infty$ if $r \rightarrow 0$, for the boundedness of the electric/magnetic field at the origin one selects only the Bessel function of the first kind J for the interior region. In the outer region, we are looking for a complex superposition of J and Y that represents outgoing waves. Such a solution can be given in terms of the Hankel functions of the first kind $H^{(1)}$ or of the second kind $H^{(2)}$. Using the asymptotic expansions of these functions [73, chap. 9, Eq. (9.2.3), Eq. (9.2.4)]

$$\begin{aligned} H_\nu^{(1)}(nkr) &\sim \sqrt{\frac{2}{\pi nkr}} e^{i(nkr - \nu\pi/2 - \pi/4)}, \\ H_\nu^{(2)}(nkr) &\sim \sqrt{\frac{2}{\pi nkr}} e^{-i(nkr - \nu\pi/2 - \pi/4)}, \end{aligned} \quad (2.5)$$

and taking into account the harmonic time dependence $\exp(i\omega t)$ (with positive frequency), one observes that $H^{(1)}$ represents incoming waves, while outgoing waves are given by $H^{(2)}$. Thus the piecewise ansatz for the basic components of the electric/magnetic bent mode profile is

$$\phi(r) = \begin{cases} A_s J_\nu(n_s k r), & \text{if } 0 \leq r \leq R^-, \\ A_f J_\nu(n_f k r) + B_f Y_\nu(n_f k r), & \text{if } R^- \leq r \leq R^+, \\ A_c H_\nu^{(2)}(n_c k r), & \text{for } r \geq R^+, \end{cases} \quad (2.6)$$

where $R^- = R - d$, $R^+ = R$, and where A_s , A_f , B_f and A_c are so far unknown constants.

The polarization dependent interface conditions lead to a homogeneous system of linear equations for A_s , A_f , B_f and A_c . The condition for a nontrivial solution can be given the form

$$\frac{\frac{J_\nu(n_f k R^-)}{J_\nu(n_s k R^-)} - q_s \frac{J'_\nu(n_f k R^-)}{J'_\nu(n_s k R^-)}}{\frac{Y_\nu(n_f k R^-)}{J_\nu(n_s k R^-)} - q_s \frac{Y'_\nu(n_f k R^-)}{J'_\nu(n_s k R^-)}} = \frac{\frac{J_\nu(n_f k R^+)}{H_\nu^{(2)}(n_c k R^+)} - q_c \frac{J'_\nu(n_f k R^+)}{H_\nu^{(2)'}(n_c k R^+)}}{\frac{Y_\nu(n_f k R^+)}{H_\nu^{(2)}(n_c k R^+)} - q_c \frac{Y'_\nu(n_f k R^+)}{H_\nu^{(2)'}(n_c k R^+)}} \quad (2.7)$$

with $q_j = n_f/n_j$ for TE polarization, and with $q_j = n_j/n_f$ for TM polarized fields, for $j = s, c$. Eq. (2.7) is the dispersion equation for the three layer bent slab waveguide. For given frequency ω , this equation is to be solved² for the propagation constants $\gamma = \nu/R$.

For the numerical implementation, Eq. (2.7) is rearranged as

$$T_1 \cdot T_2 = T_3 \cdot T_4, \quad (2.8)$$

where

$$\begin{aligned} T_1 &= J_\nu(n_f k R^-) J'_\nu(n_s k R^-) - q_s J_\nu(n_s k R^-) J'_\nu(n_f k R^-), \\ T_2 &= Y_\nu(n_f k R^+) H_\nu^{(2)'}(n_c k R^+) - q_c H_\nu^{(2)}(n_c k R^+) Y'_\nu(n_f k R^+), \\ T_3 &= Y_\nu(n_f k R^-) J'_\nu(n_s k R^-) - q_s J_\nu(n_s k R^-) Y'_\nu(n_f k R^-), \\ T_4 &= J_\nu(n_f k R^+) H_\nu^{(2)'}(n_c k R^+) - q_c H_\nu^{(2)}(n_c k R^+) J'_\nu(n_f k R^+). \end{aligned}$$

In contrast to common notions about leaky modes, the fields obtained by the ansatz (2.6) do not diverge for large radial coordinate r . The asymptotic expansion (2.5) predicts a decay $\sim 1/\sqrt{r}$. No difficulties related to ‘large’ terms are to be expected for the numerical evaluation of Eq. (2.8). Moreover, as shown below, with the squared mode profile being accompanied by a factor r^{-1} in the relevant expression, the bend modes can even be normalized with respect to the azimuthal mode power.

2.2.1 Bend mode normalization

The power flow density associated with a bend mode is given by the time averaged Poynting vector $\mathbf{S}_{\text{av}} = \frac{1}{2} \Re(\mathbf{E} \times \mathbf{H}^*)$. The axial component $S_{\text{av},y}$ vanishes in the 2-D setting; for TE waves the radial and azimuthal components evaluate to

$$\begin{aligned} S_{\text{av},r} &= \frac{-1}{2\mu_0\omega} \Re \left[i \tilde{E}_y \frac{\partial \tilde{E}_y^*}{\partial r} \right] e^{-2\alpha R\theta}, \\ S_{\text{av},\theta} &= \frac{\beta}{2\mu_0\omega} \frac{R}{r} |\tilde{E}_y|^2 e^{-2\alpha R\theta}, \end{aligned} \quad (2.9)$$

²In an alternative approach, where one looks at time domain resonances of circular cavities, a similar procedure as outlined here [44, 39] leads to precisely the same equation (cf. the remarks in the introduction). In that case, Eq. (2.7) is to be solved for complex valued resonance frequencies ω , for given integer azimuthal mode numbers ν .

and for TM polarization one obtains

$$\begin{aligned}
 S_{\text{av},r} &= \frac{1}{2\epsilon_0\epsilon\omega} \Re \left[\tilde{H}_y^* \frac{\partial \tilde{H}_y}{\partial r} \right] e^{-2\alpha R\theta}, \\
 S_{\text{av},\theta} &= \frac{\beta}{2\epsilon_0\epsilon\omega} \frac{R}{r} |\tilde{H}_y|^2 e^{-2\alpha R\theta}.
 \end{aligned} \tag{2.10}$$

The total optical power transported by the mode in the angular direction is given by $P_\theta(\theta) = \int_0^\infty S_{\text{av},\theta} dr$. Somewhat surprisingly, this expression can be considerably simplified by using the following formula [89, Section 11.2, Eq. 5],

$$\int C_\mu(kx) D_\nu(kx) \frac{dx}{x} = \frac{kx}{\mu^2 - \nu^2} \{ C_\mu(kx) D_{\nu+1}(kx) - C_{\mu+1}(kx) D_\nu(kx) \} + \frac{C_\mu(kx) D_\nu(kx)}{\mu + \nu} \tag{2.11}$$

where C_μ, D_ν are any cylindrical functions (i.e. functions which are linear combinations of J_μ and Y_μ , or of J_ν and Y_ν , respectively). Observing that for a valid mode profile the pieces of the ansatz (2.6) satisfy the polarization dependent continuity conditions at the dielectric interfaces, application of Eq. (2.11) and of several standard identities for Bessel functions leads to exact cancellation of the boundary terms that arise in the piecewise integration, with the exception of the limit term for $r \rightarrow \infty$. In that regime the mode profile is represented by the asymptotic form (2.5) of the relevant Hankel functions, such that one arrives at the two expressions

$$\begin{aligned}
 P_\theta(\theta) &= \frac{|A_c|^2}{2\mu_0\omega\alpha R\pi} e^{\alpha R(\pi - 2\theta)} \quad (\text{TE}), \\
 P_\theta(\theta) &= \frac{|A_c|^2}{2\epsilon_0 n_c^2 \omega \alpha R \pi} e^{\alpha R(\pi - 2\theta)} \quad (\text{TM}),
 \end{aligned} \tag{2.12}$$

for the modal power of TE and TM polarized modes, respectively. For certain well guided modes with extremely low losses, i.e. $\alpha \approx 0$, Eqs. (2.12) are not suitable for direct use. In this case, we compute the modal power by numerical integration of $P_\theta(\theta) = \int_0^\infty S_{\text{av},\theta} dr$ over a suitably chosen radial interval. All mode profiles shown in Section 2.4 are power normalized with respect to these expressions (evaluated at $\theta = 0$).

Alternatively, Eqs. (2.12) can be derived in a way quite analogous to what follows in Section 2.2.2: Upon integrating the vanishing divergence of the Poynting vector $\nabla \cdot (\mathbf{E} \times \mathbf{H}^* + \mathbf{E}^* \times \mathbf{H}) = 0$ for a modal solution (\mathbf{E}, \mathbf{H}) over a differential angular segment in the domain of polar coordinates, by means of Gauss' theorem

one relates the angular decay of modal power to the outflow of optical power in the radial direction. The limit of that flow for large radial coordinates exists and can be evaluated by again using the asymptotic form (2.5) of the mode profile, leading to expressions (2.12) for the modal power.

By considering the above expressions for large bend radii, one might wonder whether these may lead to a scheme for the normalization of nonguided modal solutions associated with straight waveguides e.g. as given in [90] in terms of plane wave superpositions. Examination of Eq. (2.12) with the help of Eq. (2.25), however shows that the expression (2.12) for the modal power is not applicable in the limit $R \rightarrow \infty$. Hence in this respect, there is no direct correspondence between the present bend modes supported by structures with low curvature and radiative modes of similar straight waveguides.

2.2.2 Orthogonality of bend modes

If the bend mode profiles are employed as basis elements for an expansion of a general optical field in the bend structure, the orthogonality properties of these modes become relevant: Projecting on the basis modes allows to relate the modal amplitudes to the given arbitrary field. As a consequence of the leaky nature of the complex bend modes, the orthogonality relations involve nonconjugate versions of the field profiles.³

Let $(\mathbf{E}_p, \mathbf{H}_p)$ and $(\mathbf{E}_q, \mathbf{H}_q)$ be the electromagnetic fields (2.1) of bend modes with propagation constants γ_p and γ_q , respectively, that are supported by the same bent waveguide. We start with the identity

$$\nabla \cdot (\mathbf{E}_p \times \mathbf{H}_q - \mathbf{E}_q \times \mathbf{H}_p) = 0, \quad (2.13)$$

which is a straightforward consequence of the Maxwell equations.

Consider the integral of Eq. (2.13) over an angular segment $\Omega = [0, \tilde{r}] \times [\theta, \theta + \Delta\theta]$ in the waveguide plane, specified by intervals of the polar coordinates:

$$\int_{\Omega} \nabla \cdot \mathbf{A} \, dS = 0, \quad \text{with} \quad \mathbf{A} = (A_r, A_y, A_\theta) = \mathbf{E}_p \times \mathbf{H}_q - \mathbf{E}_q \times \mathbf{H}_p. \quad (2.14)$$

After simplification of Eq. (2.14) by means of the Gauss theorem and a Taylor series expansion around θ , for small, nonzero $\Delta\theta$ one obtains

$$i(\gamma_p + \gamma_q)R \int_0^{\tilde{r}} A_\theta(r, \theta) \, dr = \tilde{r} A_r(\tilde{r}, \theta). \quad (2.15)$$

³An approximate orthogonality relation involving complex conjugates of one of the mode profiles is derived in Ref. [91], valid in the limit of large bend radius (i.e. for almost straight waveguides).

In order to evaluate the limit $\tilde{r} \rightarrow \infty$ of the right hand side, rA_r is expressed in terms of the basic mode profile components E_y and H_y , with the help of Eqs. (2.2, 2.3):

$$rA_r = \frac{i}{\mu_0\omega} r (E_{p,y}\partial_r E_{q,y} - E_{q,y}\partial_r E_{p,y}) + \frac{i}{\epsilon_0\epsilon_c\omega} r (H_{p,y}\partial_r H_{q,y} - H_{q,y}\partial_r H_{p,y}). \quad (2.16)$$

Here $\epsilon_c = n_c^2$ is the permittivity in the exterior region of the bend (constant for large radii). In this region, the basic components $\phi_p = \tilde{E}_{p,y}$ or $\phi_p = \tilde{H}_{p,y}$ of modal solutions (2.6) are given by Hankel functions of second kind i.e. $\phi_p(r) = A_{c,p} H_{\gamma_p R}^{(2)}(n_c k r)$, which, for large radial coordinate, assume the asymptotic forms

$$\begin{aligned} \phi_p(r) &\sim A_{c,p} \sqrt{\frac{2}{\pi n_c k r}} e^{-i(n_c k r - \gamma_p R \pi/2 - \pi/4)}, \\ \partial_r \phi_p(r) &\sim \left(-\frac{1}{2r} - i n_c k \right) \phi_p(r). \end{aligned} \quad (2.17)$$

By using these expressions, the limits $r \rightarrow \infty$ of the individual parts of Eq. (2.16) can be shown to vanish

$$\lim_{r \rightarrow \infty} [r(\phi_p \partial_r \phi_q - \phi_q \partial_r \phi_p)] = 0. \quad (2.18)$$

This leads to the identity

$$(\gamma_p + \gamma_q) \int_0^\infty \mathbf{a}_\theta \cdot (\mathbf{E}_p \times \mathbf{H}_q - \mathbf{E}_q \times \mathbf{H}_p) dr = 0, \quad (2.19)$$

where \mathbf{a}_θ is the unit vector in the azimuthal (θ -) direction.

After inspecting Eqs. (2.2), (2.3), one readily sees that the fields $(\mathbf{E}_{\tilde{p}}, \mathbf{H}_{\tilde{p}})$ and the propagation constant $\gamma_{\tilde{p}}$ with

$$\begin{aligned} \gamma_{\tilde{p}} &= -\gamma_p, \\ E_{\tilde{p},r} &= E_{p,r}, E_{\tilde{p},y} = E_{p,y}, E_{\tilde{p},\theta} = -E_{p,\theta}, \\ H_{\tilde{p},r} &= -H_{p,r}, H_{\tilde{p},y} = -H_{p,y}, H_{\tilde{p},\theta} = H_{p,\theta} \end{aligned} \quad (2.20)$$

describe a valid modal solution of the bend problem. By writing out the expression (2.19) for the quantities with indices \tilde{p} and q , by applying the transformation (2.20), and by observing that $\mathbf{a}_\theta \cdot (\mathbf{E}_{\tilde{p}} \times \mathbf{H}_q - \mathbf{E}_q \times \mathbf{H}_{\tilde{p}}) = \mathbf{a}_\theta \cdot (\mathbf{E}_p \times \mathbf{H}_q + \mathbf{E}_q \times \mathbf{H}_p)$, Eq. (2.19) can be given the form

$$(\gamma_p - \gamma_q) \int_0^\infty \mathbf{a}_\theta \cdot (\mathbf{E}_p \times \mathbf{H}_q + \mathbf{E}_q \times \mathbf{H}_p) dr = 0. \quad (2.21)$$

Motivated by the result (2.21), we define the following symmetric, complex valued product⁴ of two (integrable) electromagnetic fields $(\mathbf{E}_1, \mathbf{H}_1)$ and $(\mathbf{E}_2, \mathbf{H}_2)$, given in the polar coordinate system of the bend structure:

$$\begin{aligned} (\mathbf{E}_1, \mathbf{H}_1; \mathbf{E}_2, \mathbf{H}_2) &= \int_0^\infty \mathbf{a}_\theta \cdot (\mathbf{E}_1 \times \mathbf{H}_2 + \mathbf{E}_2 \times \mathbf{H}_1) dr \\ &= \int_0^\infty (E_{1,r}H_{2,y} - E_{1,y}H_{2,r} + E_{2,r}H_{1,y} - E_{2,y}H_{1,r}) dr. \end{aligned} \quad (2.22)$$

Obviously, the integrand vanishes if fields of different (2-D) polarizations are inserted, i.e. TE and TM bend modes are orthogonal with respect to (2.22). One easily checks that the product is also zero, if the forward and backward versions (two fields with their components related by the transformation (2.20)) of a bend mode are inserted. Finally, according to Eq. (2.21), two nondegenerate bend modes with propagation constants $\gamma_p \neq \gamma_q$ that are supported by the same bend structure are orthogonal with respect to the product (2.22). These formal statements hold for pairs of the fields (2.1) with the full space and time dependence, for the expressions excluding the time dependence, as well as for pairs of pure mode profiles that depend on the radial coordinate only.

Assuming that for a given bend configuration a discrete, indexed set of nondegenerate modal fields $(\mathbf{E}_p, \mathbf{H}_p)$ with (pairwise different) propagation constants γ_p is considered, the orthogonality properties can be stated in the more compact form

$$(\mathbf{E}_p, \mathbf{H}_p; \mathbf{E}_q, \mathbf{H}_q) = \delta_{p,q} N_p, \quad (2.23)$$

with

$$N_p = 2 \int_0^\infty \mathbf{a}_\theta \cdot (\mathbf{E}_p \times \mathbf{H}_p) dr = 2 \int_0^\infty (E_{p,r}H_{p,y} - E_{p,y}H_{p,r}) dr,$$

and $\delta_{p,q} = 0$ for $p \neq q$, $\delta_{p,p} = 1$. For mode sets of uniform polarization and uniform direction of propagation, it can be convenient to write the orthogonality properties in terms of the basic mode profile components $\phi = \tilde{E}_y$ (TE) or $\phi = \tilde{H}_y$ (TM). This leads to the relations

$$\int_0^\infty \zeta \frac{\phi_p \phi_q}{r} dr = \delta_{p,q} P_p, \quad \text{with } P_p = \int_0^\infty \zeta \frac{\phi_p^2}{r} dr, \quad (2.24)$$

$\zeta = 1$ for TE, and $\zeta = 1/\epsilon(r)$ for TM polarization, which differ from the corresponding familiar expressions for straight dielectric slab waveguides by the appearance of the inverse radial coordinate r only. According to Eq. (2.17), P_p is

⁴Cf. the standard variants of orthogonality relations for straight dielectric waveguides made of attenuating materials, as introduced e.g. in Ref. [43]

obviously bounded. Note, however, that here N_p and P_p are complex valued quantities.

An alternative derivation of Eq. (2.24) starts with the eigenvalue equation (2.4), written out for two different modal solutions. Each equation is multiplied by the other mode profile, one subtracts the results, and integrates over the radial axis. This leads to an equation with the difference of the squared propagation constants times the integral of Eq. (2.24) on one side, and with a limit as in Eq. (2.16) on the other. Then the reasoning of Eqs. (2.17, 2.18) can be applied to obtain the desired result. All sets of bend mode profiles shown in the following sections satisfy the relations (2.23) or (2.24), respectively, up to the accuracy that can be expected from the computational procedures.

2.3 Remarks on the numerical implementation

The solution of Eq. (2.7) requires the evaluation of Bessel and Hankel functions of complex order, where typically values of $\nu = \gamma R$ in intervals $\Re(\nu) \in [10^1, 10^4]$ and $\Im(\nu) \in [-10^{-1}, -10^{-12}]$ and arguments nkr up to 10^5 are encountered. The relevant Bessel functions are well behaved for the above values of order and argument; in particular, no terms with numerically harmful growth appear. We found that subroutines for complex order Bessel functions are not included in standard numerical libraries. MATLAB includes routines for these functions with complex argument with real order. MAPLE has built in procedures for complex argument and complex order, but they turn out to be prohibitively slow for large orders. Therefore we had to resort to own implementations.

The implemented procedures are based on “uniform asymptotic expansions” of Bessel functions and their derivatives in terms of Airy functions [73, 74]. More specifically, Eqs. (9.3.35), (9.3.36), (9.3.43), (9.3.44) from Ref. [73] were encoded, restricted to the first two terms of the summations, which we observed to be sufficient for the present examples. Hankel functions are computed as linear combination of Bessel functions. These expansions are not applicable in a regime where the order is close to the argument of the cylindrical functions. Fortunately we are interested here in configurations that involve complex orders (γR) with negative imaginary parts ($-\alpha$), and real arguments (nkr). While cases with approximate equality of order and argument could in principle occur for bend modes with extremely low loss (see e.g. bent waveguide configurations in Section 4.4.3.), by assigning a negligible small value to imaginary part of the argument, we circumvent any numerical

problems associated with this transition region. Otherwise, supplementary routines (see e.g. [74]) would have to be incorporated that cover that region of parameters.

Routines for Airy functions with complex arguments according to Ref. [92] were adopted. The procedures concerning the bent modes, as well as all parts of resonators model discussed in Chapters 3, 4, were encoded with C++ programming language. Since the Airy function routines were available in FORTRAN 77, this choice led to using FORTRAN 77 code within the C++ code. By comparison with the numerical values obtained with MAPLE, and also by validating the relations that held for the Wronskians of these functions (see Ref. [73], Eqs. (9.1.15), (9.1.16), (9.1.17)), the performance of the implemented routines for the desired range of orders and arguments is assessed.

Two techniques were implemented to find the roots ν of Eq. (2.7) in the complex plane. As a heuristic search procedure, a suitably selected region of the complex plane is divided into a number of rectangles, the lower left and upper right corner points of which are then supplied as initial guesses to a root finding routine based on the secant method. Repeated roots are rejected, the remaining unique roots are sorted in descending order of their imaginary part $-\alpha$. By refining the subdivision into rectangles, it can be ascertained with reasonable robustness that all the roots in the given region are captured.

Alternatively, a root tracking procedure can be implemented to solve the dispersion equation. Starting with the propagation constants of straight waveguides with a refractive index profile cross section equal to that of the given bent waveguide, a series of bends with decreasing radius are considered, with the roots found for each configuration used as initial guesses for the subsequent one. In this way, the bend propagation constants are followed in the complex plane.

2.4 Simulation results

As solutions of the eigenvalue problem (2.7), the bend mode solver yields complex propagation constants and mode profiles in terms of Eq. (2.6). Examples for different bend structures are discussed in this section.

Modes of different orders are indexed by counting the local minima in the absolute value of the principal electric (TE) or magnetic (TM) component of the mode profile.

2.4.1 Propagation constants

For purposes of validating our implementation we start with a comparison of phase propagation constants and attenuation levels. Tables 2.1 and 2.2 list values for angular mode numbers obtained with the present mode solver for two bend configurations adopted from Ref. [43], together with reference data from that source. We found an excellent overall agreement, for both the configurations with higher (Table 2.1) and lower refractive index contrast (Table 2.2).

R [μm]	$\nu = \gamma' R'$, Ref. [43]	$\nu = \gamma R$, present
50.5	$4.0189 \cdot 10^2 - i 7.9990 \cdot 10^{-2}$	$4.0189 \cdot 10^2 - i 7.9973 \cdot 10^{-2}$
100.5	$8.0278 \cdot 10^2 - (i 1.2856 \cdot 10^{-2})$	$8.0278 \cdot 10^2 - i 9.6032 \cdot 10^{-4}$
150.5	$1.2039 \cdot 10^3 - i 7.3948 \cdot 10^{-6}$	$1.2039 \cdot 10^3 - i 7.3914 \cdot 10^{-6}$
200.5	$1.6051 \cdot 10^3 - i 4.9106 \cdot 10^{-8}$	$1.6051 \cdot 10^3 - i 4.8976 \cdot 10^{-8}$

Table 2.1: TE_0 angular mode numbers ν for bent waveguides of different bend radius R according to Figure 2.1, with $(n_s, n_f, n_c) = (1.6, 1.7, 1.6)$, $d = 1 \mu\text{m}$, for a vacuum wavelength $\lambda = 1.3 \mu\text{m}$. Second column: Results from Ref. [43].

R [μm]	$\nu = \gamma' R'$, Ref. [43]	$\nu = \gamma R$, present
200.5	$3.1364 \cdot 10^3 - i 6.2059 \cdot 10^{-1}$	$3.1364 \cdot 10^3 - i 6.2135 \cdot 10^{-1}$
400.5	$6.2700 \cdot 10^3 - i 4.9106 \cdot 10^{-2}$	$6.2700 \cdot 10^3 - i 4.9159 \cdot 10^{-2}$
600.5	$9.4041 \cdot 10^3 - i 2.5635 \cdot 10^{-3}$	$9.4041 \cdot 10^3 - i 2.5636 \cdot 10^{-3}$
800.5	$1.2538 \cdot 10^4 - i 1.1174 \cdot 10^{-4}$	$1.2538 \cdot 10^4 - i 1.1177 \cdot 10^{-4}$
1000.5	$1.5673 \cdot 10^4 - i 4.4804 \cdot 10^{-6}$	$1.5673 \cdot 10^4 - i 7.1806 \cdot 10^{-5}$

Table 2.2: TE_0 angular mode numbers ν for low contrast bends according to Figure 2.1, with different bend radius R and parameters $(n_s, n_f, n_c) = (3.22, 3.26106, 3.22)$, $d = 1 \mu\text{m}$, for a vacuum wavelength $\lambda = 1.3 \mu\text{m}$. Second column: Results from Ref. [43].

The discussion of bent waveguides in Ref. [43] applies an alternative definition of the bend radius R' as the distance from the origin to the center of the core layer, which is related to the radius R as introduced in Figure 2.1 by $R' = R - d/2$ (hence the unusual values of bend radii in Tables 2.1, 2.2). Both definitions are meant as descriptions of the same physical configuration, i.e. both lead to the same angular field dependence (2.1), given in terms of the azimuthal mode numbers ν as determined by the dispersion equation (2.7). Via the relation $\nu = \gamma R = \gamma' R'$, the different choices of the bend radius result in different values γ and $\gamma' = \gamma R / (R -$

$d/2$) for the propagation constant, and consequently in different values β , β' and α , α' for the phase and attenuation constants.

Still, for many applications one is interested in the variation of the phase constant and the attenuation with the curvature of the bend, expressed by the bend radius. Figure 2.2 shows corresponding plots for the configuration of Table 2.1, including values for the two different bend radius definitions. While on the scale of the figure the differences are not visible for the attenuation constants, the levels of the phase propagation constants differ indeed substantially for smaller bend radii. As expected, for low curvature the values of both β/k and β'/k tend to the effective indices of straight slab waveguides with equivalent refractive index profile. For the present low contrast configuration, only minor differences between TE and TM polarization occur.

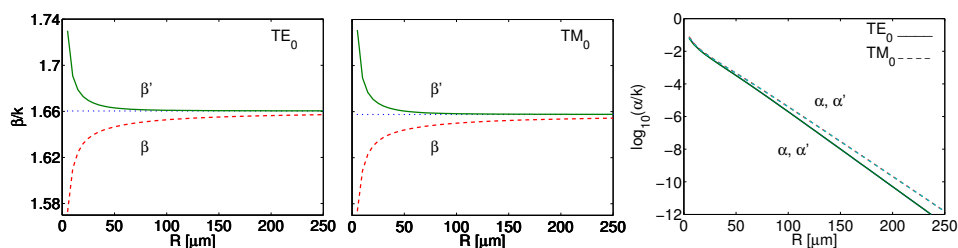


Figure 2.2: Phase constants β , β' and attenuation constants α , α' versus the bend radius R , for bends according to Table 2.1. The dashed quantities $\beta' = \beta R/R'$ and $\alpha' = \alpha R/R'$ correspond to a description of the bend in terms of an alternative bend radius $R' = R - d/2$. The dotted lines in the first two plots indicate the levels of the effective indices of a straight waveguide with the cross section and refractive index profile of the bent slabs.

Certainly no physical reasoning should rely on the entirely arbitrary definition of the bend radius. This concerns e.g. statements about the growth or decay of phase propagation constants with R (according to Figure 2.2 the sign of the slope can indeed differ), or discussions about the “phase matching” of bent waveguides and straight channels in coupler or microresonator configurations. Care must be taken that values for β and α or effective quantities like β/k are used with the proper definition of R taken into account.

With the present (semi) analytic solutions at hand, we have now a possibility to validate “classical” expressions for the variation of the bend attenuation with the bend radius. Beyond the high curvature region, Figure 2.2 shows a strict exponential decay of α with respect to R , as predicted by an approximate loss formula for

symmetric bent slabs given in [93, Eq. 9.6-24]:

$$\alpha = \frac{R-w}{R} \frac{g^2}{2\beta_s(1+gw)} \frac{h^2}{(n_f^2 - n_s^2)k^2} e^{2gw} e^{-2(\beta_s \tanh^{-1}(g/\beta_s) - g)(R-w)}. \quad (2.25)$$

Here β_s is the propagation constant corresponding to the straight waveguide with the width $d = 2w$ and refractive index profile (n_s, n_f, n_s) of the bent waveguide under investigation. Derived quantities are $g^2 = \beta_s^2 - n_s^2 k^2$ and $h^2 = (n_f^2 - n_s^2)k^2 - g^2$. Figure 2.3 reveals a very good agreement with the attenuation constants calculated by our procedures for bends with low curvature.

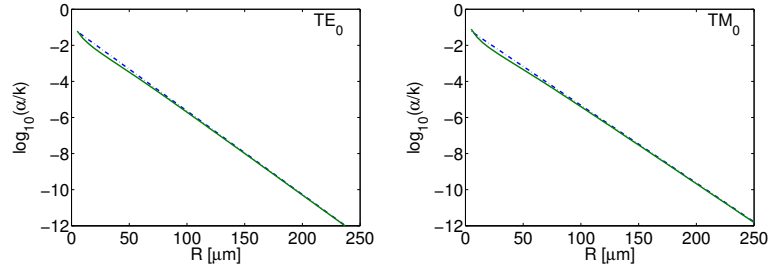


Figure 2.3: Attenuation constants of the principal *TE* and *TM* modes for symmetric bent waveguides with $n_f = 1.7$, $n_s = n_c = 1.6$, $d = 1 \mu\text{m}$, $\lambda = 1.3 \mu\text{m}$, for varying bend radius R . The dashed lines show the exponential decay according to Eq. (2.25); the solid curves are the present analytic mode solver results.

2.4.2 Mode profiles

Beyond the values of the propagation constants, the present analytical mode solver permits to evaluate modal fields for the full range of radial coordinates. Figure 2.4 illustrates normalized profiles for a few fundamental *TE* bend modes of the configurations considered in Table 2.1.

One observes the expected effects [93, 43]: Bends with large radii R support modes with almost the familiar symmetric, well confined plane profiles of straight symmetric slab waveguides. With decreasing bend radius, the phase profiles of the bend modes become more and more curved. Along with the increasing attenuation, the maximum in the absolute value of the basic electric field shifts towards the outer rim of the bend, and the relative field levels in the exterior region grow. The mode profiles are essentially complex, with oscillatory behaviour of the real- and imaginary parts of the field profiles in the exterior region. The effects of “bending” and the lossy nature of the bend modes are illustrated best by the snapshots of the physical fields in the second row of Figure 2.4.

2.4 Simulation results

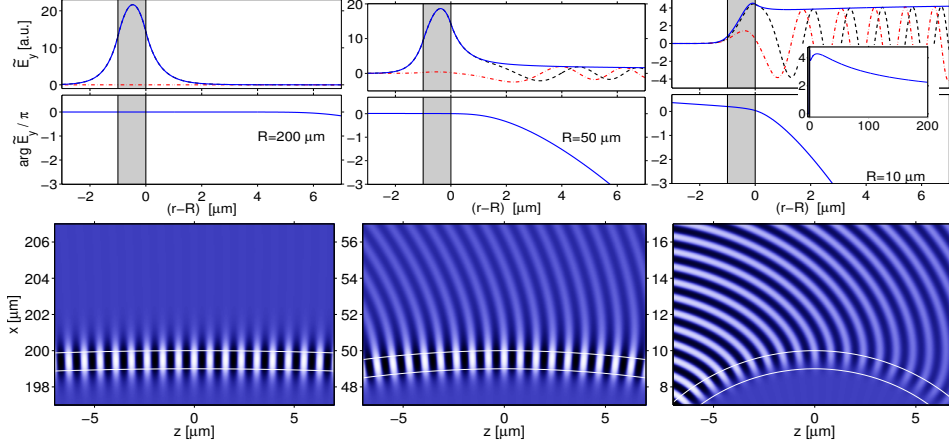


Figure 2.4: TE_0 mode profiles for bends according to the setting of Table 2.1, with different bend radii $R = 200, 50, 10 \mu\text{m}$. First row: radial dependence of the absolute value (solid line), the real- and imaginary part (dashed and dash-dotted lines), and the phase of the basic electric field component \tilde{E}_y . The profiles are normalized according to Eq. (2.12), with the global phase adjusted such that $\tilde{E}_y(R)$ is real and positive. Second row: snapshots of the propagating bend modes according to Eq. (2.1). The gray scales correspond to the levels of the real, physical field E_y .

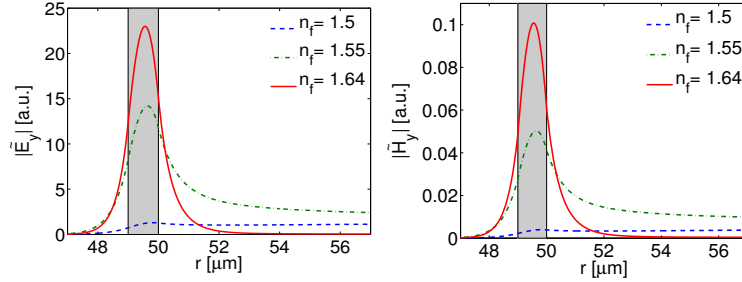


Figure 2.5: Fundamental TE (left) and TM mode profiles (right) for symmetric bent slabs with $R = 50 \mu\text{m}$, $\lambda = 1.55 \mu\text{m}$, $d = 1 \mu\text{m}$, $n_s = n_c = 1.45$, and different core refractive indices. As n_f is changed from 1.5 to 1.55 to 1.64, the effective propagation constants γ/k change from $1.4580 - i 9.2077 \cdot 10^{-3}$ to $1.4893 - i 1.1624 \cdot 10^{-3}$ to $1.5598 - i 2.1364 \cdot 10^{-7}$ (TE_0), and from $1.4573 - i 1.0088 \cdot 10^{-2}$ to $1.4862 - i 1.6013 \cdot 10^{-3}$ to $1.5504 - i 9.4104 \cdot 10^{-7}$ (TM_0), respectively.

Just as for straight waveguides, the confinement of the bend modes depends critically upon the refractive index contrast. As exemplified by Figure 2.5, one observes quite similar effects when the core refractive index of the bend is varied, as found

for the change in bend radius: With loosened confinement and growing attenuation for decreasing n_f , the mode profile maximum shifts towards the outer rim, and the relative field levels in the exterior region increase. Note that all (normalizable) mode profiles decay for large radial coordinates according to Eqs. (2.6) and (2.17), despite their appearance in Figs. 2.4 and 2.5 (See the insets in Figs. 2.4, 2.7, 2.9).

2.4.3 Comparison with FDTD results

As an attempt for a further validation of our results on bend modes we have considered the following numerical experiment. Embedded in a common background, the core of a straight slab waveguide is placed in the vicinity of a ring shaped core of the same width. If a guided wave is launched into the straight channel, by evanescent coupling it excites optical waves that travel around the ring. If, for given polarization, the bent ring waveguide supports only a single low-loss bend mode, one can expect that a field with the corresponding profile establishes itself after a suitable propagation distance. The experiment is carried out in the time domain, with a ramped-up, subsequently time-harmonic excitation, that is advanced over a limited time interval, such that resonance effects can be excluded. Allowing the “wave front” to propagate once around the ring, a radial field cross section e.g. at an angular position of 90° after the in-coupling region can be expected to give an approximation to the bend mode profile. By observing the exponential decay of the “stationary” field for an angular segment after that region, one can estimate the attenuation of the bend mode.

We have applied a standard Finite Difference Time Domain (FDTD) scheme [94, 95], where a computational window of $80 \times 58 \mu\text{m}^2$ is discretized uniformly by a mesh with step sizes of $0.05 \mu\text{m}$. Perfectly matched layer (PML) boundary conditions enclose the computational domain, with a width of 8 points, a quadratic envelope, and a strength such that the theoretical reflectivity of a wave propagating through the background material at normal incidence is 10^{-6} . The interior of the computational window contains the ring with parameters as given for Figure 2.6 and the straight waveguide with the same refractive index profile, with a gap of $0.5 \mu\text{m}$ in between. A modal field is launched into the straight core using the total field /scattered field approach [55]. Its amplitude is raised according to a half-Gaussian curve with a waist of 5 fs, with the maximum being reached at 40 fs. After this time, the incident field amplitude is kept constant. The simulation runs for a time of 1.1 ps with a time step of 0.1 fs, after which the ramp of the wave has gone around the ring approximately once.

Figure 2.6 shows an excellent agreement of the approximation for the bend mode

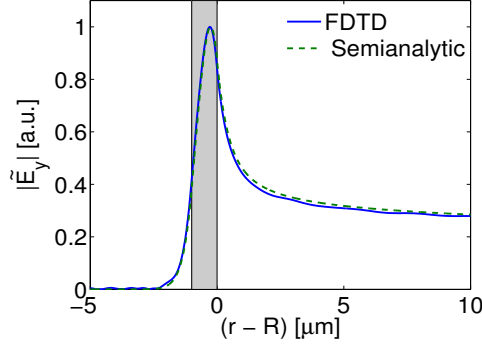


Figure 2.6: Bend mode profiles as determined by a FDTD simulation (continuous line) and by the analytical model (dashed curve), for a configuration with $(n_s, n_f, n_c) = (1.6, 1.7, 1.6)$, $d = 1 \mu\text{m}$, $R = 25 \mu\text{m}$, $\lambda = 1.3 \mu\text{m}$. Here the mode profiles are normalized to a unit maximum.

profile obtained in this way with the result of the analytical bend mode solver. We also found a very good agreement of the attenuation constant $\alpha = 0.01949 \mu\text{m}^{-1}$ estimated by the FDTD simulation with the analytic result $\alpha = 0.01978 \mu\text{m}^{-1}$. Hence comparisons of this kind can confirm the expectation that the bend modes as introduced in Eq. (2.1) are indeed suitable basis fields for a (2-D) description of cylindrical microresonator configurations.

2.4.4 Higher order bend modes

For cylindrical cavities with relatively high radial refractive index contrast, also higher order bend modes can be relevant for an adequate representation of resonant field patterns [96, 97, 98]. Table 2.3 summarizes results for propagation constants of fundamental and first order modes of both polarizations for a nonsymmetric slab with decreasing bend radius. In a straight configuration, the refractive index profile supports two guided modes per polarization orientation.

Just as for the fundamental fields, the attenuation of the first order modes grows with decreasing bend radius. Figure 2.7 shows that the significantly higher loss levels of the first order modes are accompanied by larger field amplitudes in the exterior region and by a wider radial extent of the mode profiles.

Figure 2.8 illustrates the spatial evolution of the TE_0 and TE_1 modes for a small configuration with $R = 20 \mu\text{m}$. Major differences between the plots for the single fundamental and first order fields are the faster decay of the TE_1 mode and the minimum in the radial distribution of that field.

R [μm]	TE_0		TE_1	
	β/k	α/k	β/k	α/k
∞	1.6775	—	1.6164	—
150	1.6663	≈ 0	1.6037	$1.2117 \cdot 10^{-7}$
100	1.6611	$1.0984 \cdot 10^{-12}$	1.5979	$1.7606 \cdot 10^{-5}$
50	1.6473	$9.6704 \cdot 10^{-7}$	1.5818	$1.5113 \cdot 10^{-3}$
20	1.6185	$1.8299 \cdot 10^{-3}$	1.5283	$1.4205 \cdot 10^{-2}$
10	1.5890	$1.6025 \cdot 10^{-2}$	1.4381	$3.4287 \cdot 10^{-2}$

R [μm]	TM_0		TM_1	
	β/k	α/k	β/k	α/k
∞	1.6758	—	1.6134	—
150	1.6645	≈ 0	1.6004	$3.5259 \cdot 10^{-7}$
100	1.6593	$1.8446 \cdot 10^{-12}$	1.5946	$3.4692 \cdot 10^{-5}$
50	1.6451	$1.2668 \cdot 10^{-6}$	1.5791	$2.0368 \cdot 10^{-3}$
20	1.6156	$2.1391 \cdot 10^{-3}$	1.5273	$1.7868 \cdot 10^{-2}$
10	1.5855	$1.8702 \cdot 10^{-2}$	1.4391	$4.6089 \cdot 10^{-2}$

Table 2.3: Propagation constants $\gamma = \beta - i\alpha$ of fundamental and first order modes for bends with $(n_s, n_f, n_c) = (1.6, 1.7, 1.55)$, $d = 2 \mu\text{m}$, $\lambda = 1.55 \mu\text{m}$, for different bend radii R . The value $R = \infty$ indicates the corresponding (bimodal) straight waveguide.

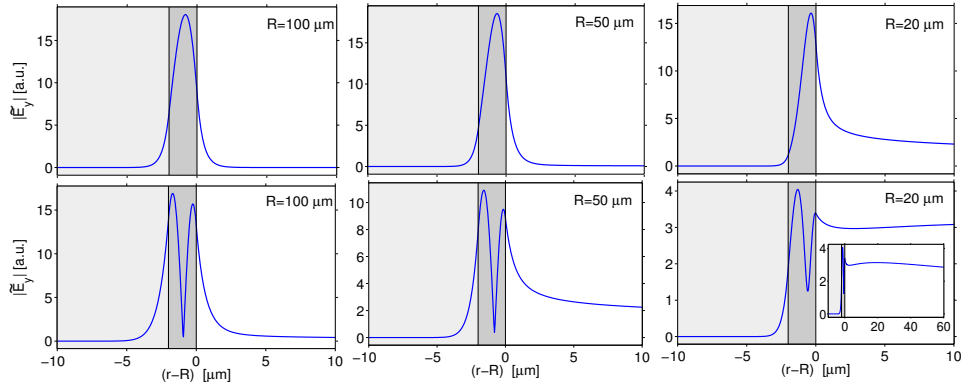


Figure 2.7: Fundamental and first order TE modes for the bends of Table 2.3, absolute values of the basic profile component \tilde{E}_y of structures with radii $R = 100$, 50, and 20 μm .

The last column of Figure 2.8 gives an example for an interference pattern that is generated by a superposition of both modes. Normalized profiles with unit am-

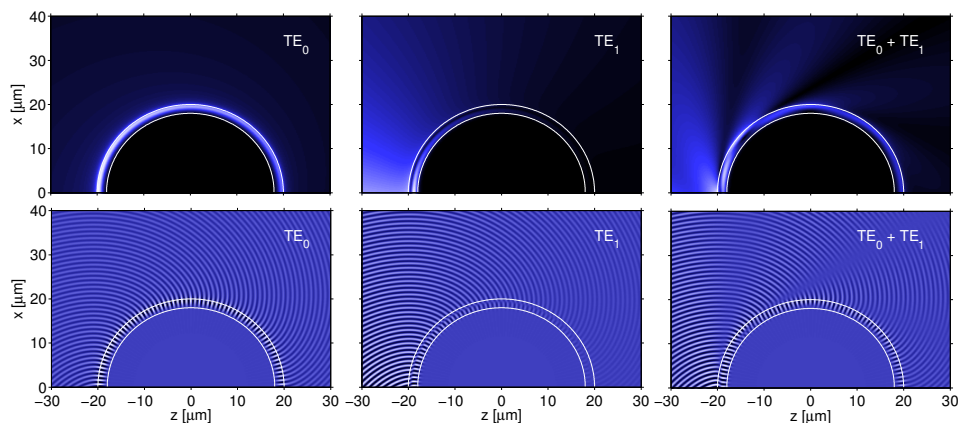


Figure 2.8: *Spatial evolution and interference of the fundamental and first order TE modes, for a configuration of Table 2.3 with $R = 20 \mu\text{m}$. The propagation of the TE_0 mode (left), of the TE_1 mode (center), and of a superposition of these (right) is evaluated. The plots show the absolute value $|E_y|$ (top) and snapshots of the time harmonic physical field E_y (bottom).*

plitudes and real, positive $\tilde{E}_y(R)$ are initialized at $\theta = 0$, or $z = 0$, respectively (cf. Figure 2.1). In the core region one observes the familiar beating process, here in the angular direction, with intensity maxima shifting periodically between the center and the outer rim of the ring. In the exterior region, the mode interference results in a ray-like pattern, where rapidly diverging bundles of waves propagate in directions tangential to the ring, originating from regions around the intensity maxima at the outer ring interface. These phenomena are obscured by the fast decay of the first order mode.

Apart from the fundamental and first order fields, further higher order modes can be found for the bent slabs of Table 2.3. While the TE_0 and TE_1 modes considered so far can be viewed as being related to the guided modes supported by a straight slab with the same refractive index profile and thickness, the profiles shown in Figure 2.9 are not related to guided modes of that straight waveguide.

For these modes, the classification by the number of minima in the absolute value of the mode profile can still be applied; also the systematics of larger attenuation and higher exterior field levels for growing mode order remains valid.

In contrast to the two lowest order fields, these higher order modes exhibit pronounced intensity maxima in the interior region. Apparently, for the present non-symmetric bend, this indicates the transition to the regime of whispering gallery modes, which is discussed below.

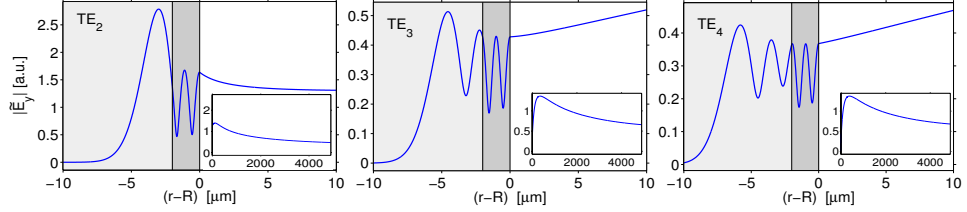


Figure 2.9: Higher order TE modes for a bend as considered for Table 2.3 with $R = 100 \mu\text{m}$. The corresponding propagation constants γ/k are $1.5347 - i 2.8974 \cdot 10^{-3}$ (TE_2), $1.5094 - i 5.7969 \cdot 10^{-3}$ (TE_3), and $1.4891 - i 6.1955 \cdot 10^{-3}$ (TE_4), respectively. The insets clearly show the decay of the mode profiles for $r \rightarrow \infty$ after an initial growth of the field in the cover region.

2.4.5 Whispering gallery modes

If the core width of a bent waveguide is increased, then as in the case of straight waveguides, the mode profile changes, and eventually the bent waveguide becomes multimodal. But at the same time another interesting phenomenon occurs, which can not happen with straight waveguides. If the core width of a bent waveguide is increased beyond a certain limit, a regime is reached where the bend modes are guided by just the outer dielectric interface and the precise location of the inner dielectric interface becomes irrelevant. These modes are known as “whispering gallery modes” (WGMs).

The model of Section 2.2 covers those configurations with the formal choice $n_s = n_f$ in Figure 2.1, where d becomes irrelevant. The above mentioned transition of a bend mode towards a WGM is shown in Figure 2.10. For illustration purposes, we adopt a set of parameters from Ref. [57], that specifies a high-contrast curved interface with a rather small radius, i.e. a parameter regime that differs considerably from the previous bent slabs. For the present configuration, the field profiles of the TE_0 mode for $d = 1.5 \mu\text{m}$, $2.0 \mu\text{m}$, and $4 \mu\text{m}$ are almost identical.

In fact, plots of the propagation constants for these modes in Figure 2.11 show that for core widths larger than $1.0 \mu\text{m}$, n_{eff} becomes almost independent from the core width. For increasing core width, a larger part of the mode profile is trapped inside the core. This results in the increase of the phase constant β and the decrease of the attenuation constant α .

A comparison of the present analytical simulation results for the propagation constants of the four lowest order WGMs with FDTD results from Ref. [57] is shown in Table 2.4. Again we find a very good agreement.

2.4 Simulation results

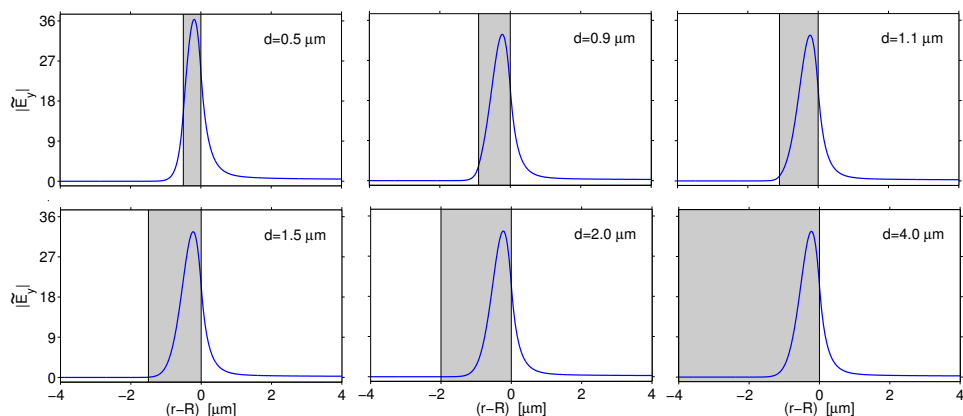


Figure 2.10: *Transition of a bend mode towards a whispering gallery mode. The core width d of a bent waveguide with the parameters $n_f = 1.5$, $n_c = 1.0$, $R = 4.0 \mu\text{m}$, and $\lambda = 1.0 \mu\text{m}$ is increased, until the whispering gallery mode regime is reached.*

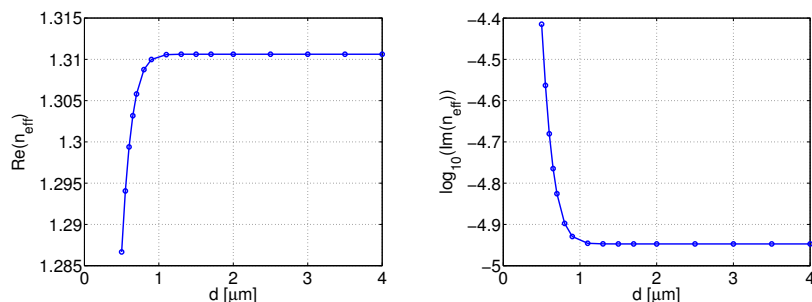


Figure 2.11: *Effect of increasing the core width on the TE_0 bent mode propagation constant (given in terms of effective refractive index $n_{\text{eff}} = \gamma/k$). The waveguide configuration is as for Figure 2.10.*

As shown in Figure 2.12, for growing mode order, qualitatively one finds the increase of the attenuation, the outwards shift of the outermost profile intensity maxima, the raise of the exterior field levels, and the wider radial extent of the profiles, just as for the modes of the bent cores in Figs. 2.7 and 2.9. In contrast to the impression given e.g. in Refs. [96, 98], the complex mode profiles exhibit minima in the absolute value of the principal field component, not nodal points.

Despite the substantial differences in the attenuation levels of these modes, the higher order fields may well play a role for the representation of resonances of the

	γ/k , present	γ/k , Ref. [57]
TE ₀	$1.3106 - i 1.1294 \cdot 10^{-5}$	$1.310 - i 1.133 \cdot 10^{-5}$
TE ₁	$1.1348 - i 1.8862 \cdot 10^{-3}$	$1.134 - i 1.888 \cdot 10^{-3}$
TE ₂	$0.9902 - i 1.1676 \cdot 10^{-2}$	—
TE ₃	$0.8558 - i 1.8832 \cdot 10^{-2}$	—

Table 2.4: Propagation constants γ for the whispering gallery modes of a curved dielectric interface with the parameters $n_f = 1.5$, $n_c = 1.0$, $R = 4.0 \mu\text{m}$, and $\lambda = 1.0 \mu\text{m}$. Third column: Results from Ref. [57].

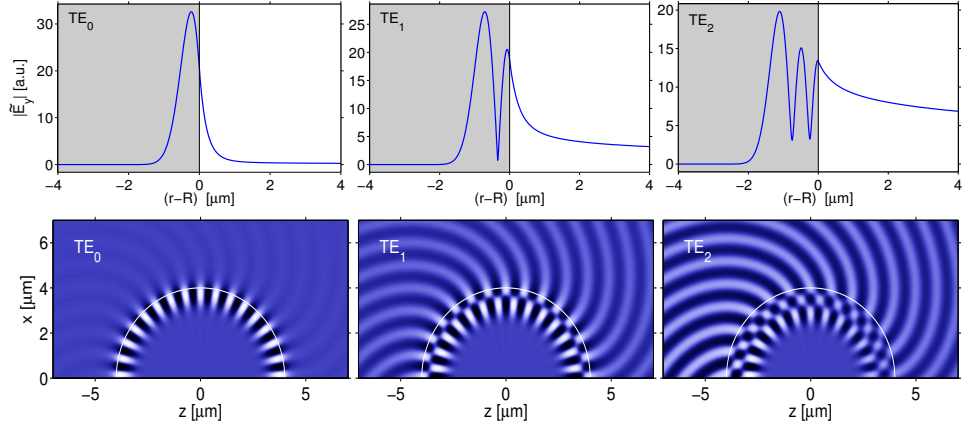


Figure 2.12: Profiles (top) and physical field evolution (bottom) of the three lowest order whispering gallery modes according to the specification of Table 2.4.

corresponding disc-shaped microresonator cavity, due to the rather short circumference. Therefore we conclude this section with two examples of interferences of whispering gallery modes in Figure 2.13. As for the bend slabs in Figure 2.8 one observes an interior beating pattern and ray-like bundles of waves in the exterior, here on much shorter ranges in terms of the local wavelength.

2.5 Effect of core refractive index perturbation

As motivated in Section 1.4.5, we are interested in the tuning of resonators by changes of the cavity core refractive index. In order to estimate this effect, one must know the dependence of the propagation constants on the core refractive index. Here we derive a perturbational expression for the change in the cavity propagation constants due to changes in the core refractive index.

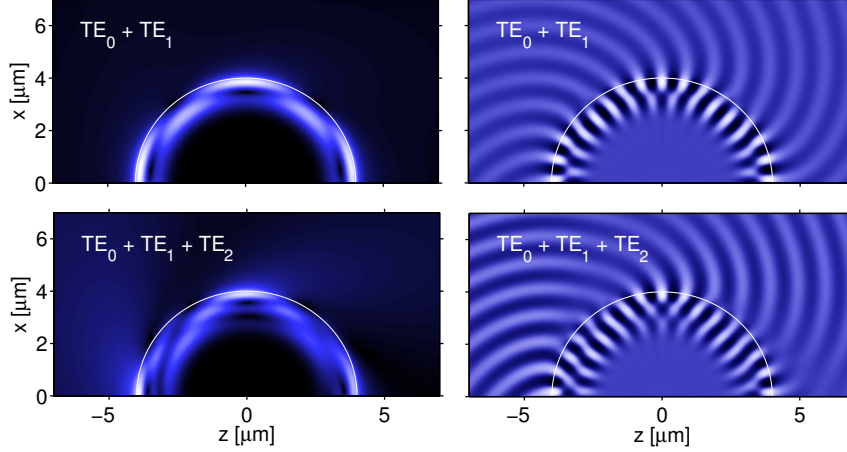


Figure 2.13: *Interference patterns of the modes of Figure 2.12 and Table 2.4; the plots show the absolute value $|E_y|$ (left) and snapshots of the time harmonic physical field E_y (right). Superpositions of the two (top) and three (bottom) lowest order fields are considered, initialized with unit amplitudes of the normalized profiles (with positive $\tilde{E}_y(R)$) at $z = 0$.*

Derivation of perturbational expression

For a bent waveguide with the refractive index distribution $n(r) = \sqrt{\epsilon(r)}$, let (\mathbf{E}, \mathbf{H}) be the full electric and magnetic field (2.1) for a given mode. Suppose that the core refractive index is slightly perturbed, and the perturbed refractive index distribution is given by $n_p(r) = \sqrt{\epsilon_p(r)}$. For this perturbation, assuming that the mode profile remains unchanged, the corresponding perturbed mode $(\mathbf{E}_p, \mathbf{H}_p)$ is approximated as

$$\begin{pmatrix} \mathbf{E}_p \\ \mathbf{H}_p \end{pmatrix} = P(\theta) \begin{pmatrix} \mathbf{E} \\ \mathbf{H} \end{pmatrix}, \quad (2.26)$$

where $P(\theta)$ is an unknown function of the angular coordinate θ .

By using Lorentz's reciprocity theorem [43] in polar coordinates to $(\mathbf{E}_p, \mathbf{H}_p, \epsilon_p)$ and $(\mathbf{E}, \mathbf{H}, \epsilon)$, one obtains

$$\int_0^\infty \nabla \cdot (\mathbf{E}_p \times \mathbf{H}^* + \mathbf{E}^* \times \mathbf{H}_p) r dr = -i\omega\epsilon_0 \int_0^\infty (\epsilon_p - \epsilon) \mathbf{E}_p \cdot \mathbf{E}^* r dr,$$

which upon inserting the ansatz given by Eq. (2.26) and after simplifying reduces to

$$\frac{dP}{d\theta} \int_0^\infty \mathbf{a}_\theta \cdot (\mathbf{E} \times \mathbf{H}^* + \mathbf{E}^* \times \mathbf{H}) dr = -i\omega\epsilon_0 P \int_0^\infty (\epsilon_p - \epsilon) \mathbf{E} \cdot \mathbf{E}^* r dr, \quad (2.27)$$

where \mathbf{a}_θ is the unit vector in the angular direction.

Inserting the bent waveguide field ansatz given by Eq. (2.1) and solving for $P(\theta)$ leads to

$$P(\theta) = P_0 \exp \left(-i\omega\epsilon_0 \frac{\int_0^\infty (\epsilon_p - \epsilon) \tilde{\mathbf{E}} \cdot \tilde{\mathbf{E}}^* r \, dr}{\int_0^\infty \mathbf{a}_\theta \cdot (\tilde{\mathbf{E}} \times \tilde{\mathbf{H}}^* + \tilde{\mathbf{E}}^* \times \tilde{\mathbf{H}}) \, dr} \theta \right), \quad (2.28)$$

where P_0 is a constant, the superscript \sim represents the mode profile associated with the field. Thus the perturbed modal field is

$$\begin{pmatrix} \mathbf{E}_p \\ \mathbf{H}_p \end{pmatrix} = P_0 \begin{pmatrix} \tilde{\mathbf{E}} \\ \tilde{\mathbf{H}} \end{pmatrix} \exp \left(-i \left(\gamma + \frac{\omega\epsilon_0}{R} \frac{\int_0^\infty (\epsilon_p - \epsilon) \tilde{\mathbf{E}} \cdot \tilde{\mathbf{E}}^* r \, dr}{\int_0^\infty \mathbf{a}_\theta \cdot (\tilde{\mathbf{E}} \times \tilde{\mathbf{H}}^* + \tilde{\mathbf{E}}^* \times \tilde{\mathbf{H}}) \, dr} \right) R\theta \right),$$

and the change in propagation constant $\delta\gamma$ due to the perturbation is given by

$$\delta\gamma = \frac{\omega\epsilon_0}{R} \frac{\int_0^\infty (\epsilon_p - \epsilon) \tilde{\mathbf{E}} \cdot \tilde{\mathbf{E}}^* r \, dr}{\int_0^\infty \mathbf{a}_\theta \cdot (\tilde{\mathbf{E}} \times \tilde{\mathbf{H}}^* + \tilde{\mathbf{E}}^* \times \tilde{\mathbf{H}}) \, dr}. \quad (2.29)$$

Note that above expression can also be written in terms of modal fields (\mathbf{E}, \mathbf{H}) instead of mode profiles $(\tilde{\mathbf{E}}, \tilde{\mathbf{H}})$. The right hand side of Eq. (2.29) is a pure real number. Therefore this expression, in fact, gives the change in the real part of the propagation constant only. In Ref. [43] a similar expression for the change in propagation constant for bulk uniform permittivity perturbations of straight waveguides is derived by means of a variational principle.

The use of asymptotic expansion of $H_\nu^{(2)}(nkr)$, given by Eq. (2.5), reveals that, in the present case of bent waveguides, the integral $\int_0^\infty (\epsilon_p - \epsilon) \tilde{\mathbf{E}} \cdot \tilde{\mathbf{E}}^* r \, dr$ is undefined for the upper limit $r = \infty$, if $\epsilon_p - \epsilon$ does not vanish for large radial coordinates. Still for a uniform perturbation $\delta\epsilon_f = \delta n_f^2 = n_{f,p}^2 - n_f^2$ of the core refractive index, it is well defined; in that case Eq. (2.29) simplifies to

$$\delta\beta = \frac{\omega\epsilon_0}{R} \frac{\delta n_f^2 \int_{R-d}^R \mathbf{E} \cdot \mathbf{E}^* r \, dr}{\int_0^\infty \mathbf{a}_\theta \cdot (\mathbf{E} \times \mathbf{H}^* + \mathbf{E}^* \times \mathbf{H}) \, dr} \quad (2.30)$$

where $R-d$ and R define the core interface as shown in Figure 2.1, $n_{f,p}$ and n_f are perturbed and unperturbed core refractive index respectively. For a small uniform perturbation of the core refractive index, using Eq. (2.30), one can approximately write

$$\frac{\partial\beta}{\partial n_f} = 2n_f \frac{\partial\beta}{\partial\epsilon_f} \approx 2n_f \frac{\omega\epsilon_0}{R} \frac{\int_{R-d}^R \mathbf{E} \cdot \mathbf{E}^* r \, dr}{\int_0^\infty \mathbf{a}_\theta \cdot (\mathbf{E} \times \mathbf{H}^* + \mathbf{E}^* \times \mathbf{H}) \, dr}. \quad (2.31)$$

Note that the integrals that occur in the above expression are well behaved.

Simulation results

Now we assess the validity of the perturbation expression (2.31). For the moderately lossy bent waveguide configuration considered in Figure 2.14, the estimation of the change in the phase propagation constants by the perturbation expression agrees very well with the directly computed values.

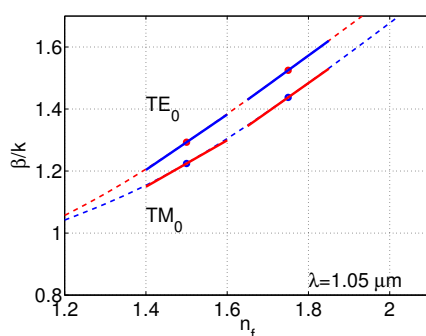


Figure 2.14: Phase propagation constants estimated by the perturbational expression, for a bent waveguide configuration with $n_s = n_c = 1.0$, $d = 0.5 \mu\text{m}$, $R = 5 \mu\text{m}$. Dashed lines denote β/k obtained by direct calculations, dots are reference points $n_f = 1.5$ and $n_f = 1.75$, and the slope of the solid line segments is given by expression (2.31).

As an another example, for Figure 2.15, the perturbational expression (2.31) is assessed for the WGMs. For the moderately lossy fundamental and first order WGMs, the agreement is excellent, but for the second order WGMs with considerable losses (e.g. $n_f = 1.5$, $\gamma/k = 1.0422 - i 5.7410 \cdot 10^{-3}$ (TE₂), $1.0339 - i 1.21610 \cdot 10^{-2}$ (TM₂)) there are major deviations. Apparently, here the changes in the mode profiles and the attenuation constants due to the core refractive index perturbation are not negligible, such that the ansatz (2.26) is not appropriate for these fields.

2.6 Concluding remarks

In this chapter we have reconsidered a classical rigorous analytic model for 2-D optical bent slab waveguides and curved dielectric interfaces with piecewise constant refractive index profiles. A frequency domain ansatz in terms of complex order Bessel and Hankel functions leads to an eigenvalue equation (transverse resonance condition) that is to be solved for the complex valued angular mode number.

According to the asymptotic expansions of the relevant Hankel functions, it is

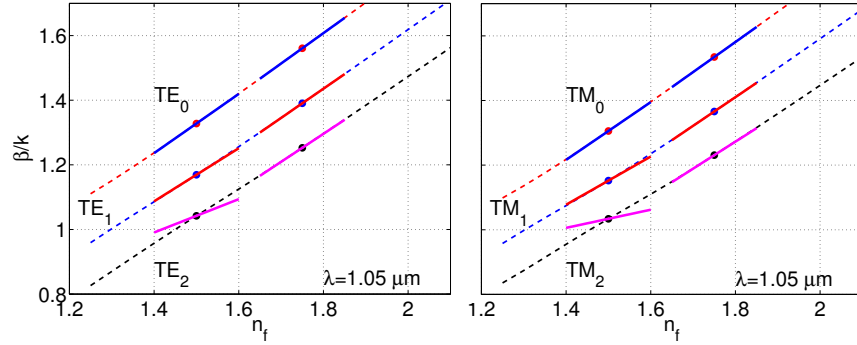


Figure 2.15: Phase propagation constants of WGMs evaluated by the perturbational expression (2.31), for a bent waveguide configuration with $n_c = 1.0$, $d = R = 5 \mu\text{m}$. Interpretation of the curves is as for Figure 2.14.

shown that the modal solutions decay according to $1/\sqrt{r}$ for growing radial coordinates r , i.e. specific products of the profile components are integrable along the radial axis. For purposes of bend mode normalization, we could derive quite compact expressions for the angular modal power. A complex valued product of two general fields in the polar coordinate system has been defined, which is suitable to express orthogonality properties of nondegenerate, directional, and polarized modal solutions of the bent waveguide problem. Perturbational analysis for the effect of core refractive index changes is presented.

A series of detailed (benchmarking) examples complements the former abstract reasoning. Concerning propagation constants, these emphasize the arbitrariness in the definition of the bend radius. Examples for profiles of bend modes and for the spatial evolution of the related physical fields are given, for fundamental and higher order modes of bent slabs with relatively small refractive index contrast, as well as for whispering gallery modes supported by high-contrast curved interfaces. A few illustrative examples for interferences of bend modes have been shown, that exhibit a periodic angular beating pattern (apart from the mode decay) in the guiding regions of the bends, and tangential, ray-like bundles of outgoing waves in the exterior regions. The validity of the perturbational expression for shifts in the (real part of) propagation constants of moderately lossy modes is also verified.

With the present results, a sound analytical basis for (2-D) coupled-mode-theory modeling of resonator devices involving microrings or microdisks as cavities has been established. We expect that many of the notions discussed in this chapter are directly transferable to the case of 3-D configurations involving bent channels with 2-D cross sections.

Chapter 3

Bent-Straight waveguide couplers

Bent-straight waveguide couplers are one of the ingredients of the “standard model” of circular microresonators. Capitalizing on the availability of rigorous analytical modal solutions for 2-D bent waveguides, in this chapter these couplers are modeled using a frequency domain spatial coupled mode formalism, derived by means of a variational principle. Simulation results for the response of 2-D couplers for varying separation distances, radii, and different wavelengths are discussed. The resulting scattering matrices show reciprocity properties as expected according to the symmetry of the coupler structures.

Parts of this chapter are adapted from:

K. R. Hiremath, R. Stoffer, M. Hammer. *Modeling of circular integrated optical microresonators by 2-D frequency domain coupled mode theory*. Optics Communications. (accepted).

Analysis of circular microresonators by means of the functional decomposition elaborated in Section 1.4 involves bent-straight waveguide couplers. The response of these couplers is characterized by scattering matrices, which in turn determine the spectral response of the resonators. Therefore it is essential to have a parameter free model of bent-straight waveguide couplers.

In this chapter, we analyze the interaction between bent waveguides and straight waveguides in two dimensional settings, using spatial coupled mode theory. The formulation presented in Section 3.2 takes into account that multiple modes in each of the cores may turn out to be relevant for the functioning of the resonators. Section 3.3 discusses reciprocity of the scattering matrices, which also provides a useful means of assessing the reliability of the simulations. Having access to analytical 2-D bend modes proves useful for the numerical implementation of this model, which is outlined in Section 3.4. Sections 3.4.1, 3.4.2 discuss simulation results for monomode and multimode settings. Section 3.5 presents the conclusions of the present work on bent-straight waveguide couplers.

3.1 Coupled mode theory

A rigorous approach to investigate an electromagnetic wave-propagation problem is to solve the Maxwell equations (in differential or integral form) for a given device, along with the material interface conditions, and relevant initial and boundary conditions. Analytic solutions exist for rather a few problems only. In many cases, one has to resort to computational techniques of more analytical character [99, 100, 88, 101, 102, 103], or to pure numerical methods, e.g. different versions of finite difference (time domain) methods or finite element methods [55, 57, 104, 105, 106]¹.

At times, the above rigorous approach may not be intuitive. Direct applications of the numerical methods do not provide much insight into the functioning of the devices in terms of their “special structures”. For devices made of directional couplers, i.e. formed by several more or less parallel waveguides in close vicinity, the above approaches play down the coupling viewpoint. To model such devices, a more pragmatic approximation technique - “Coupled mode theory” (CMT) is used [42, 50, 51, 52]. CMT has been quite successfully employed for the analysis of wave interaction in straight waveguides [35, 107] and fibers [108]. To our knowledge, most of the studies [21, 54, 109, 110] on CMT based modeling of interaction between bent/cavity waveguides and straight waveguides (in optical

¹For comprehensive information about finite difference time domain methods, see www.fdttd.org

regime) are based on Ref. [44], where a complex eigenfrequency model of the cavity waveguides is used. Also the interaction between the cavity and the straight waveguide is treated with a rather heuristic ‘‘coupled point’’ argument (see Eq.(48) in Ref.[44]).

Capitalizing on the availability of the real frequency analytical model of 2-D bent waveguides discussed in Chapter 2, in the subsequent sections we address the problem of wave interaction in bent-straight waveguide couplers in terms of a frequency domain spatial coupled mode theory model. This model is consistent with standard physical notions, and the coupling is modeled with systematically and rigorously derived coupled mode equations.

3.2 Bent-straight waveguide couplers

Consider the coupler configuration shown in Figure 3.1(a). The coupled mode theory description starts with the specification of the basis fields, here the time-harmonic modal solutions associated with the isolated bent (b) and straight cores (c). Customarily, the real, positive frequency ω is given by the vacuum wavelength λ ; we omit the common time dependence $\sim \exp(i\omega t)$ for the sake of brevity. Only forward propagating modes are considered, where, for convenience, we choose the z -axis of the Cartesian system as introduced in Figure 3.1 as the common propagation coordinate for all fields.

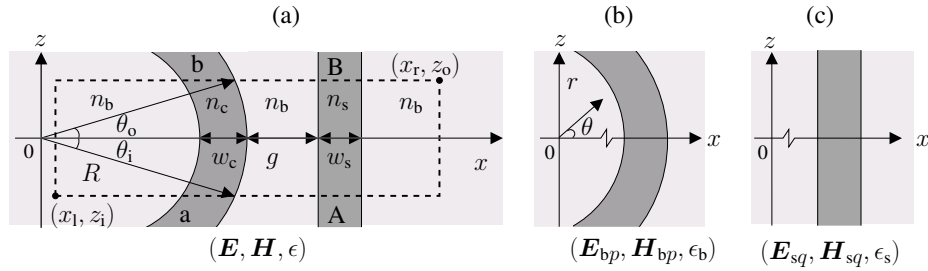


Figure 3.1: The bent-straight waveguide coupler setting (a). One assumes that the interaction between the waves supported by the bent and straight cores is restricted to the rectangular computational window $[x_l, x_r] \times [z_i, z_o]$. Inside this region the optical field is represented as a linear combination of the modal fields of the bent waveguide (b) and of the straight waveguide (c).

Let \mathbf{E}_{bp} , \mathbf{H}_{bp} , and ϵ_b represent the modal electric fields, magnetic fields, and the spatial distribution of the relative permittivity of the bent waveguide. Due to the

rotational symmetry, these fields are naturally given in the polar coordinate system r, θ associated with the bent waveguide. For the application in the CMT formalism, the polar coordinates are expressed in the Cartesian x - z -system, such that the basis fields for the cavity read

$$\begin{pmatrix} \mathbf{E}_{bp} \\ \mathbf{H}_{bp} \end{pmatrix}(x, z) = \begin{pmatrix} \tilde{\mathbf{E}}_{bp} \\ \tilde{\mathbf{H}}_{bp} \end{pmatrix}(r(x, z)) e^{-i\gamma_{bp}R\theta(x, z)}. \quad (3.1)$$

Here $\tilde{\mathbf{E}}_{bp}$ and $\tilde{\mathbf{H}}_{bp}$ are the radial dependent electric and magnetic parts of the mode profiles; the complex propagation constants γ_{bp} prescribe the harmonic dependences on the angular coordinate. Note that the actual values of γ_{bp} are related to the (arbitrary) definition of the bend radius R , see Section 2.4.1.

Likewise, \mathbf{E}_{sq} , \mathbf{H}_{sq} , and ϵ_s denote the modal fields and the relative permittivity associated with the straight waveguide. These are of the form

$$\begin{pmatrix} \mathbf{E}_{sq} \\ \mathbf{H}_{sq} \end{pmatrix}(x, z) = \begin{pmatrix} \tilde{\mathbf{E}}_{sq} \\ \tilde{\mathbf{H}}_{sq} \end{pmatrix}(x) e^{-i\beta_{sq}z}, \quad (3.2)$$

i.e. guided modes with profiles $\tilde{\mathbf{E}}_{sq}$, $\tilde{\mathbf{H}}_{sq}$ that depend on the lateral coordinate x , multiplied by the appropriate harmonic dependence on the longitudinal coordinate z , with positive propagation constants β_{sq} . Note that for the present 2-D theory all modal solutions can be computed analytically. While the modal analysis is fairly standard for straight multilayer waveguides with piecewise constant permittivity, for the bend structures we employ analytic solutions in terms of Bessel- and Hankel functions of complex order, computed by means of a bend mode solver as presented in Chapter 2.

Now the total optical electromagnetic field \mathbf{E} , \mathbf{H} inside the coupler region is assumed to be well represented by a linear combination of the modal basis fields (3.1), (3.2),

$$\begin{pmatrix} \mathbf{E} \\ \mathbf{H} \end{pmatrix}(x, z) = \sum_{v=b,s} \sum_{i=1}^{N_v} C_{vi}(z) \begin{pmatrix} \mathbf{E}_{vi} \\ \mathbf{H}_{vi} \end{pmatrix}(x, z) \quad (3.3)$$

with so far unknown amplitudes C_{vi} that are allowed to vary with the propagation coordinate z , and N_b , N_s denote number of bent waveguide and straight waveguide modes under consideration. This assumption forms the central approximation of the present CMT approach; no further approximations or heuristics enter, apart from the numerical procedures used for the evaluation of the CMT equations (section 3.4). Note that here, unlike e.g. in Ref. [44], no ‘‘phase matching’’ arguments appear; via the transformation $r, \theta \rightarrow x, z$ the tilt of the wave front of the bend modes (3.1) is taken explicitly into account.

3.2.1 Coupled mode equations

For the further procedures, the unknown coefficients C_{vi} are combined into amplitude vectors $\mathbf{C} = (\mathbf{C}_b, \mathbf{C}_s) = ((C_{bi}), (C_{si}))$. To determine equations for these unknowns, here we follow an approach that relies on a variational principle [111, 112]. Consider the functional

$$\begin{aligned} \mathcal{F}(\mathbf{E}, \mathbf{H}) = \iint [(\nabla \times \mathbf{E}) \cdot \mathbf{H}^* - (\nabla \times \mathbf{H}) \cdot \mathbf{E}^* \\ + i\omega\mu\mathbf{H} \cdot \mathbf{H}^* + i\omega\epsilon_0\epsilon\mathbf{E} \cdot \mathbf{E}^*] dx dz, \end{aligned} \quad (3.4)$$

a 2-D restriction of the functional for the 3-D setting given in [43], stripped from the boundary terms. For the present 2-D configurations, the convention of vanishing derivatives $\partial_y = 0$ applies to all fields; the curl-operators are to be interpreted accordingly. \mathcal{F} is meant to be viewed as being dependent on the six field components \mathbf{E} , \mathbf{H} . If \mathcal{F} becomes stationary with respect to arbitrary variations of these arguments, then \mathbf{E} and \mathbf{H} satisfy the Maxwell curl equations as a necessary condition:

$$\nabla \times \mathbf{E} = -i\omega\mu\mathbf{H}, \quad \nabla \times \mathbf{H} = i\omega\epsilon_0\epsilon\mathbf{E}. \quad (3.5)$$

We now restrict the functional to the fields allowed by the coupled mode ansatz. After inserting the trial field (3.3) into the functional (3.4), \mathcal{F} becomes a functional that depends on the unknown amplitudes \mathbf{C} . For the “best” approximation to a solution of the problem (3.5) in the form of the field (3.3), the variation of $\mathcal{F}(\mathbf{C})$ is required to vanish for arbitrary variations $\delta\mathbf{C}$. Disregarding again boundary terms, the first variations of \mathcal{F} at \mathbf{C} in the directions δC_{wj} , for $j = 1, \dots, N_w$ and $w = b, s$, are

$$\delta\mathcal{F} = \int \sum_{v=b,s} \sum_{i=1}^{N_v} \left\{ M_{vi,wj} \frac{dC_{vi}}{dz} - F_{vi,wj} C_{vi} \right\} \delta C_{wj}^* dz - c.c. \quad (3.6)$$

where *c.c.* indicates the complex conjugate of the preceding integrated term,

$$M_{vi,wj} = \langle \mathbf{E}_{vi}, \mathbf{H}_{vi}; \mathbf{E}_{wj}, \mathbf{H}_{wj} \rangle = \int \mathbf{a}_z \cdot (\mathbf{E}_{vi} \times \mathbf{H}_{wj}^* + \mathbf{E}_{wj}^* \times \mathbf{H}_{vi}) dx, \quad (3.7)$$

$$F_{vi,wj} = -i\omega\epsilon_0 \int (\epsilon - \epsilon_v) \mathbf{E}_{vi} \cdot \mathbf{E}_{wj}^* dx, \quad (3.8)$$

and where \mathbf{a}_z is a unit vector in the z -direction. Consequently, one arrives at the coupled mode equations

$$\sum_{v=b,s} \sum_{i=1}^{N_v} M_{vi,wj} \frac{dC_{vi}}{dz} - \sum_{v=b,s} \sum_{i=1}^{N_v} F_{vi,wj} C_{vi} = 0, \quad (3.9)$$

for all $j = 1, \dots, N_w$ and $w = b, s$ as a necessary condition for \mathcal{F} to become stationary for arbitrary variations δC_{wj} . Note that the same expression is also obtained from the complex conjugate part of equation (3.6). In matrix notation, equations (3.9) read

$$\mathbf{M}(z) \frac{d\mathbf{C}(z)}{dz} = \mathbf{F}(z) \mathbf{C}(z). \quad (3.10)$$

Here the entries of the matrices \mathbf{M} and \mathbf{F} are given by the integrals (3.7) and (3.8). Due to the functional form of the bend modes and the varying distance between the bent and straight cores, these coefficients are z -dependent.

Derivation of coupled mode equation by reciprocity technique

Alternatively, the coupled mode equations (3.9) or (3.10) can be derived by means of a ‘‘reciprocity’’ technique [43]. For any two electromagnetic fields $(\mathbf{E}_p, \mathbf{H}_p)$ and $(\mathbf{E}_q, \mathbf{H}_q)$ with corresponding relative permittivity distributions ϵ_p and ϵ_q , using the Maxwell equations one can derive the following identity,

$$\int \nabla \cdot (\mathbf{E}_p \times \mathbf{H}_q^* + \mathbf{E}_q^* \times \mathbf{H}_p) dx = -i\omega\epsilon_0 \int (\epsilon_p - \epsilon_q) \mathbf{E}_p \cdot \mathbf{E}_q^* dx, \quad (3.11)$$

commonly known as ‘‘reciprocity identity’’ or ‘‘Lorentz reciprocity theorem’’.

Apply Eq. (3.11) for $(\mathbf{E}, \mathbf{H}, \epsilon)$ and $(\mathbf{E}_{wj}, \mathbf{H}_{wj}, \epsilon_w)$. After straightforward manipulations with the coupled mode field ansatz (3.3) leads to

$$\begin{aligned} & \sum_{v=b,s} \sum_{i=1}^{N_v} \int \mathbf{a}_z \cdot (\mathbf{E}_{vi} \times \mathbf{H}_{wj}^* + \mathbf{E}_{wj}^* \times \mathbf{H}_{vi}) dx \frac{dC_{vi}}{dz} + \\ & \sum_{v=b,s} \sum_{i=1}^{N_v} \int \nabla \cdot (\mathbf{E}_{vi} \times \mathbf{H}_{wj}^* + \mathbf{E}_{wj}^* \times \mathbf{H}_{vi}) dx C_{vi} \\ & = -i\omega\epsilon_0 \sum_{v=b,s} \sum_{i=1}^{N_v} \int (\epsilon - \epsilon_w) \mathbf{E}_{vi} \cdot \mathbf{E}_{wj}^* dx C_{vi}. \end{aligned} \quad (3.12)$$

By applying the ‘‘reciprocity identity’’ for the second term on the left hand side of Eq.(3.12), and combining it with the right hand side, one obtains

$$\begin{aligned} & \sum_{v=b,s} \sum_{i=1}^{N_v} \int \mathbf{a}_z \cdot (\mathbf{E}_{vi} \times \mathbf{H}_{wj}^* + \mathbf{E}_{wj}^* \times \mathbf{H}_{vi}) dx \frac{dC_{vi}}{dz} \\ & = -i\omega\epsilon_0 \sum_{v=b,s} \sum_{i=1}^{N_v} \int (\epsilon - \epsilon_v) \mathbf{E}_{vi} \cdot \mathbf{E}_{wj}^* dx C_{vi}. \end{aligned} \quad (3.13)$$

Rewriting Eq. (3.13) in terms of the coefficients $M_{vi,wj}$, $F_{vi,wj}$ given by Eqs. (3.7), (3.8) leads to the coupled mode equations (3.9).

Coupled mode equations for couplers with monomodal waveguides

In the single mode case $N_b = N_s = 1$, Eq.(3.10) is given explicitly [71, 34] as

$$\begin{pmatrix} M_{bb} & M_{sb} \\ M_{bs} & M_{ss} \end{pmatrix} \frac{d}{dz} \begin{pmatrix} C_b \\ C_s \end{pmatrix} = \begin{pmatrix} F_{bb} & F_{sb} \\ F_{bs} & F_{ss} \end{pmatrix} \begin{pmatrix} C_b \\ C_s \end{pmatrix}, \quad (3.14)$$

where the mode index $p = q = 1$ is omitted for simplicity.

3.2.2 Transfer matrix and scattering matrix

To proceed further, the CMT equations are solved by numerical means. Brief details about the procedures are given in Section 3.4; the result can be stated in terms of a transfer matrix T that relates the CMT amplitudes at the output plane $z = z_o$ to the amplitudes at the input plane $z = z_i$ of the coupler region:

$$C(z_o) = T C(z_i). \quad (3.15)$$

It remains to relate the transfer matrix, obtained directly as the solution of the CMT equations on the limited computational window, to the coupler scattering matrix as required for the abstract model of Section 1.4 or Section 4.1, respectively.

Outside the coupler (i.e. outside the region $[x_l, x_r] \times [z_i, z_o]$), it is assumed that the interaction between the fields associated with the different cores is negligible. The individual modes propagate undisturbed according to the harmonic dependences on the respective propagation coordinates, such that the external fields are:

$$\begin{aligned} a_p \begin{pmatrix} \tilde{\mathbf{E}}_{bp} \\ \tilde{\mathbf{H}}_{bp} \end{pmatrix}(r) e^{-i\gamma_{bp}R(\theta - \theta_i)}, & \quad \text{for } \theta \leq \theta_i, \\ A_q \begin{pmatrix} \tilde{\mathbf{E}}_{sq} \\ \tilde{\mathbf{H}}_{sq} \end{pmatrix}(x) e^{-i\beta_{sq}(z - z_i)}, & \quad \text{for } z \leq z_i, \end{aligned} \quad (3.16)$$

and

$$\begin{aligned} b_p \begin{pmatrix} \tilde{\mathbf{E}}_{bp} \\ \tilde{\mathbf{H}}_{bp} \end{pmatrix}(r) e^{-i\gamma_{bp}R(\theta - \theta_o)}, & \quad \text{for } \theta \geq \theta_o, \\ B_q \begin{pmatrix} \tilde{\mathbf{E}}_{sq} \\ \tilde{\mathbf{H}}_{sq} \end{pmatrix}(x) e^{-i\beta_{sq}(z - z_o)}, & \quad \text{for } z \geq z_o. \end{aligned} \quad (3.17)$$

Here $\mathbf{a} = (a_p)$, $\mathbf{A} = (A_q)$ and $\mathbf{b} = (b_p)$, $\mathbf{B} = (B_q)$ are the constant external mode amplitudes at the input and output ports of the coupler (c.f. the corresponding definitions in the abstract resonator model of Section 1.4 or Section 4.1). See Figure 3.1 for the definitions of the coordinate offsets z_i , θ_i and z_o , θ_o .

For a typical coupler configuration, the guided modal fields of the straight waveguide are well confined to the straight core. On the contrary, due to the radiative nature of the fields, the bend mode profiles can extend far beyond the outer interface of the bent waveguide. Depending upon the specific physical configuration, the extent of these radiative parts of the fields varies, such that also outside the actual coupler region, the field strength of the bend modes in the region close to the straight core may be significant. Therefore, to assign the external mode amplitudes A_q, B_q , it turns out to be necessary to project the coupled field on the straight waveguide modes.

At a sufficient distance from the cavity, in the region where only the straight waveguide is present, the total field $\phi = (\mathbf{E}, \mathbf{H})$ can be expanded into the complete set of modal solutions of the eigenvalue problem for the straight waveguide. The basis set consists of a finite number of guided modes $\phi_{sq} = (\mathbf{E}_{sq}, \mathbf{H}_{sq})$ and a nonguided, radiative part ϕ_{rad} , such that

$$\phi = \sum_q B_q \phi_{sq} + \phi_{\text{rad}}, \quad (3.18)$$

where B_q are the constant amplitudes of ϕ_{sq} . These amplitudes can be extracted by applying the formal expansion to the total field (3.3) as given by the solution of the CMT equations. Using the orthogonality properties of the basis elements, the projection at the output plane $z = z_o$ of the coupler yields

$$B_q \exp(i\beta_{sq}z) = C_{sq} + \sum_{p=1}^{N_b} C_{bp} \frac{\langle \phi_{bp}; \phi_{sq} \rangle}{\langle \phi_{sq}; \phi_{sq} \rangle} = C_{sq} + \sum_{p=1}^{N_b} C_{bp} \frac{M_{bp,sq}}{M_{sq,sq}}. \quad (3.19)$$

where the mode overlaps $\langle \phi_{mi}; \phi_{nj} \rangle = \langle \mathbf{E}_{mi}, \mathbf{H}_{mi}; \mathbf{E}_{nj}, \mathbf{H}_{nj} \rangle = M_{mi,nj}$ occur already in the coupled mode equations (3.10). An expression analogous to (3.19) can be written for the projection at $z = z_i$, where the coefficients A_q are involved. What concerns the external amplitudes of the bend modes, no such procedure is required, since the field strength of the straight waveguide modes is usually negligible in the respective angular planes, where the major part of the bend mode profiles is located. Here merely factors are introduced that adjust the offsets of the angular coordinates in (3.16),(3.17).

Thus, given the solution (3.15) of the coupled mode equations in the form of the transfer matrix \mathbf{T} , the scattering matrix \mathbf{S} that relates the amplitudes a_p, b_p, A_q, B_q of the external fields as required in equation (1.1) is defined as

$$\mathbf{S} = \mathbf{Q} \mathbf{T} \mathbf{P}^{-1} \quad (3.20)$$

where \mathbf{P} and \mathbf{Q} are $(N_b + N_s) \times (N_b + N_s)$ matrices with diagonal entries $P_{p,p} = \exp(-i\gamma_{bp}R\theta_i)$ and $Q_{p,p} = \exp(-i\gamma_{bp}R\theta_o)$, for $p = 1, \dots, N_b$, followed by the entries $P_{q+N_b, q+N_b} = \exp(-i\beta_{sq}z_i)$ and $Q_{q+N_b, q+N_b} = \exp(-i\beta_{sq}z_o)$, for $q = 1, \dots, N_s$.

A lower left block is filled with entries $P_{q+N_b, p} = \exp(-i\beta_{sq}z) M_{bp, sq} / M_{sq, sq}|_{z=z_i}$ and $Q_{q+N_b, p} = \exp(-i\beta_{sq}z) M_{bp, sq} / M_{sq, sq}|_{z=z_o}$, for $q = 1, \dots, N_s$ and $p = 1, \dots, N_b$, respectively, that incorporate the projections. All other coefficients of \mathbf{P} and \mathbf{Q} are zero.

3.2.3 Remarks on the projection operation

Admittedly, at the first glance the projection operation might appear redundant, since the CMT solution in the form (3.3) provides directly amplitudes for the basis fields that occur also in the external field representation (3.16), (3.17). Here perhaps further explanatory remarks are necessary.

The physical field around the exit planes of the CMT window can be seen as a superposition of the outgoing guided modes of the bus core with their constant amplitudes, and a remainder, that, when expanded in the modal basis associated with the straight waveguide, is orthogonal to the guided waves. The notions of “vanishing interaction” or “decoupled” fields, as used e.g. for the motivation of the assumptions underlying the abstract framework of Section 1.4, are to be concretized in precisely this way: The guided waves in the straight core are stationary, iff projections onto the mode profiles at growing propagation distances lead to constant amplitudes A_q, B_q (apart from the phase changes according to the undisturbed propagation of the respective modes).

Now the coupled mode theory formalism is limited to the few non-orthogonal bend and straight modes included in the CMT ansatz, which are overlapping in the regions of the input and exit ports A and B of the coupler. Consequently, when the CMT procedures try to approximate both the guided and radiative part of the real field, the optimum approximations may well be superpositions with non-stationary coupled mode amplitudes C_{sq} of the modes of the bus waveguide. Indeed, as observed in Sections 3.4.1 and 3.4.2, the projected amplitudes $|B_q|^2$ (or the related scattering matrix elements $|S_{sq, wj}|^2$) become stationary, when viewed as a function of the exit port position z_o , while at the same time the associated CMT solution $|C_{sq}(z)|^2$ (or the elements $|T_{sq, wj}|^2$ of the transfer matrix) exhibit an oscillatory behaviour. Still, in the sense of the projections, one can speak of “non-interacting, decoupled” fields. That justifies the limitation of the computational window to z -intervals where the elements of \mathbf{S} (not necessarily of \mathbf{T}) attain constant absolute

values around the input and output planes.

In conclusion, it is at least partly misleading to stick to the familiar notion of “mode evolutions” computed by the CMT approach. If one abandons that viewpoint and regards the CMT procedures as just “a” method that generates an approximate field solution inside the computational window, then applying the projections to extract the external mode amplitudes appears perfectly reasonable.

3.3 Reciprocity of scattering matrix

For the analysis of the bent-straight waveguide couplers discussed in Section 3.2, we have considered only forward propagating modes. By considering backward propagating modes also, the corresponding full scattering matrix that relates the bidirectional amplitudes of the outgoing waves to the amplitudes of the corresponding incoming modes is given as:

$$\begin{pmatrix} a^- \\ A^- \\ b \\ B \end{pmatrix} = \begin{pmatrix} 0 & 0 & S_{bb}^- & S_{bs}^- \\ 0 & 0 & S_{sb}^- & S_{ss}^- \\ S_{bb} & S_{bs} & 0 & 0 \\ S_{sb} & S_{ss} & 0 & 0 \end{pmatrix} \begin{pmatrix} a \\ A \\ b^- \\ B^- \end{pmatrix}. \quad (3.21)$$

Here the superscripts $-$ indicate the amplitudes of backwards (anticlockwise) propagating waves, where the zeroes implement the assumption of negligible backreflections. The entries of the submatrices S_{vw} with $v, w = b, s$ represent the “coupling” from the modes of waveguide w to the fields supported by waveguide v .

A fundamental property of any linear optical circuit made of nonmagnetic materials is that the transmission between any two “ports” does not depend upon the propagation direction. The proof can be based e.g. on the integration of a reciprocity identity over the spatial domain covered by that circuit [43]. More specifically, the full scattering matrix of the reciprocal circuit has to be symmetric. The argument holds for circuits with potentially attenuating materials, in the presence of radiative losses, and irrespectively of the particular shape of the connecting cores. It relies crucially on the precise definition of the “ports” of the circuit, where independent ports can be realized either by mode orthogonality or by spatially well separated outlets.

Assuming that the requirements of that argument can be applied at least approximately to our present bent-straight waveguide couplers, one expects that the coupler scattering matrix is symmetric. For the submatrices this implies the following

equalities (T denotes the transpose):

$$\mathbf{S}_{bb} = (\mathbf{S}_{bb}^-)^T, \quad \mathbf{S}_{sb} = (\mathbf{S}_{bs}^-)^T, \quad \mathbf{S}_{bs} = (\mathbf{S}_{sb}^-)^T, \quad \mathbf{S}_{ss} = (\mathbf{S}_{ss}^-)^T. \quad (3.22)$$

If the coupler shown in Figure 3.1 is defined symmetrical with respect to the central plane $z = 0$ and if identical mode profiles are used for the incoming and outgoing fields, then one can further expect (see [43]) the transmission $\mathbf{A} \rightarrow \mathbf{b}$ to be equal to the transmission $\mathbf{B}^- \rightarrow \mathbf{a}^-$. Similarly, one expects equal transmissions $\mathbf{a} \rightarrow \mathbf{B}$ and $\mathbf{b}^- \rightarrow \mathbf{A}^-$, or

$$\mathbf{S}_{bs} = \mathbf{S}_{bs}^-, \quad \mathbf{S}_{sb} = \mathbf{S}_{sb}^-. \quad (3.23)$$

Consequently, according to equations (3.22) and (3.23), also the unidirectional scattering matrix

$$\mathbf{S} = \begin{pmatrix} \mathbf{S}_{bb} & \mathbf{S}_{bs} \\ \mathbf{S}_{sb} & \mathbf{S}_{ss} \end{pmatrix} \quad (3.24)$$

associated with the forward, clockwise propagation through the coupler, i.e. the lower left quarter block of the full matrix in equation (3.21) can be expected to be symmetric:

$$\mathbf{S}_{bs} = (\mathbf{S}_{sb})^T, \quad \mathbf{S}_{bs}^- = (\mathbf{S}_{sb}^-)^T. \quad (3.25)$$

Here translated to the multimode coupler setting, this means that “the coupling from the straight waveguide to the cavity bend is equal to the coupling from the cavity bend to the bus waveguide”.

3.4 Simulation results

The coupled mode equations (3.9), (3.10) are treated by numerical means on a rectangular computational window $[x_1, x_r] \times [z_i, z_o]$ as introduced in Figure 3.1. The solution involves the numerical quadrature of the integrals (3.7), (3.8) in the z -dependent matrices \mathbf{M} and \mathbf{F} , where a simple trapezoidal rule [113] is applied, using an equidistant discretization of $[x_1, x_r]$ into intervals of length h_x .

Subsequently, a standard fourth order Runge-Kutta scheme [113] serves to generate a numerical solution of the coupled mode equations over the computational domain $[z_i, z_o]$, which is split into intervals of equal length h_z . Exploiting the linearity of equation (3.10), the procedure is formulated directly for the transfer matrix \mathbf{T} , i.e. applied to the matrix equation

$$\frac{d\mathbf{T}(z)}{dz} = \mathbf{M}(z)^{-1} \mathbf{F}(z) \mathbf{T}(z) \quad (3.26)$$

with initial condition $\mathbf{T}(z_i) = \mathbf{I}$ (the identity matrix), such that $\mathbf{C}(z) = \mathbf{T}(z) \mathbf{C}(z_i)$. While the evaluation of the resonator properties via equations (3.20) and (1.4), (1.5) requires only the solution $\mathbf{T} = \mathbf{T}(z_o)$ at the coupler output plane $z = z_o$, also the examination of the evolutions of $\mathbf{T}(z)$, or $\mathbf{S}(z)$, respectively, turns out to be instructive.

Having explained how to compute the scattering matrices for the bent-straight waveguide couplers, in Section 3.4.1 and 3.4.2 we summarize a series of numerical results for the theory outlined in Section 3.2 and 3.3. Note that couplers with quite small radius with substantial refractive index contrast are considered as test structures. For the CMT approach, these represent rather extreme configurations, partially with strongly leaky fields, thus with relatively large field strengths in the regions where the CMT ansatz-field clearly violates the Maxwell equations. One expects that for couplers that consist of bent waveguides with large radii, i.e. with better confined bend modes, and more adiabatic interaction in the coupler regions, the CMT approach comes even closer to reality.

3.4.1 Coupler with monomodal bent waveguide

As the first example, we consider bent-straight waveguide couplers according to Figure 3.1, formed by straight and circularly bent cores of widths $w_s = 0.4 \mu\text{m}$ and $w_c = 0.5 \mu\text{m}$ with refractive index $n_c = n_s = 1.5$, embedded in a background with refractive index $n_b = 1$. The configurations differ with respect to the radius R of the outer bend interface, and with respect to the distance g between the cores. The interaction of waves with vacuum wavelength $\lambda = 1.05 \mu\text{m}$ is studied, $k = 2\pi/\lambda$ is the associated vacuum wavenumber. Both constituent waveguides are single-mode at the target wavelength, with mode profiles that are well confined to the respective cores. Figure 3.2 illustrates an example for the two basis fields. The longer outer tail of the bend profile is accompanied by a slight shift of the profile maximum towards the exterior of the bend.

The CMT simulations of the couplers are carried out on computational windows of $[x_l, x_r] \times [z_i, z_o] = [0, R + 10 \mu\text{m}] \times [-R + 1 \mu\text{m}, R - 1 \mu\text{m}]$, if $R \leq 5 \mu\text{m}$, otherwise on a window $[x_l, x_r] \times [z_i, z_o] = [R - 5 \mu\text{m}, R + 10 \mu\text{m}] \times [-8, 8] \mu\text{m}$, discretized with stepsizes of $h_x = 0.005 \mu\text{m}$ and $h_z = 0.1 \mu\text{m}$. For the two basis fields the CMT analysis generates 2×2 transfer matrices \mathbf{T} and scattering matrices \mathbf{S} that can be viewed as being z -dependent in the sense as discussed in Section 3.4. Figure 3.3 shows the evolution of the matrix elements with the position $z = z_o$ of the coupler output plane.

The matrix elements $T_{o,i}$ and $S_{o,i}$ relate the amplitudes of an input mode i to an

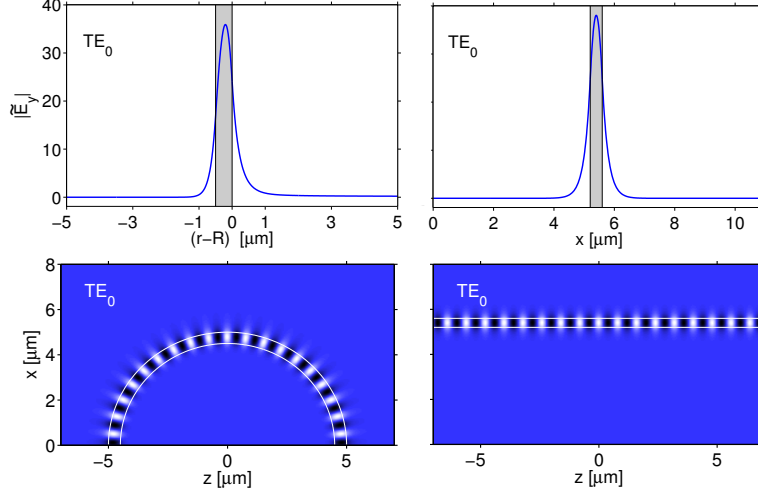


Figure 3.2: Normalized fundamental TE mode profiles $|\tilde{E}_y|$ (top) and snapshots of the propagating physical fields E_y (bottom) of the constituent bent (left) and straight waveguides (right) related to the coupler configurations of Section 3.4.1, for $R = 5 \mu\text{m}$. The effective mode indices of the basis fields are $\gamma/k = 1.29297 - i7.5205 \cdot 10^{-6}$ (bend mode), and $\beta/k = 1.3137$ (straight waveguide).

output mode o ; for the present normalized modes the absolute squares can thus be viewed as the relative fractions of optical power transferred from mode i at the input plane $z = z_i$ to mode o at the output plane $z = z_o$ of the coupler. After an initial interval, where these quantities remain stationary, one observes variations around the central plane $z = 0$ of the coupler, which correspond to the interaction of the waves. Here the nonorthogonal basis fields are strongly overlapping; it is therefore not surprising that the levels of specific components of $|T_{o,i}|^2$ and $|S_{o,i}|^2$ exceed 1 in this interval.

After the region of strongest interaction, near the end of the z -computational interval, one finds that the elements $|T_{b0,i}|^2$ that map to the bend mode amplitude become stationary again, while the elements $|T_{s0,i}|^2$ related to the output to the straight mode still show an oscillatory behaviour. This is due to the interference effects as explained in Section 3.2.3. The proper amplitudes of the modes of the bus channel can be extracted by applying the projection operation (3.19); the corresponding matrix elements $|S_{s0,i}|^2$ attain stationary values, such that the ‘‘coupling strength’’ predicted for the involved modes does not depend on the (to a certain degree arbitrary) position of the coupler output plane.

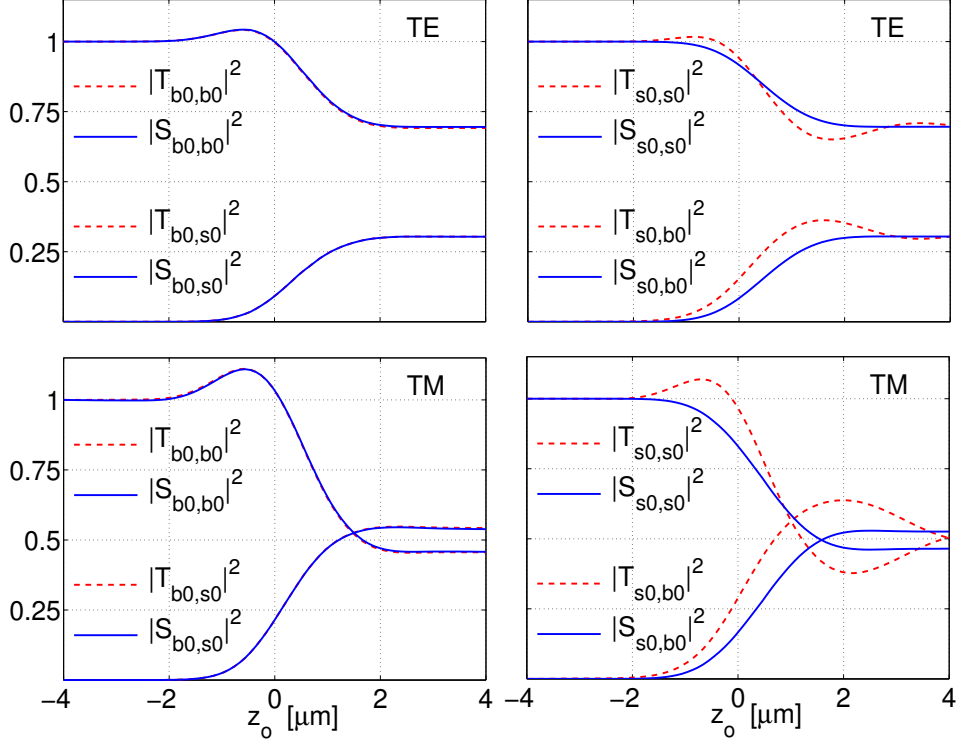


Figure 3.3: Elements of the transfer matrix T and scattering matrix S for TE (first row) and TM (second row) polarized light, versus the output plane position z_o , for couplers as introduced in Section 3.4.1 with $R = 5 \mu\text{m}$ and $g = 0.2 \mu\text{m}$.

Anyway, the scattering matrix S , that enters the relations (1.4), (1.5) for the transmission properties of the resonator device, should be considered a static quantity, computed for the fixed computational interval $[z_i, z_o]$. From the design point of view, one is interested in the elements of this matrix (the “coupling coefficients”) as a function of the resonator / coupler design parameters. Figure 3.4 summarizes the variation of S with the width of the coupler gap, for a series of different bend radii.

Uniformly for all radii and for both polarizations one observes the following trends. For large gap widths, the non-interacting fields lead to curves that are constant, at levels of unity ($|S_{s0,s0}|^2$, full transmission along the straight waveguide), moderately below unity ($|S_{b0,b0}|^2$, attenuation of the isolated bend mode, stronger for the TM field), or zero ($|S_{b0,s0}|^2$ and $|S_{s0,b0}|^2$, decoupled fields). As the gap width decreases, the growing interaction strength between the modes in the two cores causes increasing cross coupling $|S_{b0,s0}|^2$, $|S_{s0,b0}|^2$ and decreasing self coupling

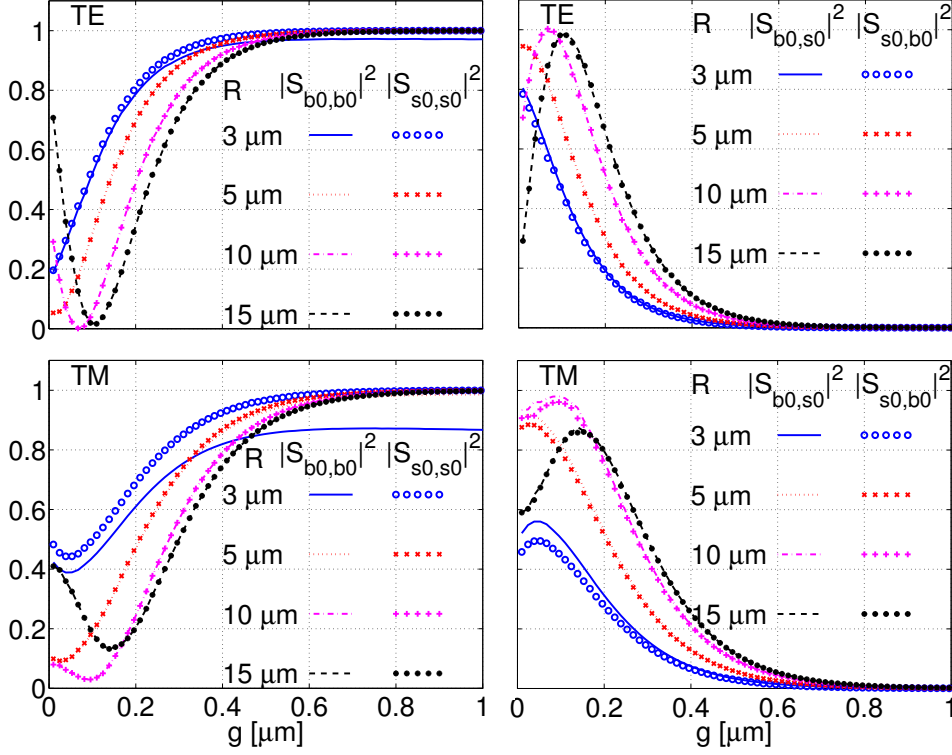


Figure 3.4: Scattering matrix elements $|S_{o,i}|^2$ versus the gap width g , for couplers as considered in Section 3.4.1 with cavity radii $R = 3, 5, 10, 15 \mu\text{m}$, for TE (first row) and TM (second row) polarized waves.

$|S_{s0,s0}|^2$, $|S_{b0,b0}|^2$. This continues until a maximum level of power transfer is attained (where the level should depend on the “phase mismatch” between the basis fields, though a highly questionable notion in case of the bend modes [114]).

If the gap is further reduced, the cross coupling coefficients decrease, even if a growing strength of the interaction can be expected; the decrease can be attributed to a process of “forth and back coupling”, as shown in Figure 3.5, where along the propagation axis a major part of the optical power changes first from the input channel to the second waveguide, then back to the input core. One should therefore distinguish clearly between the magnitude of the coefficients (3.8) in the differential equations that govern the coupling process, and the solution of these equations for a finite interval, the net effect of the coupler, represented by the scattering matrix S .

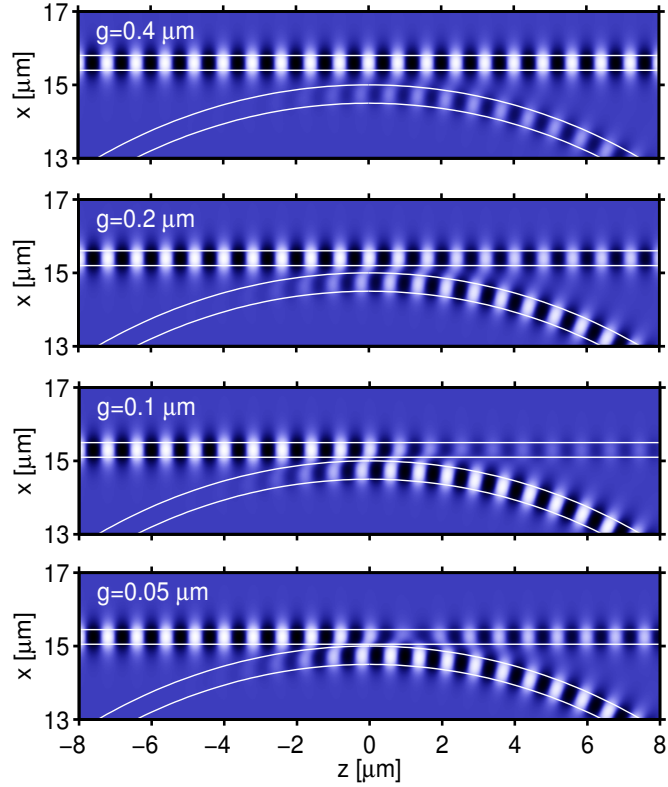


Figure 3.5: Forth and back coupling as the separation distance g is reduced. The plots show the real physical E_y field for the coupler configuration as in Section 3.4.1, with $R = 15 \mu\text{m}$.

For the symmetric computational windows used for the present simulations, the abstract reasoning of Section 3.3 predicts symmetric coupler scattering matrices. According to Figures 3.3 and 3.4, this constraint is respected remarkably well by the CMT simulations. In Figure 3.3, the curves related to $|S_{s0,b0}|^2$ and $|S_{b0,s0}|^2$ end in nearly the same level at $z = z_0$. Figure 3.4 shows pairs of close curves for the cross coupling coefficients, where larger deviations occur only for rather extreme configurations with small bend radii and gaps close to zero; the deviations are more pronounced for the TM case. Here one might question the validity of the assumptions underlying the CMT ansatz (3.3). Otherwise the symmetry of the scattering matrices provides a useful means to assess the accuracy of the CMT simulations, beyond merely the power balance constraint.

In the “standard resonator model”, as seen from Eqs. (1.4), (1.5), the spectral re-

sponse of the resonators depends on the scattering matrix entries. Therefore it is useful to look at the wavelength dependence of the scattering matrix, which is shown in the plots of Figure 3.6 and 3.7.

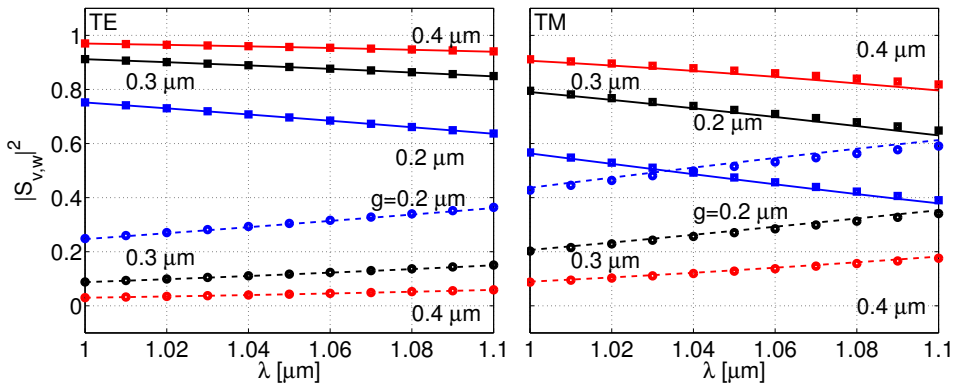


Figure 3.6: Wavelength dependence of the entries (absolute square) of the scattering matrix S , $|S_{b0,b0}|^2$ (solid line), $|S_{b0,s0}|^2$ (dashed line), $|S_{s0,b0}|^2$ (circles), and $|S_{s0,s0}|^2$ (squares). The coupler configuration is as in Section 3.4.1, with $R = 5 \mu\text{m}$ and gap widths $g = 0.2 \mu\text{m}, 0.3 \mu\text{m}, 0.4 \mu\text{m}$.

Note that the scattering matrix entries are complex numbers. While the absolute square of these entries, as shown in Figure 3.6, shows a monotonic behaviour, the corresponding real and imaginary parts, shown in Figure 3.7, oscillate. These oscillations are due to phase changes experienced by the modal fields while propagating along the coupler. We will elaborate this point further in Section 4.3, with a numerical example in Section 4.4.1.

As the wavelength increases, the bent waveguide and straight waveguide modes become less confined, and the interaction between these modes increases. This results in a steady increase of the cross coupling coefficients $|S_{b0,s0}|^2, |S_{s0,b0}|^2$, and a decrease of the self coupling coefficients $|S_{b0,b0}|^2, |S_{s0,s0}|^2$. For varying wavelengths and for both polarizations, the simulation results in Figures 3.6 and 3.7 show that reciprocity is maintained very well, i.e. the cross coupling coefficients $S_{b0,s0}$ and $S_{s0,b0}$ coincide as complex numbers (see the plots in the second row of Figure 3.7). Slight deviations can be observed for the configurations with $g = 0.2 \mu\text{m}$ and TM polarization, for the structure with the strongest interaction and lossy, less regular fields.

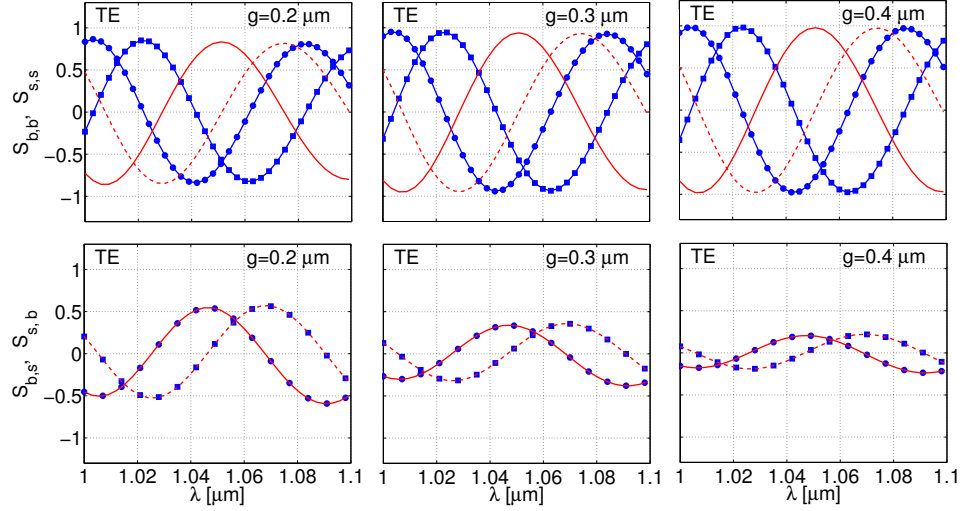


Figure 3.7: Wavelength dependence of complex valued entries of the scattering matrix S . For each separation distance, the plots in the first row show $\Re(S_{b_0, b_0})$ (line with circles), $\Im(S_{b_0, b_0})$ (line with squares), $\Re(S_{s_0, s_0})$ (solid line), $\Im(S_{s_0, s_0})$ (dashed line), and the plots in the second row show $\Re(S_{b_0, s_0})$ (circles), $\Im(S_{b_0, s_0})$ (squares), $\Re(S_{s_0, b_0})$ (solid line), $\Im(S_{s_0, b_0})$ (dashed line). \Re and \Im denote the real and imaginary parts of the complex numbers. Coupler configurations are as in Figure 3.6.

3.4.2 Coupler with multimodal bent waveguide

If the core width of a bent waveguide is increased beyond a certain limit, then as discussed in Section 2.4.5, the whispering gallery regime is reached, where the modes are guided by just the outer dielectric interface. Figure 3.8 illustrates the first four lowest order whispering gallery modes that are supported by a structure with the parameters of the previous ring segments, where the interior has been filled with the core material. If the resulting disk is employed as the cavity in a resonator structure, all bend modes with reasonably low losses must be suspected to be relevant for the functioning of the device. Therefore we now consider bent-straight coupler configurations, where the bend supports multiple whispering gallery modes.

A parameter set similar to Section 3.4.1 is adopted, with $n_c = n_s = 1.5$, $n_b = 1.0$, $R = 5 \mu\text{m}$, $w_c = R$, $w_s = 0.4 \mu\text{m}$, $g = 0.2 \mu\text{m}$, for the target wavelength $\lambda = 1.05 \mu\text{m}$. The CMT analysis of the coupler structures is carried out on a computational window $[x_l, x_r] = [0, 15] \mu\text{m}$, $[z_i, z_o] = [-4, 4] \mu\text{m}$ with large extent in the (radial) x -direction, in order to capture the radiative parts of the lossy higher

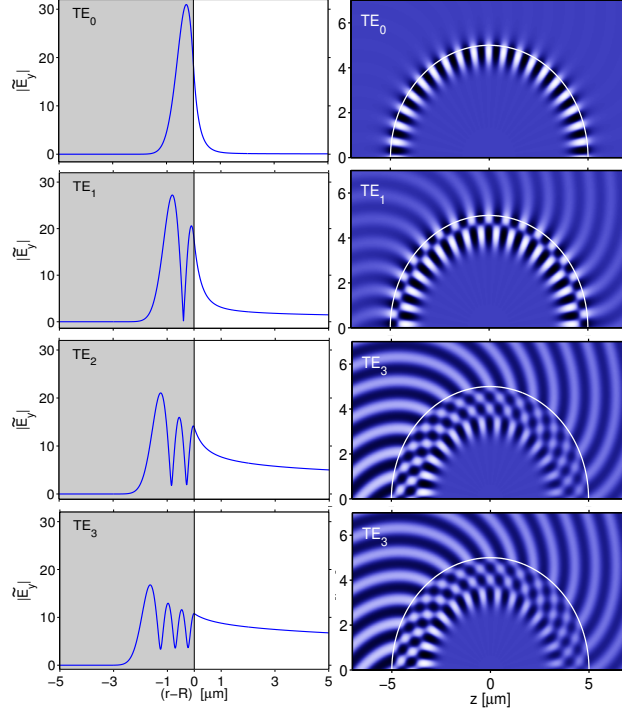


Figure 3.8: TE polarized whispering gallery modes; basis fields for the CMT analysis of the multimode couplers of Section 3.4.2. The plots show the absolute value $|\tilde{E}_y|$ of the radial mode profile (left) and snapshots of the propagating physical field E_y (right). The effective mode indices γ_j/k related to the bend radius $R = 5 \mu\text{m}$ are $1.32793 - i 9.531 \cdot 10^{-7}$ (TE_0), $1.16931 - i 4.032 \cdot 10^{-4}$ (TE_1), $1.04222 - i 5.741 \cdot 10^{-3}$ (TE_2), and $0.92474 - i 1.313 \cdot 10^{-2}$ (TE_3), for $\lambda = 1.05 \mu\text{m}$. All modes are power normalized.

order bend fields. Stepsizes for the numerical integrations are $h_x = 0.005 \mu\text{m}$, $h_z = 0.1 \mu\text{m}$, as before.

It is not a priori evident, how many basis fields are relevant for a particular simulation. Figure 3.9 shows the effect of the inclusion of the higher order bend modes on the evolution of the primary coefficients of the scattering matrix \mathbf{S} .

The self coupling coefficient $|\mathbf{S}_{b_0,b_0}|^2$ of the fundamental bend field is hardly influenced at all, and there is only a minor effect on the cross coupling coefficients $|\mathbf{S}_{s_0,b_0}|^2$ and $|\mathbf{S}_{b_0,s_0}|^2$. Inclusion of the first order bend field reduces merely the self coupling coefficient $|\mathbf{S}_{s_0,s_0}|^2$ of the straight mode by a substantial amount, due to the additional coupling to that basis field. Apparently, for the present structure it

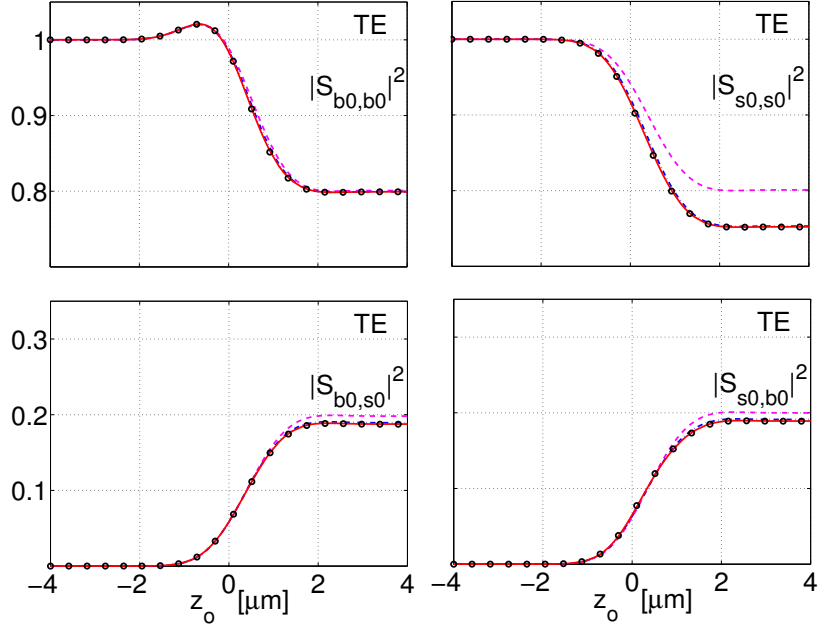


Figure 3.9: CMT analysis of the multimode coupler of Section 3.4.2, effect of the inclusion of higher order cavity modes on the evolution of the scattering matrix. Results for TE waves with one (dashed line), two (dash-dotted line), three (solid line), and four cavity modes (dotted line) taken into account. Note the different vertical axes of the plots.

is sufficient to take just the two or three lowest order bend modes into account. This hints at one of the advantages of CMT approach, where one can precisely analyze the significance of the individual basis modes. We will resume this issue in Section 4.4.2.

With three cavity fields and the mode of the straight waveguide, the CMT simulations lead to coupler scattering matrices of dimension 4×4 . Curves for the evolution of the 16 elements of the propagation and scattering matrices \mathbf{T} , \mathbf{S} are collected in Figure 3.10. Just as in Section 3.4.1, the application of the projection procedure to extract the stationary levels of $|S_{s0,j}|^2$, $|S_{j,s0}|^2$ from the nonstationary quantities $|T_{s0,j}|^2$, $|T_{j,s0}|^2$ at the exit port of the coupler is essential.

Again, the agreement of the exit levels of all cross coupling coefficients indicates that reciprocity is satisfied. In contrast to Figure 3.3, the noticeable decay of the self coupling coefficients $|S_{b1,b1}|^2$, $|S_{b2,b2}|^2$ is due to the strong attenuation of the basis fields, as directly introduced into \mathbf{S} via equation (3.20).

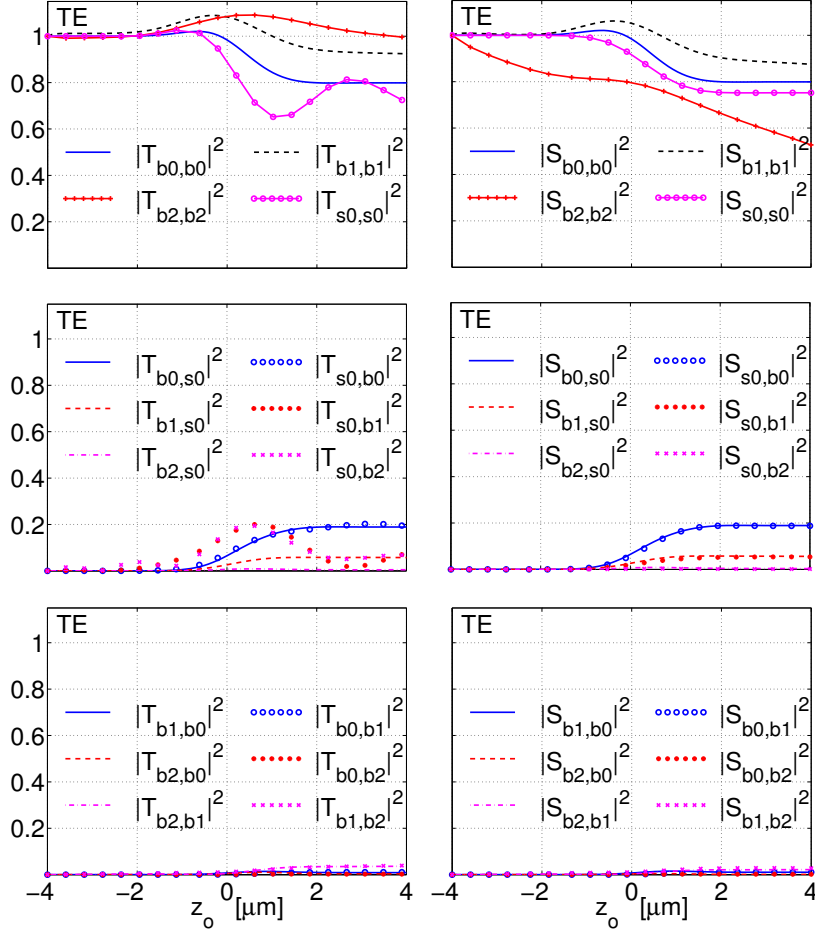


Figure 3.10: Evolution of the propagation matrix \mathbb{T} and scattering matrix \mathbb{S} for the coupler configuration with multimode bend as specified in Section 3.4.2; CMT results with four basis fields.

According to Figure 3.11, the elements of the scattering matrix exhibit a similar variation with the gap width as found for the former monomode bent-straight waveguide coupler (cf. Figure 3.4). With growing separation distance the cross coupling coefficients tend to zero. The constant levels attained by the self coupling coefficients of the bent modes are determined by the power the respective mode loses in traversing the computational window. Also here, with the exception of configurations with almost closed gap, we find that cross coupling coefficients with reversed indices coincide, i.e. that the simulations obey reciprocity.

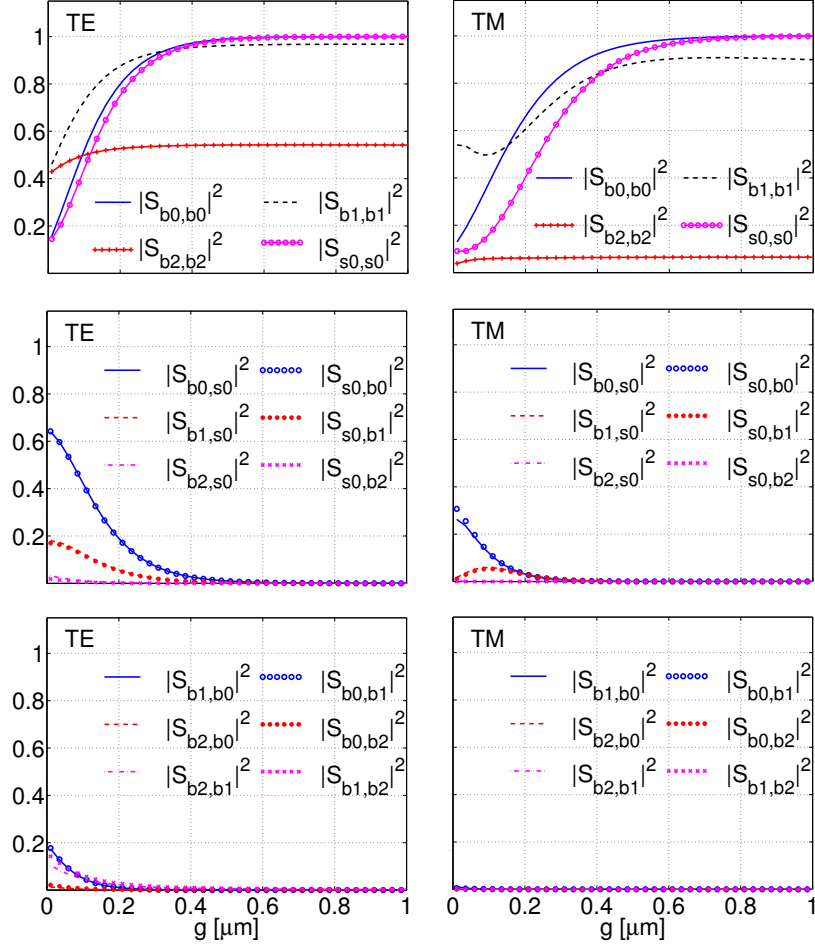


Figure 3.11: Scattering matrix elements $|S_{o,i}|^2$ versus the gap width g for the coupler structures of Section 3.4.2 for TE (top) and TM polarization (bottom). The CMT simulations take three whispering gallery modes and the field of the straight waveguide into account.

3.5 Concluding remarks

In this chapter, we presented a spatial coupled mode theory based model of 2-D bent-straight waveguide couplers. In this frequency domain approach, coupled mode equations are rigorously derived by a variational principle. Availability of 2-D analytical bent waveguide modes facilitates the implementation of the model consistent with standard physical notions. By solving the coupled mode equations

numerically, and projecting the resulting coupled mode field on the modes of the straight waveguide, we obtained the scattering matrices of the couplers. In symmetrical coupler settings, the scattering matrices satisfy the reciprocity property, that permits to assess the validity of the simulation results.

Using the above coupled mode theory model, a detailed study of the effects of separation distance, the radius of the bent waveguide, and the wavelength on the scattering matrices has been carried out. For the couplers involving bent waveguides that support multiple whispering gallery modes, one can systematically investigate the significance of the individual modes. In combination with analytically computed bent mode propagation constants, the model allows to calculate rigorously the free parameters in the “standard resonator model” and to analyze the spectral response of the microresonators (Sections 1.4, 4.1). While the present study discusses only 2-D couplers, this theory can be extended in a straightforward way to the 3-D setting, as discussed in detail in Ref. [69].

Chapter 4

Microresonators

Circular integrated optical microresonators are increasingly employed as compact and versatile wavelength filters. In this chapter, we investigate an ab-initio 2-D frequency domain model for these devices. The resonators are functionally represented in terms of two couplers with appropriate connections using bent and straight waveguides. The abstract scattering matrices of these couplers and the propagation constants of the cavity bends allow to compute the spectral responses of the resonators. These parameters are calculated by means of the rigorous analytical model of bent waveguides, and the spatial coupled mode theory model of the constituent bent-straight waveguide couplers. We present results for the spectral response and field examples for microresonators with mono- and multi-modal cavities for TE and TM polarizations. Comparisons with finite difference time domain simulations show very good overall agreement. Effect of the separation distances on the spectral response is investigated. Also examples for the effect of slight changes of the core refractive index on the resonator spectra, evaluated by perturbational expressions, are presented.

Parts of this chapter are adapted from:

K. R. Hiremath, R. Stoffer, M. Hammer. *Modeling of circular integrated optical microresonators by 2-D frequency domain coupled mode theory*. Optics Communications. (accepted).

In Section 1.4 we discussed the “standard resonator model” for structures with monomodal waveguides. Knowing the propagation constants of the cavity segments and the scattering matrices of the bent-straight waveguide couplers, one can compute the throughput power and the dropped power for the entire resonator devices. As explained in Chapter 2, the required propagation constants of bent waveguides can be calculated analytically. With the coupled mode theory model of bent-straight waveguide couplers, as presented in Chapter 3, one can reckon the required scattering matrices. Thus, given the geometrical and material parameters of a resonator, the spectral response can be computed. Preliminary results of this approach are contained in Refs. [34, 71].

In this chapter, we generalize the above resonator model to the multimodal setting. The chapter is organized as follows. Section 4.1 introduces the schematic microresonator model, formulated directly for configurations with multimode cavities. Section 4.3 outlines how to compute the spectral response of the resonators. Section 4.4 provides a series of example simulations, including the benchmarking against independent rigorous numerical calculations. A detailed study of effect of the separation distances on the resonator spectral response is presented in Section 4.5. Tuning of resonators is investigated in Section 4.6.

4.1 Abstract microresonator model

Referring to the classification of resonator types given in [53], we treat the circular microcavities as traveling wave resonators in the framework of a pure frequency domain description. Neglecting reflected waves turns out to be adequate even for the present devices with already quite small radii (though we can check this only implicitly via comparison to numerical results). One expects this approximation to break down for even smaller cavities, where the interaction between the waves in the bus waveguides and the cavity can no longer be regarded as adiabatic. In that regime of standing wave resonators descriptions similar to those given in Refs. [53, 115] would have to be applied, that take reflected waves fully into account.

The resonators investigated in this chapter consist of ring or disk shaped dielectric cavities, evanescently coupled to two parallel straight bus cores. We consider guided-wave scattering problems in the frequency domain, where a time-harmonic optical signal $\sim \exp(i\omega t)$ of given real frequency ω is present everywhere. Cartesian coordinates x, z are introduced for the spatially two dimensional description as shown in Figure 4.1. The structure and all TE- or TM-polarized optical fields are assumed to be constant in the y -direction.

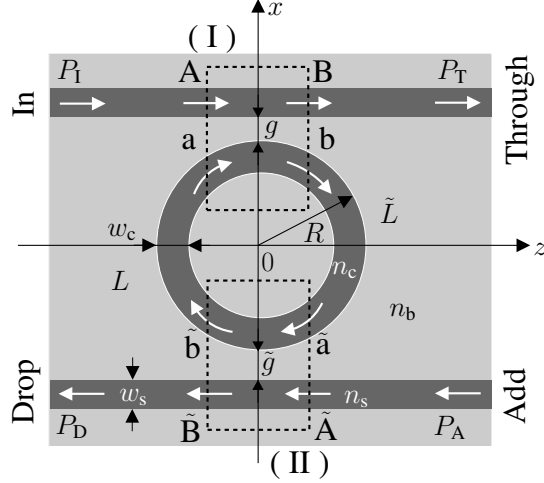


Figure 4.1: Schematic microresonator representation: A cavity of radius R , core refractive index n_c and width w_c is placed between two straight waveguides with core refractive index n_s and width w_s , with gaps of width g and \tilde{g} between the cavity and the bus waveguides. n_b is the background refractive index. The device is divided into two couplers (I), (II), connected by cavity segments of lengths L and \tilde{L} outside the coupler regions.

Adhering to the most common description for microring-resonators [35, 34], the devices are divided into two bent-straight waveguide couplers, which are connected by segments of the cavity ring. Half-infinite pieces of straight waveguides constitute the external connections, where the letters A, B, \tilde{A} , \tilde{B} (external) and a, b, \tilde{a} , \tilde{b} (internal) denote the coupler ports. If one accepts the approximation that the interaction between the optical waves in the cavity and in the bus waveguides is negligible outside the coupler regions, then this functional decomposition reduces the microresonator description to the mode analysis of straight and bent waveguides, and the modeling of the bent-straight waveguide couplers.

Assuming that all transitions inside the coupler regions are sufficiently smooth, such that reflections do not play a significant role for the resonator functioning, we further restrict the model to unidirectional wave propagation, as indicated by the arrows in Figure 4.1. Depending on the specific configuration, this assumption can be justified or not; at least for the structures considered in Section 4.4.2 we observed this approximation to be adequate.

Consider coupler (I) first. Suppose that the straight cores support N_s guided modes with propagation constants β_{sq} , $q = 1, \dots, N_s$. For the cavity, N_b bend modes are taken into account. Due to the radiation losses, their propagation constants

$\gamma_{bp} = \beta_{bp} - i\alpha_{bp}$, $p = 1, \dots, N_b$, are complex valued [114]. Here β_{sq} , β_{bp} and α_{bp} are real positive numbers. The variables A_q , B_q , and a_p , b_p , denote the directional amplitudes of the properly normalized “forward” propagating (clockwise direction, cf. Figure 4.1) basis modes in the respective coupler port planes, combined into amplitude (column) vectors \mathbf{A} , \mathbf{B} , and \mathbf{a} , \mathbf{b} . A completely analogous reasoning applies to the second coupler, where a symbol $\tilde{\cdot}$ identifies the mode amplitudes $\tilde{\mathbf{A}}$, $\tilde{\mathbf{B}}$, and $\tilde{\mathbf{a}}$, $\tilde{\mathbf{b}}$ at the port planes.

The model of Chapter 3 for unidirectional wave propagation through the coupler regions provides scattering matrices \mathbf{S} , $\tilde{\mathbf{S}}$, such that the coupler operation is represented as

$$\begin{pmatrix} \mathbf{b} \\ \mathbf{B} \end{pmatrix} = \mathbf{S} \begin{pmatrix} \mathbf{a} \\ \mathbf{A} \end{pmatrix}, \quad \begin{pmatrix} \tilde{\mathbf{b}} \\ \tilde{\mathbf{B}} \end{pmatrix} = \tilde{\mathbf{S}} \begin{pmatrix} \tilde{\mathbf{a}} \\ \tilde{\mathbf{A}} \end{pmatrix}. \quad (4.1)$$

Outside the coupler regions the bend modes used for the description of the field in the cavity propagate independently, with the angular / arc-length dependence given by their propagation constants (cf. equation (3.1)). Hence the amplitudes at the entry and exit ports of the connecting cavity segments are related to each other as

$$\mathbf{a} = \mathbf{G} \tilde{\mathbf{b}} \quad \text{and} \quad \tilde{\mathbf{a}} = \tilde{\mathbf{G}} \mathbf{b}, \quad (4.2)$$

where \mathbf{G} and $\tilde{\mathbf{G}}$ are $N_b \times N_b$ diagonal matrices with entries $G_{p,p} = \exp(-i\gamma_{bp}L)$ and $\tilde{G}_{p,p} = \exp(-i\gamma_{bp}\tilde{L})$, respectively, for $p = 1, \dots, N_b$.

For the guided wave scattering problem, modal powers $P_{Tq} = |A_q|^2$ and $P_{Aq} = |\tilde{A}_q|^2$ are prescribed at the In-port \mathbf{A} and at the Add-port $\tilde{\mathbf{A}}$ of the resonator, and one is interested in the transmitted powers $P_{Tq} = |B_q|^2$ at port \mathbf{B} and the backward dropped powers $P_{Dq} = |\tilde{B}_q|^2$ at port $\tilde{\mathbf{B}}$. The linear system established by equations (4.1) and (4.2) is to be solved for \mathbf{B} and $\tilde{\mathbf{B}}$, given values of \mathbf{A} and $\tilde{\mathbf{A}}$. Due to the linearity of the device the restriction to an excitation in only one port, here port \mathbf{A} , with no incoming Add-signal $\tilde{\mathbf{A}} = \mathbf{0}$, is sufficient. One obtains

$$\mathbf{B} = (\mathbf{S}_{sb} \mathbf{G} \tilde{\mathbf{S}}_{bb} \tilde{\mathbf{G}} \Omega^{-1} \mathbf{S}_{bs} + \mathbf{S}_{ss}) \mathbf{A}, \quad \tilde{\mathbf{B}} = (\tilde{\mathbf{S}}_{sb} \tilde{\mathbf{G}} \Omega^{-1} \mathbf{S}_{bs}) \mathbf{A} \quad (4.3)$$

for the amplitudes of the outgoing guided modes in the Through- and Drop-ports, and

$$\mathbf{b} = \Omega^{-1} \mathbf{S}_{bs} \mathbf{A}, \quad \tilde{\mathbf{b}} = \tilde{\mathbf{S}}_{bb} \tilde{\mathbf{G}} \Omega^{-1} \mathbf{S}_{bs} \mathbf{A} \quad (4.4)$$

for the internal mode amplitudes in the cavity, where $\Omega = \mathbf{I} - \mathbf{S}_{bb} \mathbf{G} \tilde{\mathbf{S}}_{bb} \tilde{\mathbf{G}}$.

Among the factors in the expressions (4.3) and (4.4) only the inverse of Ω can be expected to introduce a pronounced wavelength dependence. Thus Ω^{-1} can be viewed as a resonance denominator in matrix form; resonances appear in case Ω becomes nearly singular, i.e. exhibits an eigenvalue close to zero. This “resonance

condition” permits a quite intuitive interpretation: Resonances appear if a field amplitude vector is excited inside the cavity, that corresponds to a close-to-zero eigenvalue of Ω , or a unit eigenvalue of $\mathbf{S}_{\text{bb}}\mathbf{G}\tilde{\mathbf{S}}_{\text{bb}}\tilde{\mathbf{G}}$. That relates to a field which reproduces itself after propagating consecutively along the right cavity segment, through coupler (II), along the left cavity segment, and finally through coupler (I).

In general, resonances must be expected to involve all bend modes that are taken into account for the description of the cavity field, due to the interaction caused by the presence of the straight cores (cf. e.g. the example of the hybrid cavity ring given in Ref. [69]). If, however, this direct interaction between the bend modes is weak, the matrices \mathbf{S}_{bb} and $\tilde{\mathbf{S}}_{\text{bb}}$ become nearly diagonal just like \mathbf{G} and $\tilde{\mathbf{G}}$, and resonances can be ascribed to individual cavity modes. Analogously to the case of standing wave resonators [115], this viewpoint allows a quantitative characterization of resonances associated with “almost isolated” cavities, where the bus waveguides are absent. Also for the numerical examples in Section 4.4.2 we found this regime to be realized; resonances can be classified as belonging to specific bend modes by inspecting the mode amplitudes that establish inside the cavity at the resonance wavelength.

In case of a configuration with single mode cavity and bus cores, further evaluation of expressions (4.3) and (4.4) is presented in Section 1.4; one obtains the familiar explicit, parameterized expressions for the transmitted and dropped power, for the free spectral range and the resonance width, for finesse and Q-factor of the resonances, etc. Here the above resonance condition means that at coupler (I) the incoming signal from the bus waveguide is in phase with the wave propagating already along the cavity, and that it compensates the propagation loss of the cavity round trip. Resonances appear as a drop in the directly transmitted power P_{T} , and a simultaneous peak in the dropped power P_{D} . Assuming that this reasoning is also applicable to a multimode configuration with weak interaction, one can establish separate resonance conditions for the individual cavity modes, which in general will be satisfied at different wavelengths. The power spectrum of the microresonator shows a systematically repeating pattern with multiple extrema, where each resonance corresponds to cavity modes of different orders. See Figure 4.9 for an example.

4.2 Scattering matrix analysis of the full resonator

Treating the resonator shown in Figure 4.1 as a black box with four external ports A, B, $\tilde{\text{A}}$, $\tilde{\text{B}}$, let’s assume that the response of the resonator is characterized by an abstract bidirectional resonator scattering matrix \mathcal{S} . Let A_{i} , B_{i} , \tilde{A}_{i} , \tilde{B}_{i} be the amplitudes of incoming fields, and A_{o} , B_{o} , \tilde{A}_{o} , \tilde{B}_{o} be the outgoing field

amplitudes at the respective ports. Then one can write

$$\begin{pmatrix} \mathbf{A}_o \\ \mathbf{B}_o \\ \tilde{\mathbf{A}}_o \\ \tilde{\mathbf{B}}_o \end{pmatrix} = \begin{pmatrix} 0 & \mathcal{S}_{AB} & 0 & \mathcal{S}_{A\tilde{B}} \\ \mathcal{S}_{BA} & 0 & \mathcal{S}_{B\tilde{A}} & 0 \\ 0 & \mathcal{S}_{\tilde{A}B} & 0 & \mathcal{S}_{\tilde{A}\tilde{B}} \\ \mathcal{S}_{\tilde{B}A} & 0 & \mathcal{S}_{\tilde{B}\tilde{A}} & 0 \end{pmatrix} \begin{pmatrix} \mathbf{A}_i \\ \mathbf{B}_i \\ \tilde{\mathbf{A}}_i \\ \tilde{\mathbf{B}}_i \end{pmatrix}, \quad (4.5)$$

where the zeros represent negligible backreflections. The interpretation of the scattering matrix elements is as for the bent-straight waveguide coupler (see Section 3.3).

Again following the reciprocity arguments for linear circuits made of nonmagnetic materials (see Section 3.3), the above scattering matrix is symmetric, i.e.

$$\mathcal{S}_{BA} = (\mathcal{S}_{AB})^T, \quad \mathcal{S}_{\tilde{B}A} = (\mathcal{S}_{\tilde{A}B})^T, \quad \mathcal{S}_{\tilde{A}B} = (\mathcal{S}_{B\tilde{A}})^T, \quad \mathcal{S}_{\tilde{A}\tilde{B}} = (\mathcal{S}_{\tilde{B}\tilde{A}})^T, \quad (4.6)$$

where the superscript T represents the transpose.

If the resonator shown in Figure 4.1 is defined symmetrical with respect to the central plane $z = 0$, and if identical mode profiles are used for the incoming and outgoing fields, then one can further expect the transmission $\mathbf{A} \rightarrow \tilde{\mathbf{B}}$ to be equal to the transmission $\mathbf{B} \rightarrow \tilde{\mathbf{A}}$. Similarly, one expects equal transmissions $\tilde{\mathbf{A}} \rightarrow \mathbf{B}$ and $\tilde{\mathbf{B}} \rightarrow \mathbf{A}$. Therefore one has

$$\mathcal{S}_{\tilde{B}A} = \mathcal{S}_{\tilde{A}B}, \quad \mathcal{S}_{B\tilde{A}} = \mathcal{S}_{A\tilde{B}}. \quad (4.7)$$

From Eq. (4.6), (4.7), one obtains

$$\mathcal{S}_{\tilde{B}A} = (\mathcal{S}_{B\tilde{A}})^T. \quad (4.8)$$

In case of monomodal port waveguides, this simplifies to

$$\mathcal{S}_{\tilde{B}A} = \mathcal{S}_{B\tilde{A}}, \quad (4.9)$$

which means that, irrespective of different separation distances, as long as there is a symmetry with respect to the $z = 0$ plane, the output power at port $\tilde{\mathbf{B}}$ for unit power input at port \mathbf{A} and no input at port $\tilde{\mathbf{A}}$ is exactly the same as the power observed at port \mathbf{B} for unit power input at port $\tilde{\mathbf{A}}$ and no input at port \mathbf{A} .

In Section 4.5.3 we show that the numerical implementation respects these abstract constraints.

4.3 Spectrum evaluation

A quantitative evaluation of the present microresonator model requires the propagation constants of the cavity modes γ_{bp} , hidden in \mathbf{G} , $\tilde{\mathbf{G}}$, and the scattering matrices \mathbf{S} , $\tilde{\mathbf{S}}$ of couplers (I) and (II). Once these quantities are available, the optical transmission through the resonator is given by equations (4.3).

In principle the spectral response of the device can be obtained by repeating the entire solution procedure for different wavelengths in an interesting range. That direct approach requires repeated computations of the bend propagation constants and the scattering matrices. A large part of the numerical effort can be avoided, if one calculates the relevant quantities merely for a few distant wavelengths, and then uses complex interpolations of these values for the actual spectrum evaluation. The interpolation procedure, however, should be applied to quantities that vary but slowly with the wavelength.

In line with the reasoning concerning the resonances in Section 1.4.3, one can expect that any rapid wavelength dependence of the transmission is determined mainly by the phase gain of the waves circulating in the cavity. Rapid changes in these phase relations are due to a comparably slow wavelength dependence of the bend propagation constants γ_{bp} , that is multiplied by the lengths L , \tilde{L} of the external cavity segments. If a substantial part of the cavity is already contained in the coupler regions, then the elements of the scattering matrices \mathbf{S} exhibit also fast phase oscillations with the wavelength, as depicted in Figure 3.7, such that \mathbf{S} directly is not suitable for the interpolation. Apart from these rapid changes, which can be attributed to the unperturbed propagation of the basis modes along the bent and straight waveguides, the interaction between the waves in the two coupled cores introduces an additional wavelength dependence, which in turn can be expected to be slow.

To separate the two scales of wavelength dependence in \mathbf{S} , one divides by the exponentials that correspond to the undisturbed wave propagation of the bend and straight modes towards and from the symmetry plane $z = 0$:

$$\mathbf{S}' = \mathbf{Q}^0 \mathbf{S} (\mathbf{P}^0)^{-1} \quad (4.10)$$

Here \mathbf{P}^0 and \mathbf{Q}^0 are diagonal matrices with entries $P_{j,j}^0$ and $Q_{j,j}^0$ as defined for \mathbf{P} and \mathbf{Q} in equation (3.20). Formally, one can view \mathbf{S}' as the scattering matrix of a coupler with zero length, where the interaction takes place instantaneously at $z = 0$. This modification of \mathbf{S} , applied analogously to $\tilde{\mathbf{S}}$, is compensated by redefining the lengths of the external cavity segments as $L' = \tilde{L}' = \pi R$, by changing the

matrices \mathbf{G} and $\tilde{\mathbf{G}}$ accordingly, and, where necessary, by taking into account the altered phase relations on the external straight segments.

After these modifications, the new matrices \mathbf{G}' and $\tilde{\mathbf{G}}'$ capture the phase gain of the cavity field along the full circumference. The modified scattering matrices \mathbf{S}' and $\tilde{\mathbf{S}}'$ show only a slow wavelength dependence (see Figure 4.4), such that the interpolation can be successfully applied to these matrices and to the bend propagation constants in \mathbf{G}' and $\tilde{\mathbf{G}}'$. The resonant features of the device are now entirely effected by the analytical relations (4.3), such that one obtains an excellent agreement between the transmission spectra computed with the interpolated quantities and the direct calculation, while the computational effort is significantly reduced.

4.4 Simulation results

In this section we summarize a series of numerical examples for the theory outlined in Sections 4.1, and 4.3, based on analytical bent modes (Chapter 2) and the CMT coupler model (Chapter 3).

The results of the CMT approach are compared with Finite Difference Time Domain (FDTD) simulations [55]. We apply an own implementation [95, 57] based on a simple second order Yee scheme [94]. Perfectly Matched Layer (PML) boundary conditions enclose the rectangular computational window, where fields are excited using the total-field / scattered field formulation. In order to generate reference signals for purposes of normalization, all FDTD calculations are carried out twice, once for the entire microresonator structure, then for one of the constituent straight waveguides only. To evaluate the spectral throughput- and dropped power, the time evolutions of the fields at suitable cross section lines through the respective ports are Fourier transformed, then projected onto the outgoing frequency domain mode profiles associated with the port. The ratio of the absolute values of these spectral signals (calculation for the microresonator structure / reference calculation) forms an approximation for the normalized output powers.

For a comparison with literature results, we consider structures as in Ref. [56], where microring/microdisk with high index contrast and very small radius resonators are calculated by 2-D FDTD with PML boundary conditions.

4.4.1 Microring resonator

For all subsequent computations of microresonator spectra, unless stated explicitly, we restrict ourselves to symmetric structures ($g = \tilde{g}$) with identical monomodal

straight waveguides. In line with the assumptions leading to equations (4.3), (4.4), the fundamental mode of the bus waveguides is launched at the In-port with unit power; there is no incoming field at the Add-port.

Figure 4.2 shows the spectral response for a microring-resonator made of two couplers as considered in Section 3.4.1, with cavity radius $R = 5 \mu\text{m}$ and gaps $g = \tilde{g} = 0.2 \mu\text{m}$. The CMT calculations use the computational setting as introduced for Figure 3.3. One observes the familiar ringresonator resonance pattern with dips in the transmitted power and peaks in the dropped intensity. According to Figure 3.4, the present parameter set specifies configurations with rather strong interaction in the coupler regions ($|S_{b0,s0}|^2 = 30\%$ (TE), $|S_{b0,s0}|^2 = 54\%$ (TM)), such that the resonances are relatively wide, with a substantial amount of optical power being directly transferred to the Drop port also in off resonant states. These properties are related to the attenuation of the cavity modes, and to the interaction strength in the coupler regions, i.e. to the radial confinement of the bend fields, hence one finds resonances of lower quality for TM polarization, and a decrease in quality with growing wavelength for both TE and TM polarized light.

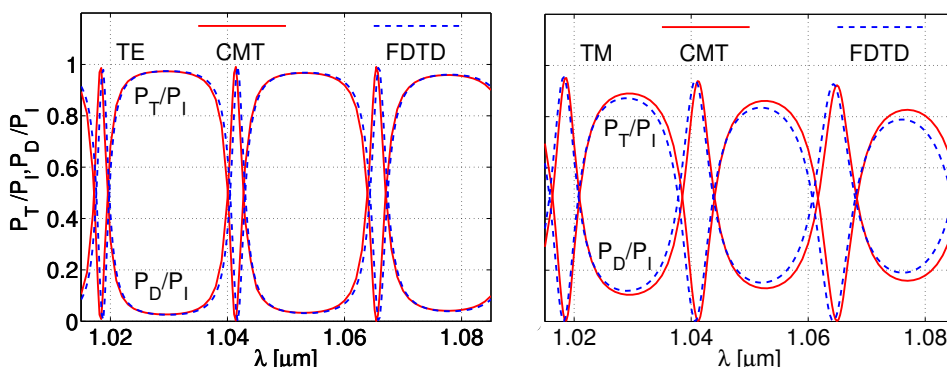


Figure 4.2: Relative transmitted P_T and dropped power P_D versus the vacuum wavelength for a ringresonator according to Figure 4.1, with parameters $n_c = n_s = 1.5$, $n_b = 1.0$, $w_c = 0.5 \mu\text{m}$, $w_s = 0.4 \mu\text{m}$, $R = 5 \mu\text{m}$, $g = \tilde{g} = 0.2 \mu\text{m}$; CMT and FDTD results for TE (left) and TM polarization (right).

The CMT results are compared with FDTD simulations, where a computational window that encloses the entire resonator device has been discretized by a rectangular grid of 1200×1220 points along the x - and z -directions with uniform mesh size of $0.0125 \mu\text{m}$. The boundaries of the computational window are enclosed by $0.4 \mu\text{m}$ wide perfectly matched layers with quadratically varying strength, which provide a reflectivity of 10^{-6} for the central wavelength $\lambda = 1.05 \mu\text{m}$. The simulations are carried out over a time interval of 13.1 ps with a step size of 0.025 fs .

According to the left and right plots of Figure 4.2, we find an excellent agreement between the CMT and the FDTD results for TE polarization, and only minor deviations for the TM case with less regular fields, more pronounced radiation, and stronger interaction in the coupler regions, where apparently the assumptions underlying the CMT approach are less well satisfied. Note that already in the present 2-D setting these FDTD calculations typically require a computation time of several hours, while the CMT analysis (with interpolation) predicts the entire spectrum in just a few minutes.

Interpolated spectrum evaluation

Now we look at the faster spectrum evaluation technique outlined in Section 4.3. For the bent-straight waveguide couplers involved in the ringresonator of Figure 4.2, the wavelength dependence of the “original” scattering matrix entries $S_{v,w}$ is depicted in Figure 3.6 (absolute square) and Figure 3.7 (real and imaginary part). By extracting phase gains for propagation along the coupler length, one obtains a “modified” scattering matrix S' (4.10). The wavelength dependence of $S'_{v,w}$ is shown in Figures 4.3, 4.4.

As the bend modes in the present coupler are not that lossy (see Figure 3.2), the plots of the absolute square of $S'_{v,w}$ in Figure 4.3 do not differ much from $S_{v,w}$ in Figure 3.6, although for the TM modes one can observe a slight change. But the plots of the real and imaginary parts of $S'_{v,w}$ clearly bring forward the essence of the discussion in Section 4.3. While the corresponding plots in Figure 3.7 show considerable oscillations, the curves in Figure 4.4 are almost linear such that $S'_{v,w}$ can be reliably interpolated.

The left side plots of Figure 4.5 shows the resonator spectrum as obtained by interpolating bend mode propagation constants and CMT scattering matrices for only two (linear interpolation) or three different wavelengths (quadratic interpolation), according to Section 4.3. While small deviations remain for the linear approximation, on the scale of the figure the curves related to quadratic interpolation are hardly distinguishable from the direct CMT results. Thus the interpolation approach provides a very effective means to predict the resonator spectrum, in particular if narrow dips /peaks in the responses of high-quality resonators would have to be resolved.

In Section 1.4.3 we discussed an approximate spectrum evaluation method, where one assumes that for a narrow wavelength interval the scattering matrices are approximately constant, and the resonances are “exclusively” due to the phase gains experienced by the cavity modes while propagating along the cavity. By using the

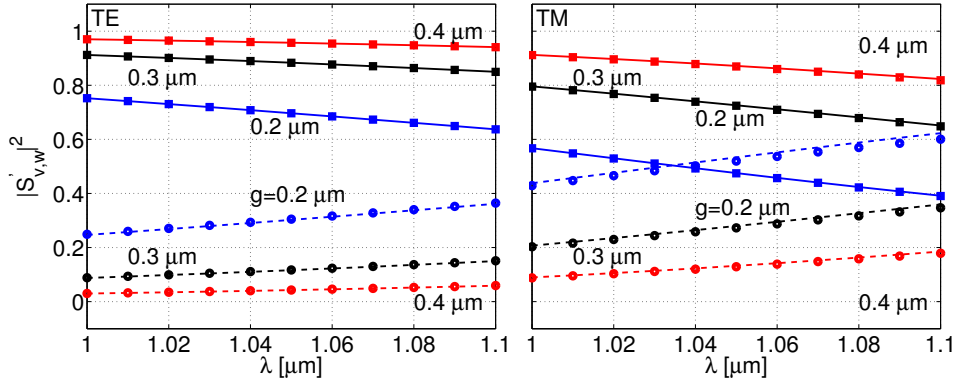


Figure 4.3: Wavelength dependence of the absolute square of the entries of the scattering matrix S' . The coupler configuration and the interpretation of the curves are identical to Figure 3.6.

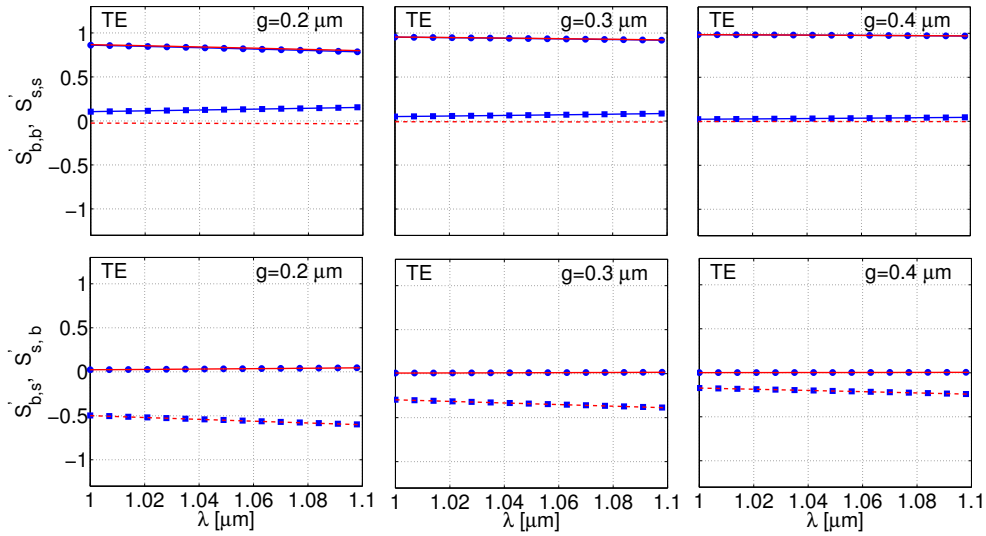


Figure 4.4: Wavelength dependence of the complex valued entries of the scattering matrix S' . For the coupler configuration and the interpretation of the curves, refer to Figure 3.7.

scattering matrices S' and \tilde{S}' (corresponding to a total cavity length of $2\pi R$), we can verify this approximation. In fact according to the right part of Figure 4.5, this scenario is quite well realized. For the present configuration with a low loss cavity mode, the spectrum evaluated with S' , \tilde{S}' at $\lambda = 1.05 \mu\text{m}$ and a wavelength dependent propagation constant γ_{b0} agrees quite well with “direct” CMT calculations. Note that, far from the reference wavelength $\lambda = 1.05 \mu\text{m}$, the approximation of

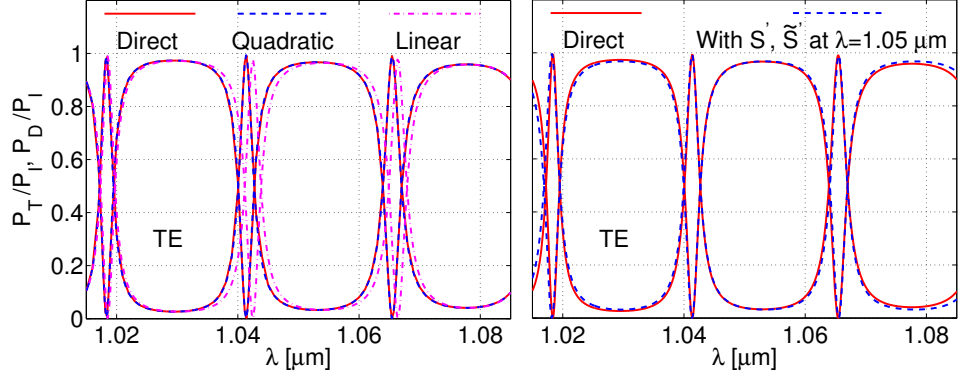


Figure 4.5: Left: CMT results, where the spectrum has been evaluated directly and by interpolation of CMT computations for nodal wavelengths $1.015 \mu\text{m}$ and $1.085 \mu\text{m}$ (linear), or $1.015 \mu\text{m}$, $1.05 \mu\text{m}$, and $1.085 \mu\text{m}$ (quadratic interpolation). Right: Comparison of spectra computed with the approximation of constant coupler scattering matrices as discussed in Section 1.4.3 and computed with direct CMT calculations. The microresonator setting is as in Figure 4.2.

constant matrices S' , \tilde{S}' slightly deteriorates.

Beyond modal amplitudes and power levels, the CMT solutions permit to access the full optical electromagnetic field. Figure 4.6 collects plots of the principal components for off resonance and resonant configurations for both polarizations. Off resonance, one observes the large Through transmission, small amplitudes of the waves in the Drop-port, and also only minor wave amplitudes in the cavity. At the resonances, the straight transmission is almost completely suppressed; the major part of the input power arrives at the Drop-port. For the present strongly coupled configurations, the power that enters and leaves the cavity at the two couplers leads to considerably different field intensities in the left and right halves of the ring. Here the radiative parts of the bend modes are appreciable outside the cavity, in particular for the more lossy TM waves.

4.4.2 Microdisk resonator

We now consider the symmetrical microdisk resonator that is constituted by two of the multimode couplers discussed in Section 3.4.2. The computational setting and all parameters are identical to the data given in Section 3.4.2, for gap widths $g = \tilde{g} = 0.2 \mu\text{m}$. The CMT description represents the optical field in the cavity as a superposition of the whispering gallery modes of Figure 3.8, where in principle

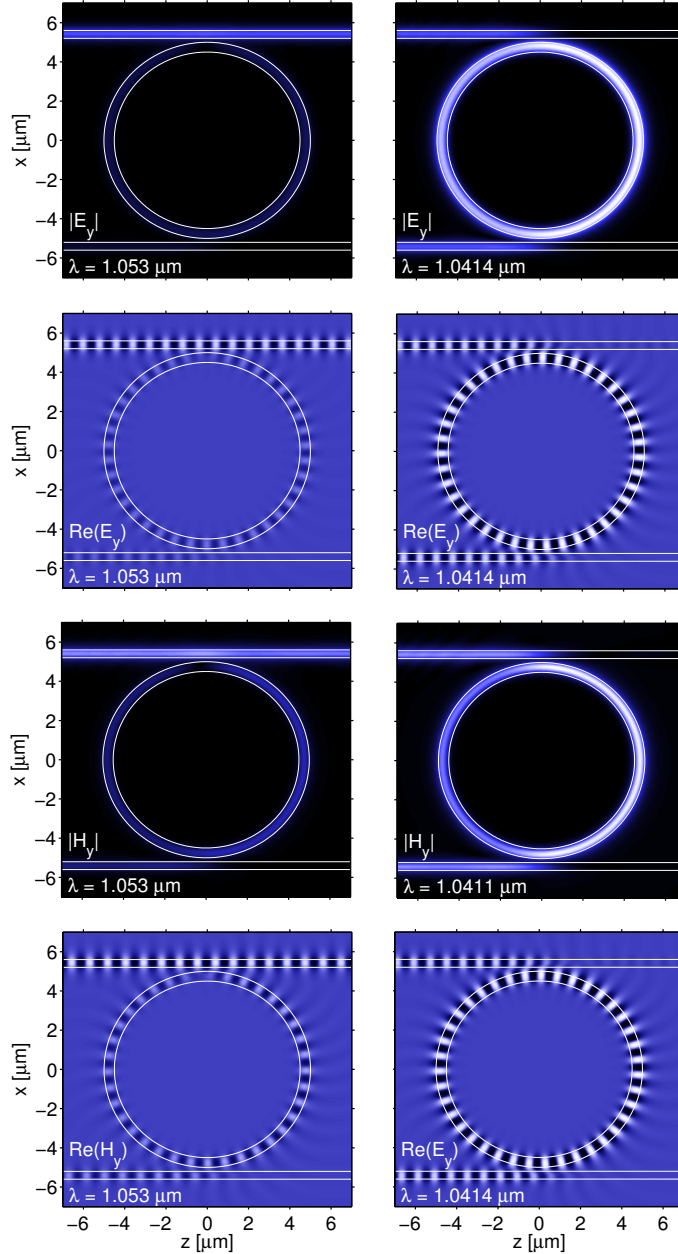


Figure 4.6: CMT results for the microring structure of Figure 4.2, local intensities (first and third row) and snapshots of the physical field (second and fourth row) of the principal components of TE (E_y) (first and second row) and TM (H_y) (third and fourth row) polarized waves, for an off-resonance wavelength (first column) and at a resonance (second column). For visualization purposes the coupler computational window has been extended to $[z_i, z_o] = [-4, 8] \mu\text{m}$.

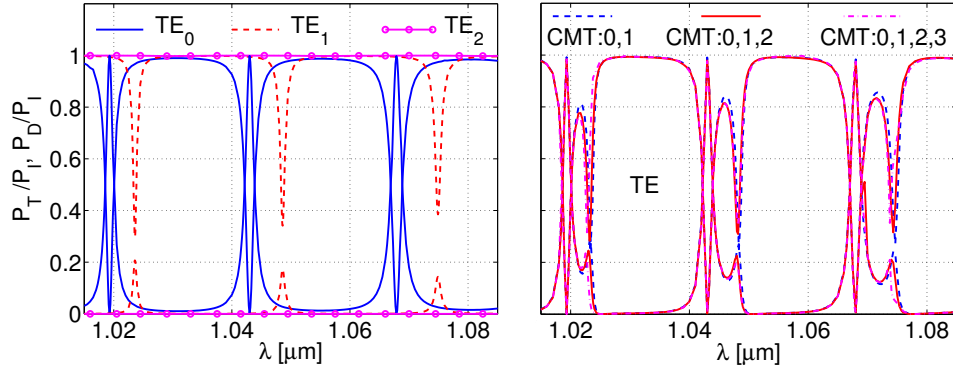


Figure 4.7: *TE* power spectrum of the microdisk resonator of Section 4.4.2. CMT analysis with different sets of basis modes; besides the mode of the straight waveguide, only one bend field (TE_0 , TE_1 , TE_2 , left), or the two, three, or four lowest order whispering gallery modes (right) are taken into account.

one must expect that more or less pronounced features related to all of these basis fields appear in the resonator spectrum. Figure 4.7 allows to investigate the significance of the individual cavity modes on the spectral response predicted by the CMT analysis.

The plots of Figure 4.7 show the spectral response as obtained by CMT computations where, besides the mode of the straight waveguide, different sets of bend modes are used as basis fields. The curves related to calculations with single cavity modes (left) exhibit only specific extrema of the full spectrum with similar extremal levels; obviously these resonances can be assigned to the respective (TE_0 or TE_1) whispering gallery mode. As these modes circulate along the cavity with their different propagation constants, individual resonance conditions are satisfied in general at different wavelengths. Apparently the regime discussed at the end of Section 4.1 is realized here (cf. also the tiny bend mode cross coupling coefficients $|S_{b_0, b_i}|^2$ in Figure 3.11).

While the fundamental and first order bend mode are essential for the present resonator, inclusion of the second order whispering gallery mode into the CMT analysis leads only to minor, the third order bend field to no visible changes of the curves in the right plot of Figure 4.7. Thus for this microdisk configuration it is sufficient to take into account the three lowest order cavity modes as basis fields to predict reliably the spectral response.

The left plot of Figure 4.8 allows to validate the interpolation approach of Sec-

tion 4.3 for the spectrum evaluation; just as in Section 4.4.1 one finds that the quadratic interpolation of the scattering matrix coefficients and propagation constants leads to curves that are almost indistinguishable from the directly computed results. The spectrum computed with the approximation technique of Section 1.4.3 is shown in the plots on right side Figure 4.8. Using constant scattering matrices S' , \tilde{S}' evaluated at $\lambda = 1.05 \mu\text{m}$ along with the wavelength dependent cavity mode propagation constants, computed spectrum (dashed line) agrees quite well with the strictly wavelength dependent calculations (solid line). On the scale of the figure, the locations of the resonances predicted by this approximation match with those corresponding to the “direct” calculations; but away from the reference wavelength $\lambda = 1.05 \mu\text{m}$, the TE_1 extrema levels differ slightly. Anyway, here one can accept the line of arguments in Section 1.4.3 as a very good approximation.

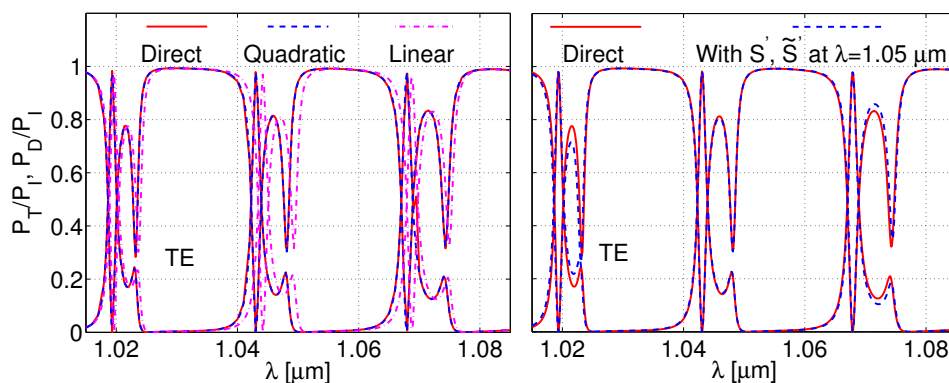


Figure 4.8: Left: CMT spectra (four basis modes) for the resonator setting as in Figure 4.7 computed directly, and by interpolation of data evaluated at the nodal wavelengths $1.015 \mu\text{m}$, $1.085 \mu\text{m}$ (linear) or $1.015 \mu\text{m}$, $1.05 \mu\text{m}$, $1.085 \mu\text{m}$ (quadratic interpolation). Right: Spectrum computed with direct CMT calculations (solid line) and with the approximation technique in Section 1.4.3 (dashed line).

Figure 4.9 compares the CMT spectra for TE and TM polarized light with rigorous FDTD calculations, where the simulation parameters are identical to those given in Section 4.4.1. There is a quite satisfactory agreement; as before minor deviations occur for the configurations with highly radiative, strongly interacting, and less regular fields in the TM case. The computational effort required for the CMT analysis is about two orders of magnitude lower than the effort required for the FDTD simulations.

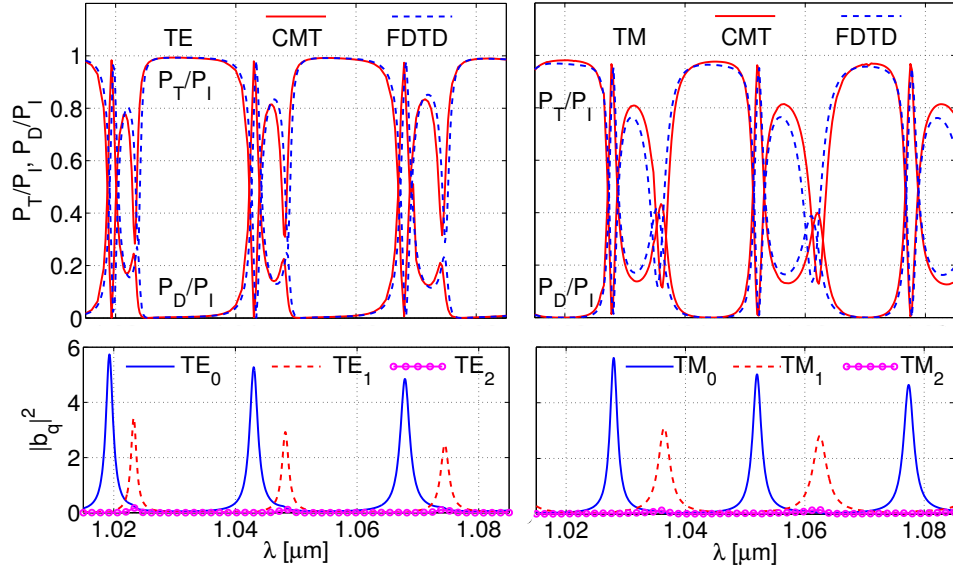


Figure 4.9: Power transmission through the microdisk resonator of Section 4.4.2, CMT and FDTD spectra (top) for TE (left) and TM polarized modes (right). The plots in the second row show the wavelength dependence of the amplitudes $|b_q|^2$ of the whispering gallery modes inside the cavity at port b (see Figure 4.1).

As an alternative to the computations of Figure 4.7, the inspection of the amplitudes of the basis modes that establish inside the cavity for varying wavelength provides a direct means for labeling the spectral features. The plots in the second row of Figure 4.9 identify the narrower, most pronounced resonances as belonging to the fundamental cavity modes, while the wider, less pronounced peaks are due to the first order whispering gallery fields.

Figure 4.10 gives an impression of the field distributions that accompany the resonance phenomena. Off resonance, most of the input power is directly transferred to the Through-port. At the wavelength corresponding to the minor resonance, the field pattern in the cavity exhibits a nearly circular nodal line that corresponds to the radial minimum in the profile of the first order whispering gallery mode (cf. Figure 3.8). According to Figure 4.9, here the first order mode carries most of the power inside the cavity. The deviation from the circular pattern is caused by the interference with the fundamental bend mode, which is also excited at this wavelength with a small power fraction. The major resonance related to the fundamental mode is of higher quality, with much larger intensity in the cavity, almost full sup-

pression of the waves in the Through-port and nearly complete drop of the input power.

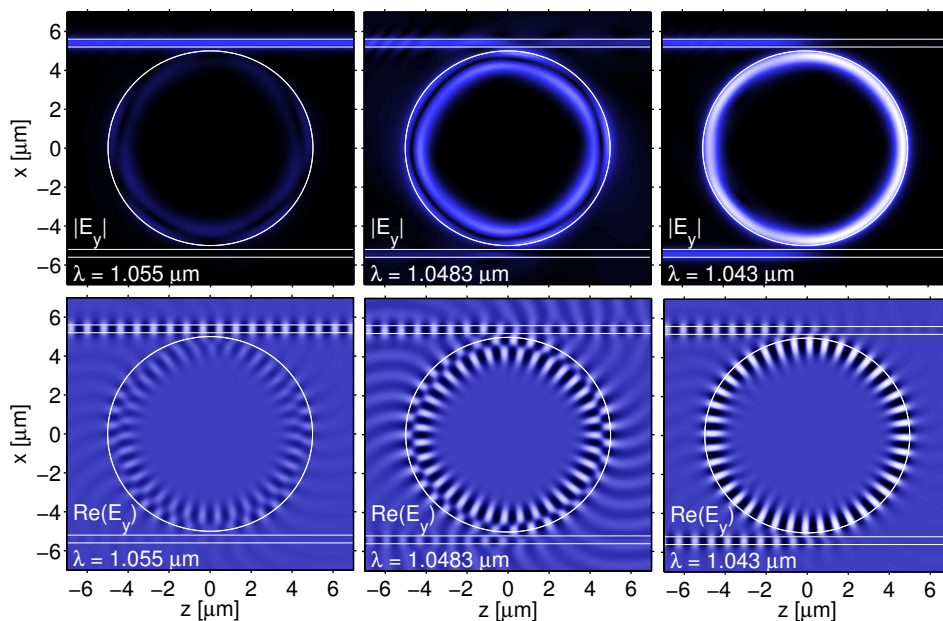


Figure 4.10: Field examples for the microdisk resonator of Section 4.4.2, CMT simulations with four basis modes, absolute value $|E_y|$ of the principal component of the TE fields (top), and snapshots of the real physical electric field (bottom). The wavelengths correspond to an off-resonance configuration (left) and to minor (center) and major resonances (right). The color scale levels of the plots in each row are comparable.

4.4.3 Compact high contrast cavities

Now we compare CMT simulations with FDTD results for microring resonators with high index contrast and extremely small radius as presented in Ref. [56]. A ring cavity of radius $R = 2.5 \mu\text{m}$ is coupled to straight waveguides. The cavity and the straight waveguides have a core of width $w_c = w_s = 0.3 \mu\text{m}$, and refractive index $n_c = n_s = 3.2$, the background refractive index is $n_b = 1$, and the separation distance is $g = \tilde{g} = 0.232 \mu\text{m}$. The fundamental mode of the In-port straight waveguide is launched with unit power. The response of this resonator is scanned over a wavelength range $[1.42, 1.62] \mu\text{m}$.

CMT calculations are carried out over a computational window $(x_1, z_1) = (0, -2) \mu\text{m}$, $(x_r, z_0) = (8, 2) \mu\text{m}$ with stepsizes $h_x = 0.001 \mu\text{m}$, $h_z = 0.1 \mu\text{m}$. For the spectrum evaluation, quadratic interpolation is used with nodal wavelengths $\lambda = 1.42 \mu\text{m}$, $1.52 \mu\text{m}$, $1.62 \mu\text{m}$. At these nodal wavelengths, as shown in Table 4.1, the straight waveguides are bimodal and the bent waveguide (ring segment) is “monomodal” (i.e. the bend does not support other modal fields with reasonably low attenuation).

$\lambda [\mu\text{m}]$	β/k Straight waveguide		γ/k Bent waveguide
	TE ₀	TE ₁	TE ₀
1.42	2.7959	1.4133	2.6332 - i 0
1.52	2.7572	1.2578	2.5964 - i 0
1.62	2.7186	1.1268	2.5598 - i 0

Table 4.1: Effective refractive indices of the modes of the straight waveguides and bent waveguide for the ringresonator of Section 4.4.3. Due to the high refractive index contrast, the bend modes have negligible losses.

The resultant spectral response of the ringresonator is shown in Figure 4.11. Even though the straight waveguides are bimodal, due to the “phase matching” condition (see the values in Table 4.1), practically no power is coupled to the TE₁ straight waveguide mode. In good qualitative agreement with Ref. [56], the plots represent the output powers for the fundamental TE mode of the straight waveguide. The left plot of Figure 4.11 shows sharp resonances of the transmitted power, whereas the plot on the right side magnifies the resonance features at $\lambda_{\text{res}} = 1.5596 \mu\text{m}$. At this resonance wavelength, the CMT simulations predict a full width at half maximum (FWHM) $2\delta\lambda \approx 0.3 \text{ nm}$, a quality factor $Q \approx 5200$, while Ref. [56] quotes $2\delta\lambda \approx 0.3 \text{ nm}$, $Q \approx 5000$.

A comparison of the resonance wavelengths obtained by the CMT simulations and the results of Ref. [56] is shown in Table 4.2. On the micron scale these results agree up to the second decimal place. For applications, where the positions of the resonance wavelengths on a large wavelength range (as e.g. in the left plot of Figure 4.11) is relevant, one can consider the difference relative to the free spectral range (FSR), i.e. look at the expression $|\lambda_{\text{res}}^{\text{CMT}} - \lambda_{\text{res}}^{\text{FDTD}}|/\text{FSR}$. For the TE₀ resonance at $\lambda_{\text{res}}^{\text{CMT}} = 1.5596 \mu\text{m}$, one obtains a small deviation of about 6%; in this respect, we find a reasonable agreement between FDTD and CMT simulations. On the other hand, for applications that involve a fine sampling of wavelengths, one might be interested in the deviation relative to the resonance width (FWHM), given by $|\lambda_{\text{res}}^{\text{CMT}} - \lambda_{\text{res}}^{\text{FDTD}}|/\text{FWHM}$. This leads to a deviation of about 930%, i.e. the computational values for the resonance positions become meaningless in this

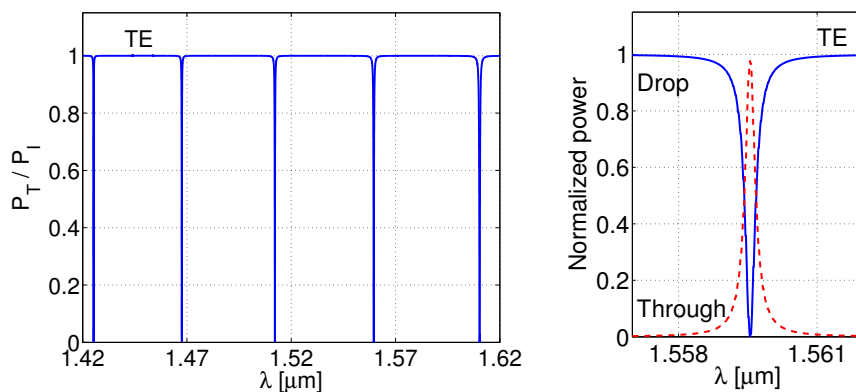


Figure 4.11: Left: CMT Spectral response of the microring resonator of Section 4.4.3. Right: Resonance feature at $\lambda_{\text{res}} = 1.5596 \mu\text{m}$. At this wavelength, almost 98% of the input power is dropped.

respect.

Note that for the present configuration, it is difficult to access the reliability of the CMT or the FDTD approach. The corresponding ring resonator with the high refractive index contrast represents an extreme configuration for the CMT approach. Also, the FDTD computations are seriously constrained by inherent numerical dispersion. Therefore we do not attempt a statement about which of the simulations corresponds to physical reality, what concerns the precise resonance positions.

	$\lambda_{\text{res}} [\mu\text{m}]$				
Ref. [56]	1.4252	1.4675	1.5122	1.5624	1.6103
Present	1.4280	1.4715	1.5149	1.5596	1.6131

Table 4.2: Comparison of resonance wavelengths for the ringresonator in Section 4.4.3 computed with FDTD (Ref. [56]) and CMT (present).

By filling the interior of the ring waveguide in Section 4.4.3 with the core material, one obtains a microdisk resonator. For this structure, we now compare CMT results with Ref. [56]. As before, the TE_0 mode is excited at the In-port, the spectral response is computed with quadratic interpolation at nodal wavelengths $\lambda = 1.42 \mu\text{m}, 1.52 \mu\text{m}, 1.62 \mu\text{m}$. For the present setting, apart from the straight waveguide modes, the first three lower order cavity modes are sufficient as basis fields. Table 4.3 gives their effective refractive indices at the nodal wavelengths.

λ [μm]	γ/k TE ₀	γ/k TE ₁	γ/k TE ₂
1.42	2.7482 - i 0	2.3435 - i 0	2.0153 - i 6.4147 · 10 ⁻¹¹
1.52	2.7298 - i 0	2.3067 - i 0	1.9638 - i 1.0137 · 10 ⁻⁹
1.62	2.7119 - i 0	2.2709 - i 1.0878 · 10 ⁻¹²	1.9137 - i 1.0653 · 10 ⁻⁸

Table 4.3: Effective indices of the whispering gallery modes ($w_c = R$) of the disk with radius $R = 2.5 \mu\text{m}$, inner core refractive index $n_c = 3.2$, and external cladding refractive index $n_b = 1.0$.

As in the case of the corresponding microring configuration, again here most of the input power is coupled to only the TE₀ mode of the straight waveguides. The spectral response of this microdisk resonator is shown in Figure 4.12; we again find a reasonable qualitative agreement with Ref. [56]. As evident from the plot on the left side, for the present configuration, only the TE₀ and TE₁ cavity modes play a significant role. Details of the resonances are shown in the associated plots.

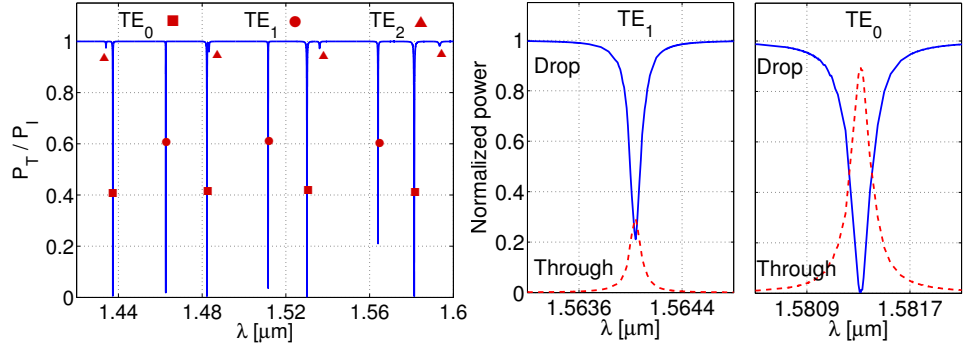


Figure 4.12: CMT Spectral response of the microdisk resonator (left plot) of Section 4.4.3 with $w_c = R$. The central plot shows the resonance of the TE₁ cavity mode with $\lambda_{\text{res}} = 1.5640 \mu\text{m}$, $2\delta\lambda \approx 0.1 \text{ nm}$, and $Q = 14000$, whereas the right plot shows that of the TE₀ cavity mode with $\lambda_{\text{res}} = 1.5813 \mu\text{m}$, $2\delta\lambda \approx 0.2 \text{ nm}$, and $Q = 7900$.

Note that these plots are obtained by quadratic interpolation of CMT results for scattering matrices S' and cavity segment propagation constants γ_{bp} at just three nodal wavelengths, whereas to resolve such sharp features with FDTD simulations, one has to do FDTD calculations over extremely large time intervals, which turns out to be demanding in terms of computational effort.

The corresponding comparison of resonant wavelengths computed with CMT simulations and values of Ref. [56] is given in Table 4.4. As in the case of the pre-

4. Influence of separation distance on the spectral response

viously discussed ring resonator, the remarks concerning the accuracy of the two simulation techniques with respect to the resonance positions apply to these results as well.

	TE ₀		TE ₁		TE ₂	
	Ref. [56]	Present	Ref. [56]	Present	Ref. [56]	Present
λ_{res} [μm]	1.4402	1.4373	1.4654	1.4626	-	1.4371
	1.4852	1.4823	1.5146	1.5115	1.4861	1.4833
	1.5332	1.5301	1.5672	1.5640	1.5390	1.5361
	1.5845	1.5813	-	-	1.5961	1.5935

Table 4.4: Comparison of resonance wavelengths for the microdisk resonator as considered in Section 4.4.3.

4.5 Influence of separation distance on the spectral response

In Section 3.4 we analyzed the effect of changes in the separation distance on the coupler performance. In this section, we investigate its influence on the spectral response of the entire resonators. Three types of changes of g and \tilde{g} are discussed viz. changing both separation distances identically, changing only one of the separation distances while keeping the other constant, and changing both separation distances with $g + \tilde{g} = \text{constant}$ (i.e. shifting the cavity between fixed port waveguides).

The simulations are carried out for the resonator configurations of Figure 4.5 (ring resonators) and Figure 4.8 (disk resonators), and the spectrum evaluation procedure by quadratic interpolation is employed.

4.5.1 Changing both separation distances identically

Figure 4.13 shows the effect of symmetrical changes of both separation distances on the spectral response. As evident from Figures 3.4, 3.11, as the distances g , \tilde{g} are reduced, the cross coupling between the straight waveguide and the cavity increases, and the self coupling decreases. Due to the reduced self coupling of the upper straight waveguide, the nonresonant level of throughput power decreases; whereas as more power is coupled from the upper waveguide to the cavity, and then from the cavity to the lower waveguide, the nonresonant level of drop power increases.

Due to the increased cavity self coupling ($|\mathbf{S}_{\text{bb}}|$), as seen from Eq. (1.15), the

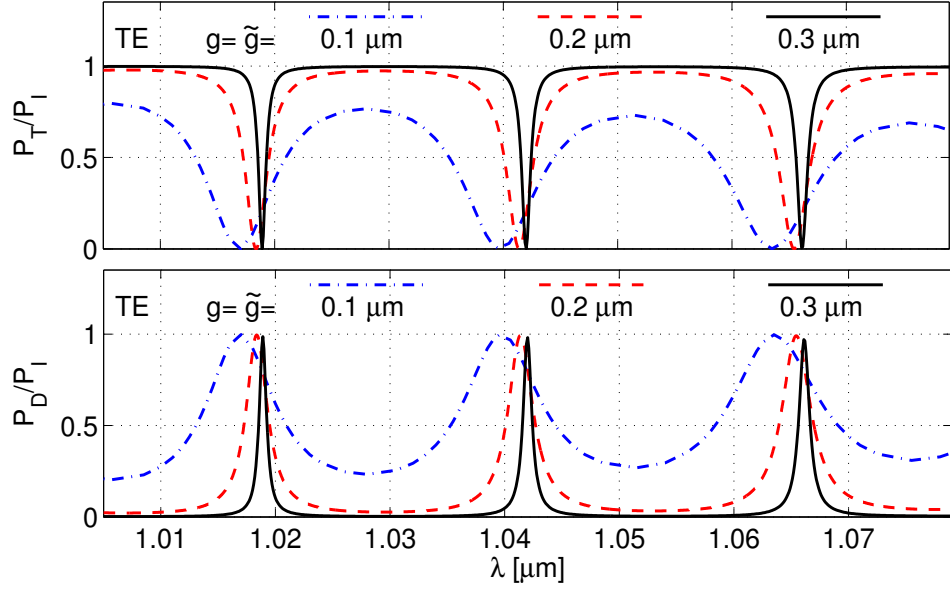


Figure 4.13: Spectral response of a ring resonator for different gap widths. The resonator configuration is as in Figure 4.5.

FWHM decreases. This is clearly revealed in plots of Figure 4.13. As shown in Table 4.5, there is also a change in the resonance positions, here defined as the wavelengths corresponding to the extrema in the transmitted and the dropped power.

$g = \tilde{g}$ [μm]	TE ₀ resonance wavelengths [μm]		
0.1	1.01700	1.03950	1.06350
0.2	1.01836	1.04138	1.06540
0.3	1.01890	1.04200	1.06606
0.4	1.01913	1.04227	1.06647
0.5	1.01924	1.04239	1.06661
0.6	1.01928	1.04245	1.06668
eigenfrequencies	1.01928	1.04248	1.06678

Table 4.5: Resonance positions of the ring resonator of Figure 4.5, for different separation distances $g = \tilde{g}$. For large separations, the resonance positions computed by the CMT based simulations tend to the eigenfrequencies of the “isolated” ring cavity [39, private communication].

For larger separation distances, the influence of neighboring straight waveguides on the cavity field propagation is marginal, and the resulting resonances of the microresonator (cavity coupled to two straight waveguides) tend to resonances of the “isolated” cavity. The comparison with resonance wavelengths of the isolated cavity obtained by the complex eigenfrequency model [39], shown in Table 4.5, confirms this fact.

The same trend is observed in case of a resonator with a disk cavity, see Figure 4.14 and Table 4.6. The disk resonance wavelengths will converge to the wavelength corresponding to the eigenfrequencies of the isolated disk (note that corresponding data for eigenfrequencies of the isolated disk was not available).

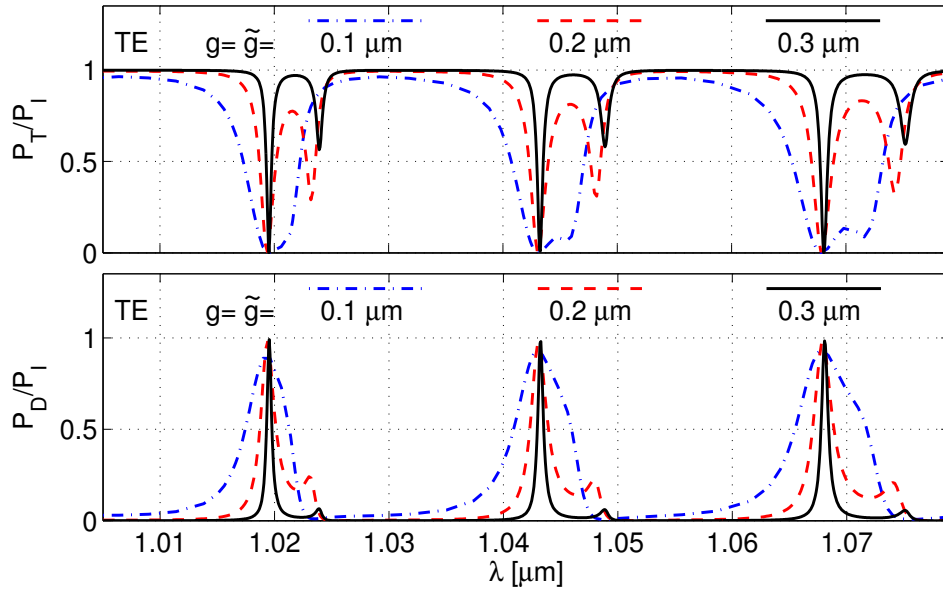


Figure 4.14: Spectral response of disk resonators as in Figure 4.8 with different coupler gaps. The plots show the resonances of the TE_0 mode (the pronounced extrema) and of the TE_1 mode (the secondary extrema). The CMT simulations involve the first three WGMs.

4.5.2 Changing only one of the separation distances

Figure 4.15 shows CMT simulation results for microring resonators for varying one of the gaps g or \tilde{g} , while keeping the other constant. Keeping the separation \tilde{g} constant, if g is reduced, then the coupling between the upper bus waveguide

$g = \tilde{g}$ [μm]	Resonance wavelengths [μm]					
	TE_0			TE_1		
0.1	1.01952	1.04311	1.06787	-	1.04559	1.07161
0.2	1.01937	1.04307	1.06790	1.02324	1.04813	1.07430
0.3	1.01953	1.04324	1.06809	1.02394	1.04893	1.07520
0.4	1.01962	1.04334	1.06820	1.02425	1.04928	1.07562
0.5	1.01966	1.04340	1.06826	1.02440	1.04946	1.07584
0.6	1.01969	1.04342	1.06829	1.02449	1.04957	1.07596

Table 4.6: Resonance positions of the disk resonator of Figure 4.8, for different separations $g = \tilde{g}$. Note that for $g = \tilde{g} = 0.1 \mu\text{m}$, the broad peaks related to the TE_0 and TE_1 resonances interfere strongly.

and the cavity increases. Due to reduced self coupling of the input waveguide, the nonresonant level of the through power decreases, as more power is coupled to the cavity, the nonresonant drop power increases. On the other hand, keeping the separation g constant, if \tilde{g} is reduced, then the coupling between the lower bus waveguide and the cavity increases. As more power is coupled from the cavity to the Drop-port waveguide, the nonresonant level of the drop power increases, whereas the nonresonant through power decreases.

For the simulations shown in Figure 4.15, changing the separation distance also affects the position of the resonances. In both cases, enlarging one of the separation distances, increases the resonance wavelength.

The simulation results of Figure 4.15 show a very peculiar behaviour for $g = \tilde{g}$, for which the resonant through power and drop power attain extrema. Figure 4.16 shows the variation of the resonant power transmission for different settings of the separation distances for the ring resonator. As evident from these plots, when both coupler gaps are identical, the drop power is maximum (≈ 1), and the through power is minimum (≈ 0). This can be explained as following.

In Section 1.4.3, we derived an expression for the drop power at resonance for a microresonator configuration with identical couplers ($g = \tilde{g}$). Generalizing that expression to non-identical couplers ($g \neq \tilde{g}$) gives

$$P_{\text{D}}|_{\text{res}} = P_1 \frac{|\tilde{\mathbf{S}}_{\text{sb}}|^2 |\mathbf{S}_{\text{bs}}|^2 e^{-\alpha(L + \tilde{L})}}{(1 - |\mathbf{S}_{\text{bb}}| |\tilde{\mathbf{S}}_{\text{bb}}| e^{-\alpha(L + \tilde{L})})^2}. \quad (4.11)$$

If the cavity mode under consideration has negligible attenuation ($\alpha \approx 0$), and if the coupling is assumed to be lossless (power is conserved, i.e. $|\mathbf{S}_{\text{bs}}|^2 = 1 - |\mathbf{S}_{\text{bb}}|^2$,

4. Influence of separation distance on the spectral response

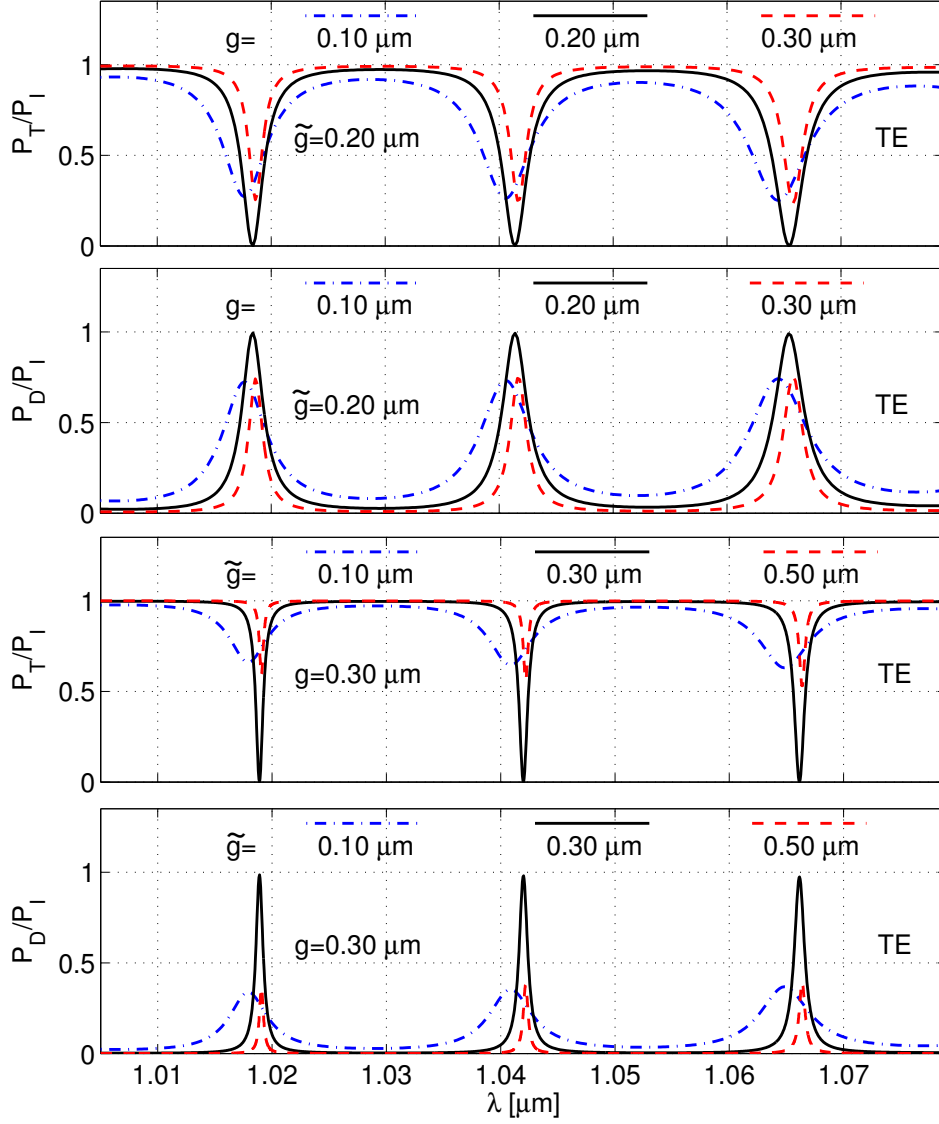


Figure 4.15: Effect of changing one of the separation distances on the spectrum response of the ring resonator. The first two plots show the response for different gaps g for a constant separation distance \tilde{g} ; for the two lower plots, g is kept fixed, while \tilde{g} varies (note the different values chosen in the upper and lower graphs).

$|\tilde{S}_{sb}|^2 = 1 - |\tilde{S}_{bb}|^2$, then

$$P_{D|res} = P_I \frac{(1 - |\tilde{S}_{bb}|^2)(1 - |S_{bb}|^2)}{(1 - |S_{bb}||\tilde{S}_{bb}|)^2}. \quad (4.12)$$

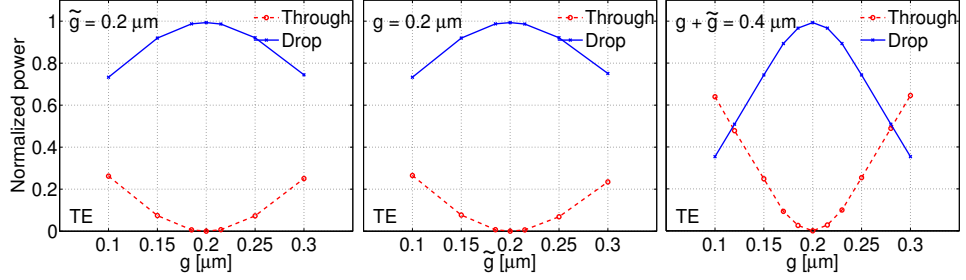


Figure 4.16: Resonant power transmission of a ring resonator for different coupler gaps. The plots show the through power and the drop power at the respective resonance wavelengths around $\lambda = 1.043 \mu\text{m}$ for $\tilde{g} = \text{constant}$ (left plot), $g = \text{constant}$ (middle plot) and $g + \tilde{g} = \text{constant}$ (right plot).

For $|\mathbf{S}_{bb}| = |\tilde{\mathbf{S}}_{bb}|$, this leads to $P_D = P_T$, i.e. complete transfer of the input power to the Drop-port. This implies $|\mathbf{S}_{ss}| = |\tilde{\mathbf{S}}_{ss}|$, $|\mathbf{S}_{bs}| = |\tilde{\mathbf{S}}_{bs}|$, $|\mathbf{S}_{sb}| = |\tilde{\mathbf{S}}_{sb}|$, which is realized for identical couplers ($g = \tilde{g}$), as illustrated in Figure 4.16.

If the attenuation losses are not negligible, then the ideal complete power transfer is not achieved. This becomes apparent for the simulation results of the disk resonator, shown in Figure 4.17. For the low loss TE_0 modes, the power drop is almost 1. But as the TE_1 mode has substantially higher attenuation (see Figure 3.8), the TE_1 resonance power drop for the symmetrical resonator is far from complete power transfer (also see Fig. 4.7).

Comparison of the first two plots of Figure 4.16 shows that for low loss case, g and \tilde{g} have almost identical effects on P_D , P_T at resonance. Moreover, the plots in Figure 4.15 and 4.17 reveal that as one of the gaps increases, the width of the resonance reduces.

4.5.3 Shifting the cavity between fixed bus waveguides

From the view point of realization of microresonators, it is useful to understand the effects of a displacement of the cavity with respect to the adjacent straight waveguides. This means, studying the effects of changing both separation distances, while keeping $g + \tilde{g} = \text{constant}$. Figure 4.18 shows corresponding simulation results for the previous ring resonator.

While for the off-resonance wavelengths there are hardly any differences, close to the resonance wavelengths, one can observe substantial changes. As seen from the right plot of Figure 4.16, for growing g with $g < \tilde{g}$, the through power steadily de-

4.5 Influence of separation distance on the spectral response

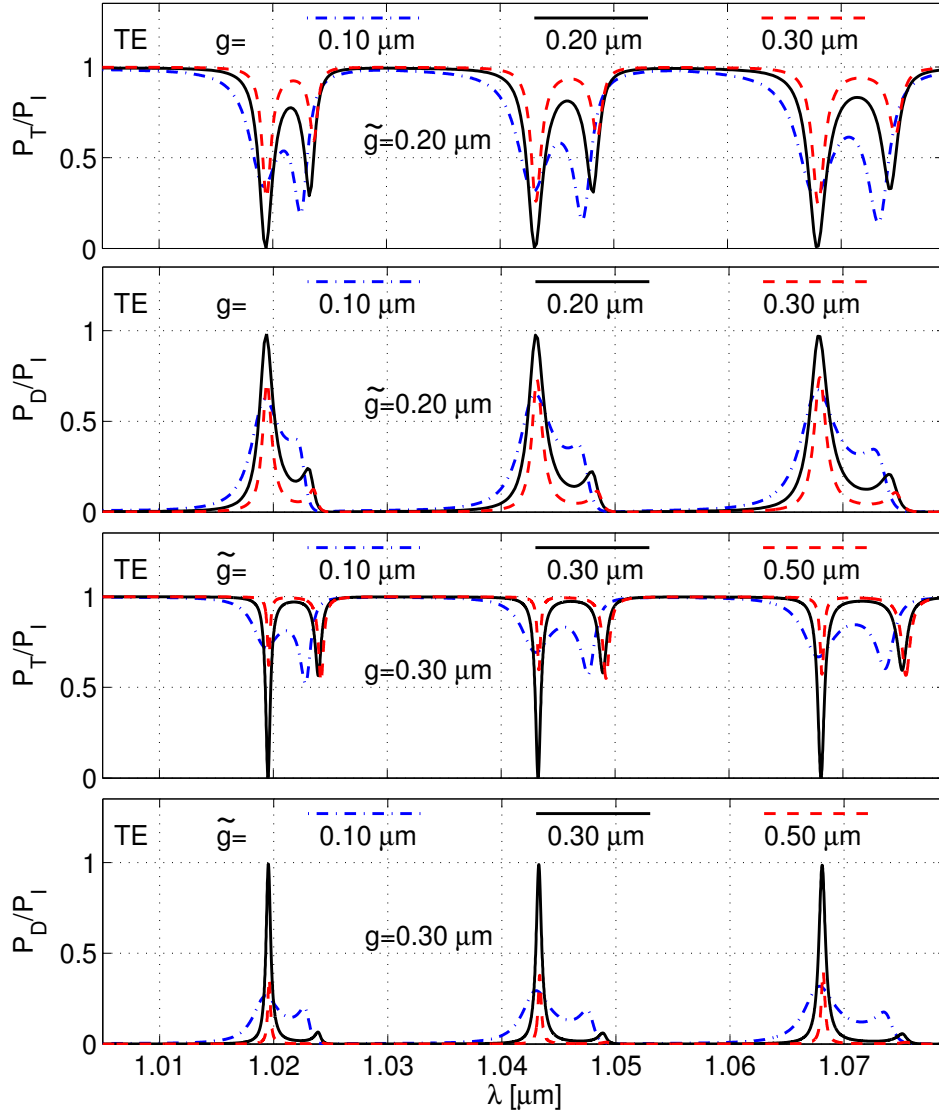


Figure 4.17: Effect of changing one of the gaps on the spectrum response of the disk resonator. The interpretation of the curves is the same as for Figure 4.15.

creases and the drop power steadily increases (also see Figure 4.18). As discussed before, for $g = \tilde{g}$, at resonance there is complete transfer of the input power to the drop port. For larger g with $g > \tilde{g}$, the reverse effect takes place, i.e. the through power steadily increases, and the drop power steadily decreases.

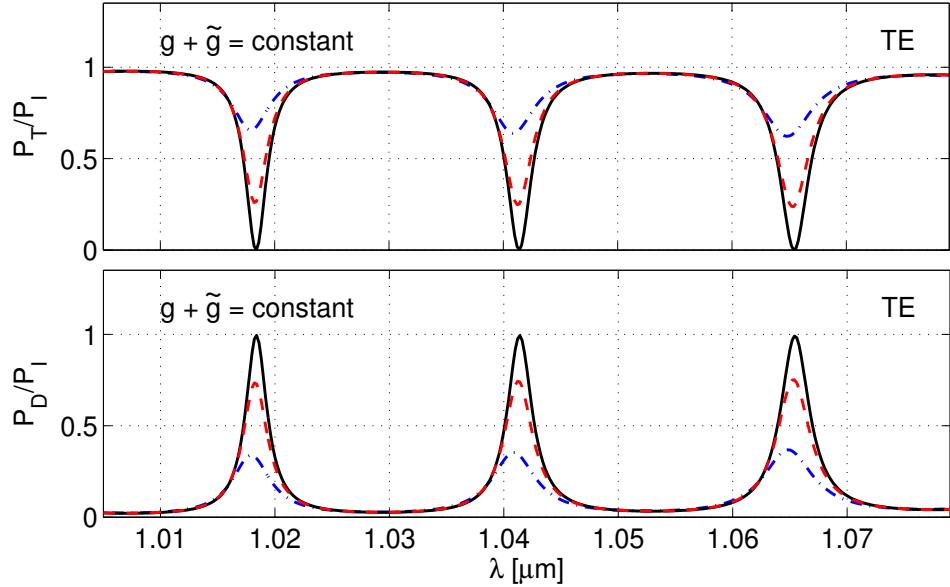


Figure 4.18: Spectral response of the ring resonator for shifting the cavity between fixed straight waveguides. For $g + \tilde{g} = 0.4 \mu\text{m}$, the plots show the through power (first row) and the drop power (second row) for ring resonators with $g = 0.10 \mu\text{m}$ and $\tilde{g} = 0.30 \mu\text{m}$ (dash-dotted line), $g = 0.15 \mu\text{m}$ and $\tilde{g} = 0.25 \mu\text{m}$ (dashed line), $g = 0.20 \mu\text{m}$ and $\tilde{g} = 0.20 \mu\text{m}$ (solid line).

For constant $g + \tilde{g}$, the simulations of Figure 4.18 systematically investigate the consequence of shifting the cavity closer to the lower straight waveguide. It will be equally interesting to investigate the effect of shifting the cavity closer to the upper (input) waveguide. For this, it is sufficient to know the influence of interchanging the separation distances g and \tilde{g} on the spectral response.

As an illustration, Figure 4.19 compares the ring resonator spectral response for $g = 0.25 \mu\text{m}$, $\tilde{g} = 0.15 \mu\text{m}$ and $g = 0.15 \mu\text{m}$, $\tilde{g} = 0.25 \mu\text{m}$. On the scale of the figure, the curves (solid line and dashed line) for the through power (first row) and the dropped power (second row) are almost indistinguishable. But when the difference between the two results is plotted (third row), one sees that power through for the setting $g = 0.25 \mu\text{m}$, $\tilde{g} = 0.15 \mu\text{m}$ is more than that for $g = 0.15 \mu\text{m}$, $\tilde{g} = 0.25 \mu\text{m}$, whereas the drop power is equal in both cases. The same behaviour is also observed in case of corresponding simulations for the disk resonator, which are shown in Figure 4.20. In that case, one can clearly distinguish the two through power curves around the resonances of the TE_1 mode. But in both cases, the

4.5 Influence of separation distance on the spectral response

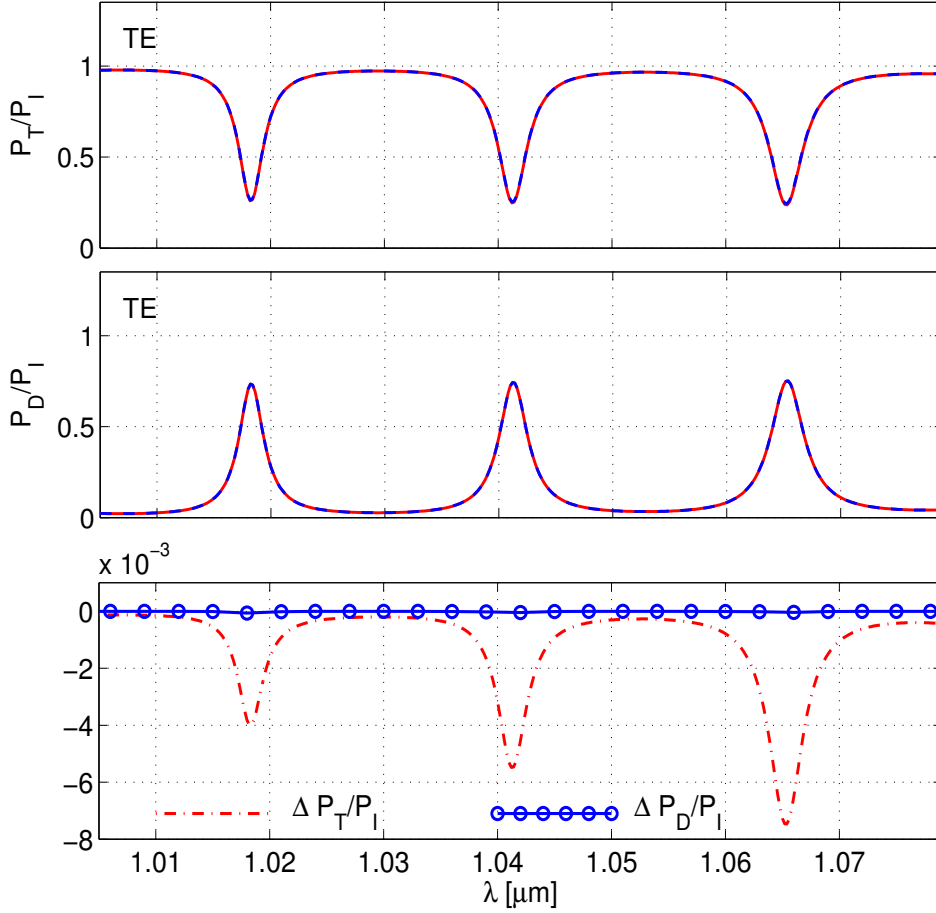


Figure 4.19: Power transmissions of the ring resonator for interchanging g and \tilde{g} . For $g + \tilde{g} = 0.4 \mu\text{m}$, the plots show the through power (top plot) and the dropped power (middle plot) for $g = 0.25 \mu\text{m}$, $\tilde{g} = 0.15 \mu\text{m}$ (dashed lines) and $g = 0.15 \mu\text{m}$, $\tilde{g} = 0.25 \mu\text{m}$ (solid lines), whereas the bottom plot shows the difference between the respective through powers (dash-dotted line), drop powers (circles) for the two settings. Note that the curves for P_D and –on the scale of the figure– also the curves for P_T are superimposed.

dropped power remains unchanged.

The invariance of the drop power for interchange of g and \tilde{g} can be explained by flipping the resonator along the z axis, and using $\mathcal{S}_{\tilde{B}A} = \mathcal{S}_{A\tilde{B}}$ from Eq. (4.6).

This can also be explained by using Eq. (4.9). For the resonator setting as in

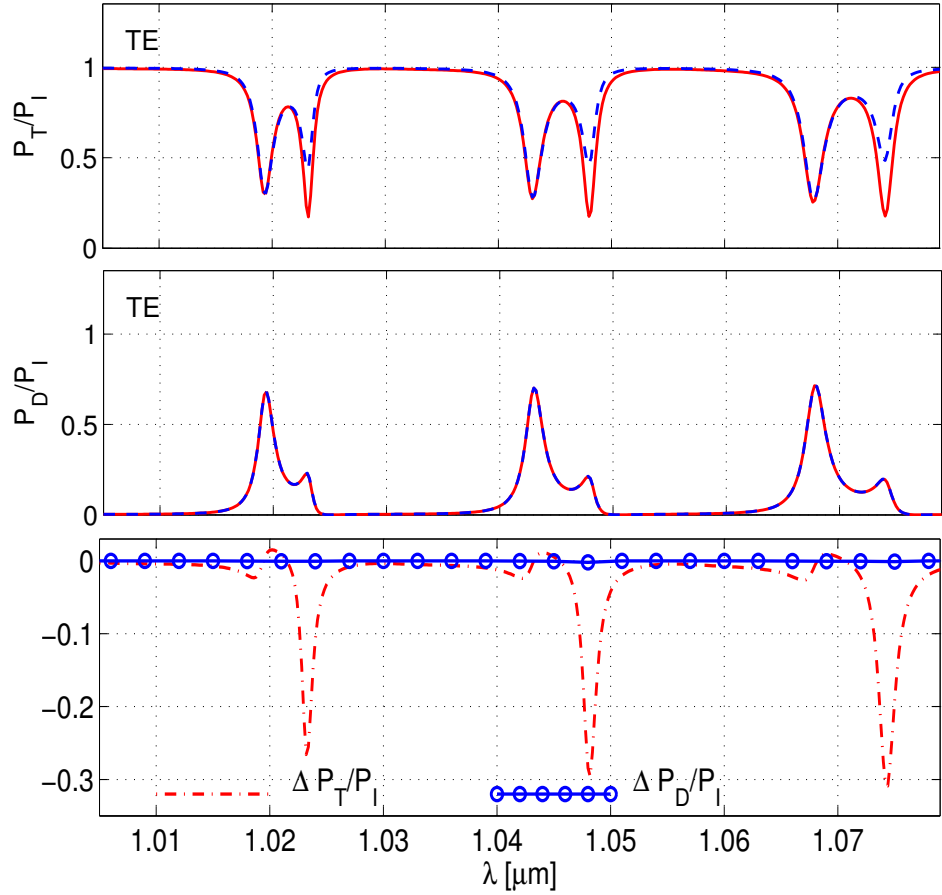


Figure 4.20: Power transmissions of the disk resonator for interchanging g and \tilde{g} with $g + \tilde{g} = 0.4 \mu\text{m}$. The interpretation of the curves is the same as for Figure 4.19.

Figure 4.1 (symmetrical around the plane $z = 0$), interchanging the separation distances g and \tilde{g} is equivalent to changing the setting with input at port A to a setting, where port \tilde{A} is excited.

According to Eq. (4.9), the power at port \tilde{B} for $P_I = 1$ and $P_A = 0$, which is the drop power with $g = 0.25 \mu\text{m}$, $\tilde{g} = 0.15 \mu\text{m}$, is the same as the power at port B for $P_I = 0$ and $P_A = 1$, which is the drop power with $g = 0.15 \mu\text{m}$, $\tilde{g} = 0.25 \mu\text{m}$. Hence the difference between the drop powers for the two settings (depicted by a line with circles in the bottom plot of Figures 4.19, 4.20) is zero.

What concerns the nonnegligible difference in the throughput power (dash-dotted

line in the last plots of Figure 4.19, 4.20, one can consider the “ideal” resonator discussed in context of Eq. (4.12). If the attenuation corresponding to the propagation along the cavity is negligible, i.e. $\alpha \approx 0$ for the cavity mode, and if the coupling is lossless, then for monomodal port waveguides, one has

$$|\mathcal{S}_{\text{BA}}|^2 + |\mathcal{S}_{\tilde{\text{B}}\tilde{\text{A}}}|^2 = 1, \quad \text{for } P_{\tilde{\text{I}}} = 1, P_{\text{A}} = 0, \quad (4.13)$$

$$|\mathcal{S}_{\tilde{\text{B}}\tilde{\text{A}}}|^2 + |\mathcal{S}_{\text{BA}}|^2 = 1, \quad \text{for } P_{\text{A}} = 1, P_{\tilde{\text{I}}} = 0. \quad (4.14)$$

From the Eq. (4.9), one has $\mathcal{S}_{\tilde{\text{B}}\tilde{\text{A}}} = \mathcal{S}_{\text{BA}}$, which leads to $|\mathcal{S}_{\text{BA}}|^2 = |\mathcal{S}_{\tilde{\text{B}}\tilde{\text{A}}}|^2$, i.e. for the low loss resonator, given input only at port A, the output power at port B is exactly the same as the output power at port $\tilde{\text{B}}$ for input given only at port $\tilde{\text{A}}$. Or in the other words, interchanging g and \tilde{g} does not affect the through power.

For the ring resonator in Figure 4.19, such an “ideal” situation is realized (see Figure 3.2, a well guided cavity mode, and Figure 3.4, almost lossless coupling). Therefore the difference in the throughput power for these simulations is quite small. As the wavelength increases, the attenuation of the cavity mode increases, resulting in corresponding growing deviation $\Delta P_{\text{T}}/P_{\tilde{\text{I}}}$. This can be clearly seen for the resonances of the TE_0 mode.

The simulations of the disk resonator in Figure 4.20, involve a substantially lossy TE_1 whispering gallery mode (see Figure 3.8). Here $|\mathcal{S}_{\text{BA}}|^2 \neq |\mathcal{S}_{\tilde{\text{B}}\tilde{\text{A}}}|^2$, which is evident from the significant difference of the through power P_{T} . Apart from the minor differences near the resonances of the TE_0 mode, one can see the pronounced deviations near the resonances of the TE_1 mode.

It should be emphasized that the invariance of the dropped power for interchanging the gaps can be used as an additional check of the consistency of the model. The almost perfect agreement of the the curves for the dropped power in Figures 4.19 and 4.20 shows that the present CMT based model of microresonators satisfies this constraint very well.

4.6 Tuning

From a practical point of view, the ability to tune the spectral response of the resonators is an essential feature. As mentioned in Section 1.4.5, a tuning mechanism can relax otherwise quite demanding fabrication tolerances, and it can also help to eliminate any unwanted temperature induced deviations of the spectral response.

For the applications of microresonators as tunable wavelength filters, suitable materials are introduced that permit to change slightly the refractive index of the cav-

ity core by external mechanisms like electro- or thermo-optic effects. Then using Eq. (1.21), shifts in resonance wavelengths due to changes of the core refractive index are given by

$$\Delta\lambda_m = \Delta n_c \frac{\partial\beta}{\partial n_c} \frac{\lambda_m}{\beta_m}, \quad (4.15)$$

where the derivative of the phase propagation constant with respect to the core refractive index can be approximated by Eq. (2.31) as

$$\frac{\partial\beta}{\partial n_c} = 2n_c \frac{\omega\epsilon_0}{R} \frac{\int_{R-d}^R \mathbf{E} \cdot \mathbf{E}^* r \, dr}{\int_0^\infty \mathbf{a}_\theta \cdot (\mathbf{E} \times \mathbf{H}^* + \mathbf{E}^* \times \mathbf{H}) \, dr}. \quad (4.16)$$

Here \mathbf{E} , \mathbf{H} are the electric field and magnetic field of the cavity mode associated with the m 'th order resonance.

Spectrum evaluation for perturbed resonators

By the interpolation method outlined in Section 4.3, in principle one can compute the resonator spectra for the unperturbed and the perturbed configurations separately. Instead of the scattering matrices S, \tilde{S} as given by Eq. (4.1), which are associated with the couplers defined over a larger z interval, one uses the scattering matrices S', \tilde{S}' as given by Eq. (4.10), which are associated with couplers of a zero length.

Similar to the arguments presented in Section 1.4.3, let's assume that for a slight change of the cavity core refractive index the scattering matrices S', \tilde{S}' do not change much, and the shifts of the resonances are entirely due to the changes in the cavity mode propagation constants. Then using S', \tilde{S}' of the unperturbed resonator, and adding the phase propagation constants shifts $\delta\beta_{bp}$ to the propagation constants γ_{bp} of the unperturbed cavity segments, one can again follow the interpolation method described in Section 4.3, without recalculating the scattering matrices for the perturbed resonator. In this way, a significant amount of computational work can be avoided.

Simulation results

Now we assess the validity of expressions (4.15), (4.16), and the above spectrum evaluation method for the perturbed resonators. For the assessment, we consider again the configurations of Sections 4.4.1 and 4.4.2. A cavity of radius $R = 5 \mu\text{m}$ is coupled to straight waveguides of width $w_s = 0.3 \mu\text{m}$ and core refractive index

$n_s = 1.5$. The background refractive index is $n_b = 1.0$, and the gap widths $g = \tilde{g} = 0.2 \mu\text{m}$. The cavity has the form of a ring, with a core width $w_c = 0.3 \mu\text{m}$, and of a disk, with $w_c = R$. For the unperturbed setting, the cavity core refractive index is $n_c = 1.5$. For the perturbed structure, this value is changed to $n_{cp} = 1.504$. The spectra are evaluated by quadratic interpolation with nodal wavelengths $\lambda = 1.015 \mu\text{m}, 1.05 \mu\text{m}, 1.085 \mu\text{m}$.

With the help of Eq. (4.16), the shifts in the (real part of) the cavity mode propagation constants at the resonance wavelengths of the unperturbed resonators are calculated; Eq.(4.15) then gives the shifts in the resonance wavelengths. Adding these differences to the unperturbed resonance wavelengths, determines the resonance positions for the perturbed configuration, which are compared with the resonance positions obtained by direct CMT simulations for the perturbed ($n_{cp} = 1.504$) resonator. Figure 4.21 depicts the spectral responses for the perturbed and the unperturbed ring resonators. The spectral response computed with the method outlined in this section agrees with the direct CMT calculation. Thus for a small perturbation of the cavity core refractive index, using the scattering matrices and the cavity propagation constants of the unperturbed structure, and the shifts in the cavity mode propagation constants, one can quite reliably predict the spectral response for the perturbed resonator.

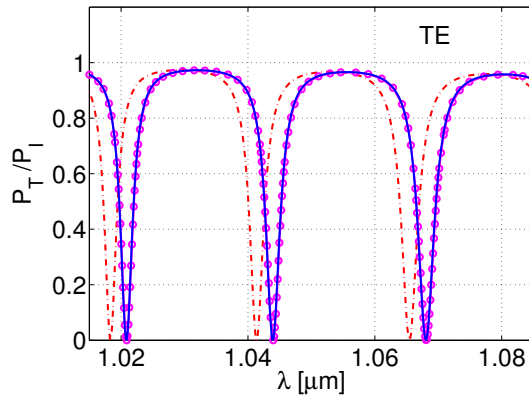


Figure 4.21: Spectrum shift due to tuning of the cavity core refractive index. The microring resonator configuration is as in Section 4.6. The curves of the normalized transmitted power are calculated by the spectrum evaluation method of Section 4.3 for the unperturbed resonator with $n_c = 1.5$ (dash-dotted line) and for the perturbed resonator with $n_{cp} = 1.504$ (circles), and by the approximation of Section 4.6 for the perturbed resonator (solid line).

A similar comparison of the transmitted power for the unperturbed and the perturbed disk resonator is shown in Figure 4.22. Just as in the case of the monomodal ring, for the present multimodal disk we find that the perturbed resonator spectrum computed by the approximation method (solid line) discussed in this section agrees well with the direct CMT simulations (circles), what concerns the resonance positions.

Minor deviations are observed in the depths of the resonance dips, in particular for the TE_1 resonances, where apparently the change in modal attenuation due to the core refractive index change is slightly larger than for the TE_0 mode. This alteration of the cavity mode losses is not taken into account by the present approximation procedure.

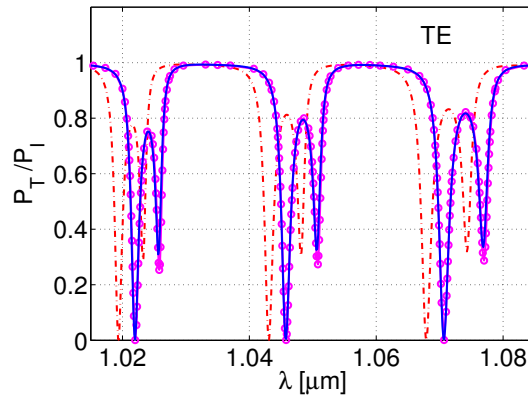


Figure 4.22: Spectral shift due to the cavity core refractive index perturbation, for the microdisk resonator as specified in Section 4.6. The interpretation of the curves is as for Figure 4.21.

4.7 Concluding remarks

A two dimensional frequency domain model of circular integrated optical microresonators based on spatial coupled mode theory has been investigated. Representing a direct implementation of the most common notions found in discussions of optical microring resonators, the present approach provides a thorough quantitative basis for the resonator design. It turns out that only a few most relevant basis fields are required to construct approximate solutions to the scattering problems that are sufficient for purposes of practical resonator design. The CMT results agree well with rigorous FDTD simulations; the computational effort for the CMT analysis

is significantly lower. Hence the approach qualifies for a generalization to three spatial dimensions [69], where hardly any alternative, practically applicable tools are available.

The numerical examples included single- and multimode microring and -disk structures, with relatively small cavity diameters and substantial refractive index contrasts, which represent rather worst-case configurations for the CMT analysis. Beyond the optical power transmission characteristics, the CMT procedures permit the direct examination of the local amplitudes of all included basis modes, and the inspection of all components of the local optical electromagnetic field. By means of adequately interpolated bend mode propagation constants and coupler scattering matrices, the spectral properties of the resonators can be evaluated in a highly efficient way. A systematic analysis of effect of the separation distances on the resonator spectral response shows that for the identical couplers setting, at resonance the drop power is maximum and the through power is minimum. It is also verified that the constrain of invariance of the drop power for interchanging the gaps is satisfied by the present CMT simulations. A perturbational analysis permits to compute reliably shifts in the resonances due to small changes of the core refractive index.

Chapter 5

Conclusions and outlook

Resonators based on circular microcavities are promising devices for applications as tunable add/drop wavelength filters in integrated optics. In this thesis, we have investigated a two dimensional frequency domain model of these devices based on spatial coupled mode theory. The approach followed in this work is directly interpretable in physical terms, and it is free of any fit parameters.

Conclusions

A functional decomposition of the resonators, outlined in Chapter 1, in terms of two bent-straight waveguide couplers with appropriate straight waveguide and bent waveguide connections, led to expressions for their spectral responses in terms of the constituent cavity mode propagation constants and the coupler scattering matrices. We presented a systematic approach to compute these parameters for given resonators.

To determine the cavity mode propagation constants, in Chapter 2 we turn to a classical analytic frequency domain model for 2-D optical bent slab waveguides and curved dielectric interfaces with piecewise constant refractive index profiles. A field ansatz in terms of complex order Bessel and Hankel functions led to an eigenvalue equation that is to be solved for the complex valued mode propagation constants. Unlike the fields in a complex frequency model of full cavities [39, 40], in the present case the asymptotic expansions of the relevant Hankel functions show that the modal solutions decay according to $1/\sqrt{r}$ for growing radial coordinates r . For the normalization of bend modes, we derived quite compact expressions for the angular modal power. We also discussed orthogonality properties of nondegener-

ate, directional, and polarized modal solutions of the bent waveguide problem. For the later discussion of tuning of resonators by changes of the core refractive index, a perturbational analysis for shifts in the propagation constants of bend modes is discussed.

Our implementation of “uniform asymptotic expansions” for Bessel functions of complex order facilitated the computational evaluation of the present analytic model of bent waveguides. In Chapter 2 we have presented a series of detailed (benchmark) examples of fundamental and higher order modes of bent slabs and whispering gallery modes. These include the computation of propagation constants (in view of the arbitrariness in the definition of the bend radius), bend mode profiles, and the spatial evolution of the related physical fields. A few illustrative examples for interferences of bend modes have been shown, that exhibit a periodic angular beating pattern (apart from the mode decay) in the guiding regions of the bends, and tangential, ray-like bundles of outgoing waves in the exterior regions. The validity of the perturbational expression for shifts in the propagation constants of moderately lossy modes has been verified.

To obtain the required coupler scattering matrices, in Chapter 3 we have proposed a spatial coupled mode theory based model of 2-D bent-straight waveguide couplers. In this pure frequency domain approach, the coupled mode equations are rigorously derived by a variational principle. Leveraged by the availability of the analytic bent modes on unbounded radial intervals, we could implement this model in consistent standard physical notions. By solving the coupled mode equations numerically, and projecting the resulting coupled mode field on the modes of the straight waveguide, we obtained the scattering matrices of the couplers. In symmetrical coupler settings, the scattering matrices satisfy a reciprocity property, that permits to assess the validity of the simulation results.

With the above coupled mode theory model, a detailed study of the effects of separation distance, the radius of the bent waveguide, and the wavelength on the scattering matrices has been carried out. For couplers involving bent waveguides that support multiple whispering gallery modes, with the present approach we have systematically investigate the significance of the individual modes. This feature of the present CMT formulation provides good insight for the characterization of resonances of the entire device.

With bent modes and coupler scattering matrices being available, in Chapter 4 we further elaborated the resonator model discussed in Chapter 1. We have formulated it for the multimodal setting. Also, approximations for fast-yet-reliable spectrum computation have discussed. The resonator model has been assessed for several examples of monomodal/multimodal structures with ring or disk cavities. In case

of a resonator with multimodal cavity, it turns out that only a few most relevant cavity basis fields are required to construct approximate solutions to the scattering problems that are sufficient for purposes of practical resonator design. With the present CMT approach, one can associate different resonance extrema in the spectral response with specific cavity modes. The comparison of CMT results with rigorous FDTD simulations shows good agreement. Moreover, the computational effort for the CMT analysis combined with the interpolation technique of Chapter 4 is substantially lower. The resonator field plots obtained with the CMT model provide useful qualitative impressions of the functioning of the resonators.

An analysis of effect of the separation distances on the spectral response shows that for the identical couplers setting, at resonance the drop power is maximum and the through power is minimum. The constrain of invariance of the drop power for interchanging the gaps is very well satisfied by the present CMT simulations. The perturbational analysis of shifts in the resonances due to slight changes in the cavity core refractive index agrees quite well with direct calculations.

Outlook

Now we would like to mention several interesting issues intimately related to the work carried out in this thesis, that deserve further attention. A few aspects are of more theoretical nature, while others are interesting from the application point of view.

The present analysis for the shifts of propagation constants due to changes in the cavity core refractive index (see Section 2.5) takes into account only the change in the real part of the propagation constants. Further investigation is necessary concerning more appropriate expressions, which give the changes in both the real and imaginary parts of the propagation constants.

Besides the present formulation, there exist other versions of coupled mode theory, e.g. spatial CMT with an ansatz for only the electric or the magnetic field, or time dependent CMT, that are applicable to the 2-D resonators as well. A comparative study of these different versions of CMT should be attempted.

For demonstrating the applicability and performance of the CMT method for the modeling of 2-D circular resonators, in the present work we restricted ourselves to unidirectional waves, and discussed configurations with adiabatic couplers and negligible backreflections only. For very small cavities the interaction between the straight waveguides and the cavity may not be adiabatic. To handle such cases, the present model should be extended to bidirectional waves.

Multiple coupled rings can improve the filter performance, when compared to a single resonator, by enhancing the resonance features in certain aspects [22]. The multiple cavities can be cascaded serially or in parallel. Modeling of such multicavity resonators requires the simulations of the coupling between two bent waveguides (or cavities). A CMT analysis for the interaction between two curved waveguides needs to be carried out.

Towards 3-D simulations

The approach followed in this thesis can be systematically extended to 3-D settings, where at present hardly any other practically applicable tools are available. Recently, significant progress has been made in this direction. For the reliable computation of bent modes and their propagation constants, a 3-D vectorial eigenmode solver for bent waveguides based on film mode matching has been proposed [67, 68]. Using these modes, a 3-D model of bent-straight waveguide couplers and microresonators has been implemented, as presented in Ref. [69]. These tools permit the reliable simulation and analysis of realistic devices, including specific 3-D features like vertical coupling or cavities that support hybrid modes.

Bibliography

- [1] W. A. Gambling. The rise and rise of optical fibers. *IEEE Journal of Selected Topics in Quantum Electronics*, 6(6):1084–1093, November-December 2000.
- [2] H. Sobol. Microwave communications-An historical perspective. *IEEE Transactions on Microwave Theory and Techniques*, 32(9):1170–1181, September 1984.
- [3] C. Yeh. *Applied photonics*. Academic press, Inc., California, 1994.
- [4] R. Ramaswami. Optical fiber communication: From transmission to networking. *IEEE Communications Magazine*, pages 138 – 147, May 2002.
- [5] N. Savage. Linking with light. *IEEE Spectrum*, 39(8):32–36, August 2002.
- [6] G. I. Papadimitriou, C. Papazoglou, and A. S. Pomportsis. Optical switching: switch fabrics, techniques, and architectures. *IEEE Journal of Light-wave Technology*, 21(2):384–405, February 2003.
- [7] P. S. Peercy. The drive to miniaturization. *Nature*, 406:1023–1026, August 2000.
- [8] M. Saruwatari. All-optical signal processing for terabit/second optical transmission. *IEEE Journal of Selected Topics in Quantum Electronics*, 6(6):1363–1374, November-December 2000.
- [9] K. J. Vahala. Optical microcavities. *Nature*, 424:839–846, August 2003.
- [10] E. A. J. Marcatili. Bends in optical dielectric guides. *The Bell System Technical Journal*, pages 2103–2132, September 1969.
- [11] B. Liu, A. Shakouri, and J. E. Bowers. Passive microring resonator coupled lasers. *Applied Physics Letters*, 79(22):3561–3563, November 2001.

BIBLIOGRAPHY

- [12] M. Kuwata-Gonokami, R. H. Jordan, A. Dodabalapur, H. E. Katz, M. L. Schilling, R. E. Slusher, and S. Ozawa. Polymer microdisk and microring lasers. *Optics Letters*, 20(20):2093–2095, October 1995.
- [13] S. J. Choi, K. Djordjev, S. J. Choi, and P.D. Dapkus. Microdisk lasers vertically coupled to output waveguides. *IEEE Photonics Technology Letters*, 15(10):1330–1332, October 2003.
- [14] T. A. Ibrahim, R. Grover, L. C. Kuo, S. Kanakaraju, L. C. Calhoun, and P. T. Ho. All-optical AND/NAND logic gates using semiconductor microresonators. *IEEE Photonics Technology Letters*, 15(10):1422–1424, October 2003.
- [15] T. A. Ibrahim, K. Amarnath, L. C. Kuo, R. Grover, V. Van, and P. T. Ho. Photonic logic NOR gate based on two symmetric microring resonators. *Optics Letters*, 29(23):2779–2781, December 2004.
- [16] V. R. Almeida, C. A. Barrios, R. R. Panepucci, and M. Lipson. All-optical control of light on a silicon chip. *Nature*, 431:1081–1084, October 2004.
- [17] F. C. Blom, D. R. van Dijk, H. J. W. M. Hoekstra, A. Driessen, and T. J. A. Popma. Experimental study of integrated optics microcavity resonators: Towards and all optical switching device. *Applied Physics Letters*, 71(6):747–749, August 1997.
- [18] K. Djordjev, S. J. Choi, S. J. Choi, and R.D Dapkus. Microdisk tunable resonant filters and switches. *IEEE Photonics Technology Letters*, 14(6):828–830, June 2002.
- [19] R. W. Boyd and J. E. Heebner. Sensitive disk resonator photonic biosensor. *Applied Optics*, 40(31):5742–5747, November 2001.
- [20] S. Blair and Y. Chen. Resonant-enhanced evanescent-wave fluorescence biosensing with cylindrical optical cavities. *Applied Optics*, 40(4):570–582, February 2001.
- [21] M. Rosenblit, P. Horak, S. Helsby, and R. Folman. Single-atom detection using whispering-gallery modes of microdisk resonators. *Physical Review A*, 70(053808), 2004.
- [22] B. E. Little, S. T. Chu, H. A. Haus, J. Foresi, and J. P. Laine. Microring resonator channel dropping filters. *IEEE Journal of Lightwave Technology*, 15(6):998–1005, June 1997.

-
- [23] F. C. Blom, H. Kelderman, H. W. J. M. Hoekstra, A. Driessen, T. J. A. Popma, S. T. Chu, and B. E. Little. A single channel dropping filter based on a cylindrical microresonator. *Optics Communications*, 167:77–82, August 1999.
- [24] K. Okamoto. Recent progress of integrated optics planar lightwave circuits. *Optical and Quantum Electronics*, 31(2):107–129, February 1999.
- [25] Y. Hibino. An array of photonic filtering advantages: arrayed-waveguide-grating multi/demultiplexers for photonic networks. *IEEE Circuits and Devices Magazine*, 16(6):21–27, November 2000.
- [26] H. Uetsuka. AWG technologies for dense WDM applications. *IEEE Journal of Selected Topics in Quantum Electronics*, 10(2):393–402, March-April 2004.
- [27] Y. Barbarin, X. J. M. Leijtens, E. A. J. M. Bente, C. M. Louzao, J. R. Kooiman, and M. K. Smit. Extremely small AWG demultiplexer fabricated on InP by using a double-etch process. *IEEE Photonics Technology Letters*, 16(11):2478–2480, November 2004.
- [28] S. Fan, P. R. Villeneuve, J. D. Joannopoulos, and H. A. Haus. Channel drop filters in photonic crystals. *Optics Express*, 3(1):4–11, July 1998.
- [29] M. Koshiba. Wavelength division multiplexing and demultiplexing with photonic crystal waveguide couplers. *IEEE Journal of Lightwave Technology*, 19(12):1970–1975, December 2001.
- [30] R. Costa, A. Melloni, and M. Martinelli. Bandpass resonant filters in photonic-crystal waveguides. *IEEE Photonics Technology Letters*, 15(3):401–403, March 2003.
- [31] M. Bertolotti, A. Driessen, and F. Michelotti, editors. *Microresonators as building blocks for VLSI photonics*, volume 709 of AIP conference proceedings. American Institute of Physics, Melville, New York, 2004.
- [32] Next generation Active Integrated optic Subsystems, project duration: September, 2001 to September, 2004. Information society technologies programme of the European Commission, project IST-2000-28018, <http://www.mesaplus.utwente.nl/nais/>.
- [33] D. J. W. Klunder, E. Krioukov, F. S. Tan, T van der Veen, H. F. Bulthuis, G. Sengo, C. Otto, H. W. J. M. Hoekstra, and A. Driessen. Vertically and

BIBLIOGRAPHY

- laterally waveguide-coupled cylindrical microresonators in Si_3N_4 on SiO_2 technology. *Applied Physics B*, 73:603–608, 2001.
- [34] M. Hammer, K. R. Hiremath, and R. Stoffer. Analytical approaches to the description of optical microresonator devices. In M. Bertolotti, A. Driessen, and F. Michelotti, editors, *Microresonators as building blocks for VLSI photonics*, volume 709 of AIP conference proceedings, pages 48–71. American Institute of Physics, Melville, New York, 2004.
- [35] K. Okamoto. *Fundamentals of Optical Waveguides*. Academic Press, U.S.A, 2000.
- [36] M. Lohmeyer, N. Bahlmann, O. Zhuromskyy, and P. Hertel. Perturbational estimation of geometry tolerances for rectangular integrated optics devices. In *Proceedings of SPIE, Integrated Optics Devices III*, volume 3620, pages 311–319, 1999.
- [37] D. K. Cheng. *Fields and Wave Electromagnetics (2'nd Ed.)*. Addison-Wesley, U.S.A., 1989.
- [38] D. J. W. Klunder, F. S. Tan, T. van der Veen, H. F. Bulthuis, G. Sengo, B. Docter, H. J. W. M. Hoekstra, and A. Driessen. Experimental and numerical study of SiON microresonators with air and polymer cladding. *IEEE Journal of Lightwave Technology*, 21(4):1099–1110, April 2003.
- [39] L. Prkna, J. Čtyroký, and M. Hubálek. Ring microresonator as a photonic structure with complex eigenfrequency. *Optical and Quantum Electronics*, 36(1–3):259–269, January-February 2004.
- [40] J. Čtyroký, L. Prkna, and M. Hubálek. Guided-wave optical microresonators: Calculation of eigenmodes. In M. Bertolotti, A. Driessen, and F. Michelotti, editors, *Microresonators as building blocks for VLSI photonics*, volume 709 of AIP conference proceedings, pages 72–90. American Institute of Physics, Melville, New York, 2004.
- [41] A. Morand, K. Phan-Huy, Y. Desieres, and P. Benech. Analytical study of the microdisk's resonant modes coupling with a waveguide based on the perturbation theory. *IEEE Journal of Lightwave Technology*, 22(3):827–832, March 2004.
- [42] T Tamir (Ed.). *Integrated Optics (Second Corrected and Updated Edition)*. Springer-Verlag, Germany, 1982.

- [43] C. Vassallo. *Optical Waveguide Concepts*. Elsevier, Amsterdam, 1991.
- [44] D. R. Rowland and J. D. Love. Evanescent wave coupling of whispering gallery modes of a dielectric cylinder. *IEE Proceedings, Pt. J*, 140(3):177–188, June 1993.
- [45] L. F. Stokes, M. Chodorow, and H. J. Shaw. All single mode fiber resonator. *Optics Letters*, 7(6):288–290, June 1982.
- [46] K. Oda, N. Takato, and H. Toba. A wide-FSR waveguide double-ring resonator for optical FDM transmission systems. *IEEE Journal of Lightwave Technology*, 9(6):728–736, June 1991.
- [47] P. Urquhart. Compound optical-fiber-based resonators. *Journal of the Optical Society of America A*, 5(6):803–812, June 1988.
- [48] A. Yariv. Universal relations for coupling of optical power between microresonators and dielectric waveguides. *Electronics Letters*, 36(4), February 2000.
- [49] I. D. Chremmos and Uzunoglu N. K. Analysis of coupling between two slab waveguides in the presence of ring resonators. *Journal of the Optical Society of America A*, 21(2):267–279, February 2004.
- [50] D. G. Hall and B. J. Thompson, editors. *Selected Papers on Coupled-Mode Theory in Guided-Wave Optics*, volume MS 84 of *SPIE Milestone Series*. SPIE Optical Engineering Press, Bellingham, Washington USA, 1993.
- [51] H. A. Haus. *Waves and Fields in Optoelectronics*. Prentice Hall, 1984.
- [52] S. L. Chuang. A coupled mode formulation by reciprocity and a variational principle. *Journal of Lightwave Technology*, 5(1):5–15, January 1987.
- [53] C. Manolatou, M. J. Khan, S. Fan, P. R. Villeneuve, H. A. Haus, and J. D. Joannopoulos. Coupling of modes analysis of resonant channel add drop filters. *IEEE Journal of Quantum Electronics*, 35(9):1322–1331, September 1999.
- [54] M. K. Chin and S. T. Ho. Design and modeling of waveguide coupled single mode microring resonator. *IEEE Journal of Lightwave Technology*, 16(8):1433–1446, August 1998.
- [55] A. Taflove. *Computational Electrodynamics: The Finite Difference Time Domain Method*. Artech House Inc., Norwood, MA, USA, 1995.

BIBLIOGRAPHY

- [56] S. C. Hagness, D. Rafizadeh, S. T. Ho, and A. Taflove. FDTD microcavity simulations: Design and experimental realization of waveguide coupled single mode ring and whispering gallery mode disk resonator. *IEEE Journal of Lightwave Technology*, 15(11):2154–2165, November 1997.
- [57] R. Stoffer. *Uni- and Omnidirectional Simulation Tools for Integrated Optics*. PhD thesis, University of Twente, Enschede, The Netherlands, May 2001.
- [58] A. I. Nosich. The method of analytical regularization in wave-scattering and eigenvalue problems: Foundations and review of solutions. *IEEE Antennas and Propagation Magazine*, 41(3):34–49, June 1999.
- [59] S. V. Boriskina, T. M. Benson, P. Sewell, and A. I. Nosich. Effect of a layered environment on the complex natural frequencies of two-dimensional WGM dielectric-ring resonators. *IEEE Journal of Lightwave Technology*, 20(8):1563–1572, August 2002.
- [60] S. V. Boriskina, T. M. Benson, P. Sewell, and A. I. Nosich. Highly efficient design of spectrally engineered whispering-gallery-mode microlaser resonators. *Optical and Quantum Electronics*, 35(4/5):545–559, November–December 2003.
- [61] S. V. Boriskina and A. I. Nosich. Radiation and absorption losses of the whispering-gallery-mode dielectric resonators excited by a dielectric waveguide. *IEEE Transactions on Microwave Theory and Techniques*, 47(2):224–231, February 1999.
- [62] S. V. Boriskina, T. M. Benson, P. Sewell, and A. I. Nosich. Tuning of elliptic whispering-gallery-mode microdisk waveguide filters. *IEEE Journal of Lightwave Technology*, 21(9):1987–1995, September 2003.
- [63] D. Marcuse. Bending losses of the asymmetric slab waveguide. *The Bell System Technical Journal*, October:2551–2563, 1971.
- [64] L. Lewin, D. C. Chang, and E. F. Kuester. *Electromagnetic Waves and Curved Structures*. Peter Peregrinus Ltd. (On behalf of IEE), Stevenage, England, 1977.
- [65] E. C. M. Pennings. *Bends in Optical Ridge Waveguides, Modelling and Experiment*. PhD thesis, Delft University, The Netherlands, June 1990.
- [66] H. J. M. Bastiaansen, J. M. van der Keur, and H. Blok. Rigorously modeling short bent, graded-index dielectric slab waveguides. *IEEE Transactions on Microwave Theory and Techniques*, 41(11):1972–1980, November 1993.

-
- [67] L. Prkna, M. Hubálek, and J. Čtyroký. Vectorial eigenmode solver for bent waveguides based on mode matching. *IEEE Photonics Technology Letters*, 16(9):2057–2059, September 2004.
- [68] L. Prkna, M. Hubálek, and J. Čtyroký. Field modeling of circular microresonators by film mode matching. *IEEE Journal of Selected Topics in Quantum Electronics*, 11(1):217–223, January/February 2005.
- [69] R. Stoffer, K. R. Hiremath, M. Hammer, L. Prkna, and J. Čtyroký. Cylindrical integrated optical microresonators: Modeling by 3-D vectorial coupled mode theory. *Optics Communications*, 2005. (accepted).
- [70] D. G. Hall and B. J. Thompson, editors. *Selected Papers on Coupled-Mode Theory in Guided-Wave Optics*, volume MS 84 of *SPIE Milestone Series*. SPIE Optical Engineering Press, Bellingham, Washington USA, 1993.
- [71] R. Stoffer, K. R. Hiremath, and M. Hammer. Comparison of coupled mode theory and FDTD simulations of coupling between bent and straight optical waveguides. In M. Bertolotti, A. Driessen, and F. Michelotti, editors, *Microresonators as building blocks for VLSI photonics*, volume 709 of AIP conference proceedings, pages 366–377. American Institute of Physics, Melville, New York, 2004.
- [72] K. R. Hiremath, R. Stoffer, and M. Hammer. Multimode circular integrated optical microresonators: Coupled mode theory modeling. In *Proceedings of 9th Annual Symposium of IEEE/LEOS Benelux Chapter*, pages 79–82, 2004.
- [73] M. Abramowitz and I. A. Stegun. *Handbook of Mathematical Functions (Applied Mathematics Series 55)*. National Bureau of Standards, Washington, D.C., 1964.
- [74] N. M. Temme. Numerical algorithms for uniform Airy-type asymptotic expansions. Technical Report MAS-R9706, Centrum voor Wiskunde en Informatica, Amsterdam, The Netherlands, 1997.
- [75] L. Prkna. *Rotationally symmetric resonant devices in integrated optics*. PhD thesis, Faculty of Mathematics and Physics, Charles University, Prague, Czech Republic, July 2004.
- [76] C. Winkler, J. D. Love, and A. K. Ghatak. Loss calculations in bent multimode optical waveguides. *Optical and Quantum Electronics*, 11:173–183, 1979.

BIBLIOGRAPHY

- [77] A. Ghatak, E. Sharma, and J. Kompella. Exact ray paths in bent waveguides. *Applied Optics*, 27(15):3180–3184, August 1988.
- [78] M. Heiblum and J. H. Harris. Analysis of curved optical waveguide by conformal transformation. *IEEE Journal of Quantum Electronics*, 11(2):75–83, February 1975.
- [79] F. Wassmann. Modal field analysis of circularly bent single-mode fibers. *IEEE Journal of Lightwave Technology*, 17(5):957–968, May 1999.
- [80] P. Bienstman, E. Six, A. Roelens, M. Vanwolleghem, and R. Baets. Calculation of bending losses in dielectric waveguides using eigenmode expansion and perfectly matched layers. *IEEE Photonics Technology Letters*, 14(2):164–166, February 2002.
- [81] A. Melloni, F. Carniel, R. Costa, and M. Martinelli. Determination of bend mode characteristics in dielectric waveguides. *IEEE Journal of Lightwave Technology*, 19(4):571–577, April 2001.
- [82] W. Berglund and A. Gopinath. WKB analysis of bend losses in optical waveguides. *IEEE Journal of Lightwave Technology*, 18(8):1161–1166, August 2000.
- [83] J. M. van der Keur. Propagation properties of a circularly curved, transversely inhomogeneous, dielectric slab waveguide. Technical Report Et/EM 1992-02, Electromagnetic Research Laboratory, Faculty of Electrical Engineering, University of Delft, The Netherlands, 1992.
- [84] M. Rivera. A Finite Difference BPM analysis of bent dielectric waveguides. *IEEE Journal of Lightwave Technology*, 13(2):233–238, February 1995.
- [85] R. Pregla. The Method of Lines for the analysis of dielectric waveguide bends. *IEEE Journal of Lightwave Technology*, 14(4):634–639, April 1996.
- [86] S. Kim and A. Gopinath. Vector analysis of optical dielectric waveguide bends using finite-difference method. *IEEE Journal of Lightwave Technology*, 14(9):2085–2092, September 1996.
- [87] T. Yamamoto and M. Koshiba. Analysis of curvature losses of whispering gallery modes in an optical dielectric disk by the finite-element method. *IEEE Journal of Lightwave Technology*, 12(1):59–63, January 1994.
- [88] H. J. M. Bastiaansen. *Modal Analysis of Straight and Curved Integrated Optical Waveguides, An integral equation approach*. PhD thesis, Delft University, The Netherlands, 1994.

- [89] Y. L. Luke. *Integrals of Bessel functions*. McGraw-Hill, New York, 1962.
- [90] P. Benech, D. A. M. Khalil, and F. S. Andr . An exact simplified method for the normalization of radiation modes in planar multilayer structures. *Optics Communications*, 88:96–100, March 1992.
- [91] N. Morita and R. Yamada. Electromagnetic fields in circular bends of slab waveguides. *IEEE Journal of Lightwave Technology*, 8(1):16–22, January 1990.
- [92] D. E. Amos. A portable package for Bessel functions of a complex argument and nonnegative order, 1983. <http://www.netlib.org/amos/> .
- [93] D. Marcuse. *Light Transmission Optics*. Van Nostrand Reinhold Company, New York, USA, 1972.
- [94] K. S. Yee. Numerical solution of boundary value problems involving Maxwell’s equations in isotropic media. *IEEE Transactions on Antennas and Propagation*, 14(3):302–307, May 1966.
- [95] R. Stoffer, H. J. W. M. Hoekstra, R. M. de Ridder, E. van Groesen, and F. P. H. van Beckum. Numerical studies of 2D photonic crystals: Waveguides, coupling between waveguides and filters. *Optical and Quantum Electronics*, 32:947–961, 2000.
- [96] D. J. W. Klunder, M. L. M. Balisteri, F. C. Blom, J. W. M. Hoekstra, A. Driessen, L. Kuipers, and N. F. Van Hulst. High-resolution photon-scanning tunneling microscope measurements of the whispering gallery modes in a cylindrical microresonator. *IEEE Photonics Technology Letters*, 12(11):1531–1533, November 2000.
- [97] M. L. M. Balistreri, D. J. W. Klunder, F. C. Blom, A. Driessen, J. P. Korterik, L. Kuipers, and N. F. van Hulst. Experimental analysis of the whispering gallery modes in a cylindrical optical microcavity. *Journal of the Optical Society of America B*, 18(4):465–471, April 2001.
- [98] D. J. W. Klunder, M. L. M. Balistreri, F. C. Blom, H. W. J. M. Hoekstra, A. Driessen, L. Kuipers, and N. F. van Hulst. Detailed analysis of the intracavity phenomena inside a cylindrical microresonator. *IEEE Journal of Lightwave Technology*, 20(3):519–529, March 2002.
- [99] G. Sztefka and H. P. Nolting. Bidirectional eigenmode propagation for large refractive index steps. *IEEE Journal of Lightwave Technology*, 5(5):554–557, May 1993.

BIBLIOGRAPHY

- [100] M. Hammer. Quadridirectional eigenmode expansion scheme for 2-D modeling of wave propagation in integrated optics. *Optics Communications*, 235(4-6):285–303, May 2004.
- [101] N. H. G. Baken. *Computational modeling of integrated optical waveguides*. PhD thesis, Delft University, The Netherlands, October 1990.
- [102] H. J. M. Bastiaansen, J. M. van der Keur, and H. Blok. Rigorous, full-vectorial source-type integral equation analysis of circularly curved channel waveguides. *IEEE Transactions on Microwave Theory and Techniques*, 43(2):401–409, February 1995.
- [103] E. W. Kolk, N. H. G. Baken, and H. Blok. Domain integral equation analysis of integrated optical channel and ridge waveguides in stratified media. *IEEE Transactions on Microwave Theory and Techniques*, 38(1):78–85, January 1990.
- [104] H. J. W. M. Hoekstra. On beam propagation methods for modelling in integrated optics. *Optical and Quantum Electronics*, 29(2):157–171, January 1997.
- [105] S. T. Chu and S. K. Chaudhuri. A finite-difference time-domain method for the design and analysis of guided-wave optical structures. *IEEE Journal of Lightwave Technology*, 7(12):2033–2038, December 1989.
- [106] H. P. Uranus. *Guiding light by and beyond the total internal reflection mechanism*. PhD thesis, University of Twente, Enschede, The Netherlands, April 2004.
- [107] A. Hardy and W. Streifer. Coupled mode theory of parallel waveguides. *IEEE Journal of Lightwave Technology*, 3(5):1135–1146, October 1985.
- [108] A. W. Snyder. Coupled-mode theory for optical fibers. *Journal of the Optical Society of America*, 62(11):1267–1277, November 1972.
- [109] M. L. Gorodetsky and V. S. Ilchenko. Optical microsphere resonators: Optimal coupling to high Q whispering gallery modes. *JOSA:B*, 16(1):147–154, January 1999.
- [110] S. J. Choi, K. Djordjev, S. J. Choi, P. D. Dapkus, W. Lin, G. Griffel, R. Menna, and J. Connolly. Microring resonators vertically coupled to buried heterostructure bus waveguides. *IEEE Journal of Lightwave Technology*, 16(3):828–830, March 2004.

BIBLIOGRAPHY

- [111] E. van Groesen. Applied analytical methods: Part I Basic variational structures and methods. Lecture notes, Applied Analysis and Mathematical Physics, Department of Applied Mathematics, University of Twente, Enschede, The Netherlands, March 2001.
- [112] M. Becker. *The principles and applications of variational methods*. Research Monograph No. 27. The M.I.T. Press, Cambridge, Massachusetts, U.S.A., 1964.
- [113] W. H. Press, S. A. Teukolsky, W. T. Vetterling, and B. P. Flannery. *Numerical Recipes in C, 2nd ed.* Cambridge University Press, 1992.
- [114] K. R. Hiremath, M. Hammer, S. Stoffer, L. Prkna, and J. Čtyroký. Analytic approach to dielectric optical bent slab waveguides. *Optical and Quantum Electronics*, 37(1-3):37–61, January 2005.
- [115] M. Hammer. Resonant coupling of dielectric optical waveguides via rectangular microcavities: The coupled guided mode perspective. *Optics Communications*, 214(1–6):155–170, 2002.

Curriculum Vitae

Kirankumar R. Hiremath was born on 21 August 1976 at Solapur, Maharashtra, India. He did his Bachelor of Science in Physics (Honors) from Sangmeshwar College, Solapur, and graduated with distinction in 1997. After that, he got an admission in Indian Institute of Technology Bombay (IIT-B) for post graduation in mathematics.

After post graduation in pure mathematics, he worked at IIT-B. First at Microwave Remote Sensing Lab of Center for Studies in Resource Engineering (from May 1999 to February 2000), for Indian Space Research Organization - IIT-B sponsored project of “SAR Interferometry and Earth Crust Movement” under the guidance of Dr. K. S. Rao. Then he worked at Industrial Mathematics Group of Department of Mathematics, for Department of Science and Technology sponsored project of “Doing Industrial Mathematics via Genetic Algorithms, Differential Algebraic Equations, Online Optimization, Computer Aided Geometric Design and Market Forecasting” (from March 2000 to August 2001) with Prof. A. K. Pani.

In September 2001, he joined University of Twente, The Netherlands, for Ph. D.. There he studied at Applied Analysis and Mathematical Physics group of Department of Applied Mathematics, and was affiliated with MESA+ Research Institute. With prof. dr. E. van Groesen as the promotor, and dr. Manfred Hammer as the supervisor, he did his research on the European Commission funded project “*Next generation Active Integrated optic Subsystems*” (NAIS). In August 2003, he finished his post graduation in mathematical sciences, and in October 2005, he finished his doctoral studies.